

THE MEASUREMENTS OF THE OPTICAL PROPERTIES OF DIAMOND-  
LIKE CARBON THIN FILMS BY FOURIER-TRANSFORM INFRARED  
SPECTROSCOPY

by

YIDAN XIE

B.Sc., Peking University, P.R.China, 1991

A THESIS SUBMITTED IN PARTIAL FULFILLMENT OF  
THE REQUIREMENTS FOR THE DEGREE OF  
MASTER OF SCIENCE

in

THE FACULTY OF GRADUATE STUDIES  
DEPARTMENT OF PHYSICS

We accept this thesis as conforming  
to the required standard

THE UNIVERSITY OF BRITISH COLUMBIA

October 1994

© Yidan Xie, 1994

In presenting this thesis in partial fulfilment of the requirements for an advanced degree at the University of British Columbia, I agree that the Library shall make it freely available for reference and study. I further agree that permission for extensive copying of this thesis for scholarly purposes may be granted by the head of my department or by his or her representatives. It is understood that copying or publication of this thesis for financial gain shall not be allowed without my written permission.

(Signature)

Department of Physics

The University of British Columbia  
Vancouver, Canada

Date Oct. 12, 1994

## **Abstract**

Infrared reflectance and transmittance measurements of diamond-like carbon thin films grown by d.c. magnetron sputtering were performed at nearly normal incidence, using a Bruker IFS 113V Fourier-transform spectrometer. The project was a collaboration with Glenn Clarke, a Ph.D student under the supervision of Dr. R. Parsons. Glenn Clarke grew all of the films and extracted the absorption coefficient from the reflectivity and transmission data, using a matrix method. The spectral features were mainly the broad interference oscillations characteristic of thin films and the absorptions caused by excited vibrational modes. An interband-transition model of  $n$  and  $k$ , together with a dispersion model, which is a superposition of the background absorption and the vibrational resonances, was used to fit the experimental data and obtain some information about the chemical bonds in these films. It was found that the optical properties of the diamond-like carbon films were strongly dependent on the deposition pressure during the sputtering and any hydrogen incorporation.

## **Table of Contents**

|   |            |
|---|------------|
| <b>Abstract</b>   | <b>ii</b>  |
| <b>Table of Contents</b>  | <b>iii</b> |
| <b>List of Tables</b>   | <b>vi</b>  |
| <b>List of Figures</b>  | <b>vii</b> |
| <b>Acknowledgment</b>   | <b>ix</b>  |
| <b>Chapter 1 Introduction</b>   | <b>1</b>   |
| 1.1 Diamond-like Carbon Thin Films  | 1          |
| 1.1.1 Attractive Properties and Applications  | 1          |
| 1.1.2 Deposition Technology   | 3          |
| 1.1.3 Experimental Work on the Properties of DLC Films                                | 6          |
| 1.1.3.1 Mechanical Properties   | 6          |
| 1.1.3.2 Electrical Properties   | 7          |
| 1.1.3.3 Optical Properties  | 8          |
| 1.2 Characterization Method for Optical Properties and Structures                     | 12         |
| 1.2.1 Ellipsometry  | 12         |
| 1.2.2 IR Spectroscopy   | 12         |
| 1.2.3 Raman Spectroscopy  | 13         |
| 1.2.4 X-ray Photoelectron Spectroscopy (XPS) and Auger<br>Electron Spectroscopy (AES) | 13         |
| 1.3 Purpose and Outline of the Thesis   | 14         |
| <b>Chapter 2 Experimental Method and Instrumentation</b>                              | <b>16</b>  |
| 2.1 Fourier-transform Spectroscopy  | 16         |
| 2.1.1 Michelson Interferometer  | 17         |

|   |           |
|---|-----------|
| 2.1.2 Fourier Analysis                                    | 20        |
| 2.1.2.1 Fourier Transformation                            | 20        |
| 2.1.2.2 Sampling Interval and Alising                     | 23        |
| 2.1.2.3 Picket-fence Effect and Zero Filling              | 27        |
| 2.1.2.4 Leakage and Apodization                           | 28        |
| 2.1.3 Resolution  | 30        |
| 2.1.4 Phase Correction                                    | 34        |
| 2.1.5 Comparison Between Grating and FT-IR spectrometer-- |           |
| Jacquinot and Fellgett Advantage                          | 35        |
| 2.1.5.1 Jacquinot Advantage                               | 35        |
| 2.1.5.2 Fellgett Advantage                                | 36        |
| 2.2 Instrumentation                                       | 37        |
| 2.2.1 Bruker IFS 113V FT-IR spectrometer                  | 37        |
| 2.2.2 Sources   | 42        |
| 2.2.3 Beamsplitters                                       | 42        |
| 2.2.4 Detectors   | 43        |
| <b>Chapter 3 Measurements</b>                             | <b>45</b> |
| 3.1 Reflectance Measurements                              | 45        |
| 3.1.1 Sample Chamber Arrangement                          | 45        |
| 3.1.2 Measurement Procedure                               | 45        |
| 3.2 Transmittance Measurements                            | 49        |
| 3.2.1 Sample Chamber Arrangement                          | 49        |
| 3.2.2 Measurement Procedure                               | 49        |
| 3.3 Sample Preparation                                    | 52        |

|  |           |
|--|-----------|
| <b>Chapter 4 Reflection, Transmission and Absorption in Amorphous Thin Films</b> | <b>54</b> |
| 4.1 Matrix Method for Reflectance and Transmittance Calculation                  | 54        |
| 4.1.1 The Sample Boundary  | 54        |
| 4.1.2 Assembly of Thin Films   | 55        |
| 4.1.3 Coherent Films and Incoherent Substrate                                    | 59        |
| 4.2 Optical Model for Amorphous Solids in the Interband Region                   | 61        |
| 4.2.1 Derivation of $k(E)$   | 61        |
| 4.2.2 Derivation of $n(E)$   | 63        |
| 4.3 Optical Model for Amorphous Solids in Long Wavelength Region                 | 64        |
| <b>Chapter 5 Experiment Results and Discussion</b>                               | <b>67</b> |
| 5.1 Experiment Results   | 67        |
| 5.1.1 Far-infrared Results   | 67        |
| 5.1.2 Mid-infrared Results   | 68        |
| 5.1.3 Near-infrared Results  | 69        |
| 5.1.4 Absorption Coefficients and Bonding Configuration                          | 69        |
| 5.2 Discussion   | 71        |
| 5.2.1 Optical Properties and Bonding Configuration                               | 71        |
| 5.2.2 Effects of Hydrogen and Oxygen Incorporation                               | 72        |
| 5.2.3 Effects of Deposition Pressure   | 73        |
| <b>Chapter 6 Conclusion</b>  | <b>93</b> |
| <b>Bibliography</b>  | <b>96</b> |

## **List of Tables**

|            |   |           |
|------------|---|-----------|
| <b>2-1</b> | <b>Coefficients for Blackmann-Harris function</b>   | <b>30</b> |
| <b>3-1</b> | <b>Optical Parameters in the Bruker IFS 113V</b>    | <b>47</b> |
| <b>3-2</b> | <b>Deposition Parameters for the Samples Tested</b> | <b>53</b> |
| <b>5-1</b> | <b>Fitting Parameters and Possible Bonding</b>      | <b>92</b> |

## **List of Figures**

|     |   |    |
|-----|---|----|
| 1-1 | Schematic of a planar magnetron sputtering system   | 5  |
| 2-1 | Schematic of a basic Michelson interferometer   | 19 |
| 2-2 | Examples of spectra and their corresponding interferograms  | 22 |
| 2-3 | Continuous interferogram and its computed spectrum  | 25 |
| 2-4 | Sampled interferogram and its computed spectrum   | 25 |
| 2-5 | Apodization functions and their corresponding Instrumental<br>Lineshapes                                    | 31 |
| 2-6 | Optical system of the Bruker IFS 113V   | 39 |
| 3-1 | Front channel optical arrangement in the Bruker IFS 113V  | 46 |
| 3-2 | Sample holder for reflectance measurements  | 46 |
| 3-3 | Back channel optical arrangement in the Bruker IFS 113V   | 50 |
| 3-4 | Sample holder for transmittance measurements  | 50 |
| 4-1 | Schematic of a pile of layers and coordinates   | 56 |
| 4-2 | The transformations of the waves across the interface between<br>layers and through the inside of the layer | 56 |
| 4-3 | Schematic of layers in our samples  | 60 |
| 5-1 | Far-infrared reflectance spectra of Si-GaAs and sample acap18   | 77 |
| 5-2 | Far-infrared transmittance spectra of Si-GaAs and sample acap18   | 78 |
| 5-3 | Mid-infrared reflectance and transmittance spectra of Si-GaAs   | 79 |
| 5-4 | Mid-infrared spectra of sample acju11   | 80 |
| 5-5 | Mid-infrared spectra of sample acju13   | 81 |
| 5-6 | Mid-infrared spectra of sample acau07   | 82 |
| 5-7 | Mid-infrared spectra of sample acju17   | 83 |



|      |   |    |
|------|---|----|
| 5-8  | Mid-infrared spectra of sample acjl27   | 84 |
| 5-9  | Near-infrared reflectance spectra of acau07 and acju17, and their best fittings                                     | 85 |
| 5-10 | Mid-infrared absorption coefficient spectrum of acju11 and its best fitting   | 86 |
| 5-11 | Mid-infrared absorption coefficient spectrum of acju13 and its best fitting   | 87 |
| 5-12 | Mid-infrared absorption coefficient spectrum of acju17 and its best fitting   | 88 |
| 5-13 | Mid-infrared absorption coefficient spectrum of acjl27 and its best fitting   | 89 |
| 5-14 | Mid-infrared absorption coefficient spectrum of acau07 and its best fitting   | 90 |
| 5-15 | Near-infrared $k$ for films of different deposition pressure and for films with and without impurity incorporations | 91 |

## **Acknowledgment**

I would like to thank my supervisor, Dr. J. E. Eldridge, for his patient, knowledgeable and valuable instructions and supervision.

All the samples were provided by Dr. Parson's lab. I am very grateful to Glenn Clarke for growing the samples and the work of obtaining film thicknesses and optical constants. I also would like to thank him for his helpful suggestions and discussions.

This work was supported by grants # 5-85653 and # 5-81631 from the Natural Science and Engineering Research Council of Canada (NSERC).

## **Chapter 1**

### **INTRODUCTION**

#### **1.1 Diamond-like Carbon Thin Films**

##### **1.1.1 Attractive Properties and Applications**

Carbon has two elementary forms: crystalline and amorphous. In its crystalline form, it can exist as either diamond, a wide band semiconductor, or graphite, a semimetal. The diamond crystal structure is face-centered cubic, in which each atom is covalently bonded to four other carbon atoms. These bonds are known as  $sp^3$  tetragonal bonds. The structure of graphite is described as layers of carbon atoms with strong  $sp^2$  trigonal bonds in the plane, and the fourth atom in the outer shell forms a weak van der Waals type bond between planes [1]. As a result, diamond has the properties of extreme hardness, chemical inertness, high electrical resistivity, high dielectric strength, excellent optical transparency in the infrared, and high thermal conductivity, while graphite appears to be the opposite: softness, lubricity, good electrical conductivity, lower density and a grayish-black appearance. On the other hand, in its amorphous forms, carbon can be regarded as degenerated or imperfect graphite structure, where only short-range order exists and is responsible for the intermediate properties.

Though diamond exhibits excellent mechanical and optical properties which make it an ideal window material, it is not readily available. This led to the development of Diamond-like carbon (DLC) films. They were first produced by Aisenberg and Chabot [2] and are characterized by extreme hardness and scratch

resistance, high electrical resistance, high dielectric strength, chemical inertness, and transparency in the infrared region. The properties of DLC films are closer to those of diamond than graphite. This may be explained by their structure and bonding network: the films are amorphous rather than crystalline, with all possible combinations of  $sp^1$ ,  $sp^2$ , and  $sp^3$  bonds, which are typical for carbyne, graphite, and diamond, respectively [3]. It has been found that a significant fraction of the carbon atoms is present as  $sp^3$  tetrahedrally coordinated sites in diamond-like carbon films [4] [5].

Arising from the extraordinary properties similar to diamond, the DLC films have drawn great attention and have been applied extensively, such as for wear- and corrosion-resistant coatings in sliding devices, antireflection coatings, protective coatings, dielectric p-n junctions, barrier coatings, passivation layers, and heat sinks in electrical devices [1]. The followings are some examples of these applications:

- Overcoats on thin-film media for magnetic recording

Since head-disk contact occurs intermittently when the drive starts and stops, the overcoats on the thin-film media used in computer hard disks are essential for reliable memory storage. The overcoats should be as thin as possible, resist wear by the head, have low static and dynamic friction coefficients with the head, and protect the medium against corrosion. Thus, the hard DLC film are widely used as wear resistant overcoats on thin film media [1].

- Antireflection coatings on germanium

The DLC film is smooth, hard, durable and optically transparent in the infrared, thus it is a suitable coating for germanium, which is the most commonly used window and lens material in this region but which is easily scratched by

sand and chemically attacked by salt water. Furthermore, the refractive index of 4 of germanium makes it reflect the incident light considerably. DLC films were shown to be very good as antireflection coatings on germanium [6].

- **Protective coatings on front surface aluminum mirror**

The optical performance of front surface mirrors in thermal imaging systems tends to deteriorate with time and with exposure to the atmosphere. DLC films have been demonstrated to be suitable protective coatings needed for the front surface mirrors in the infrared region, since they overcome the shortcomings of other types of coatings in this optical region [6].

### **1.1.2 Deposition Technology**

Diamond-like carbon films can be generally divided into two categories: hydrogenated and non-hydrogenated. Hydrogenated DLC films are typically prepared by impact of hydrocarbon ions in the energy region from several tens to 100eV. Direct deposition from hydrocarbon ion beams and by r.f. self-bias plasma assisted chemical vapor deposition are the most commonly used methods, which provide much higher impact energy than other methods. Non-hydrogenated DLC films containing little hydrogen can be prepared by sputtering of carbon, by direct ion beam deposition from ion beams or by condensation of vaporized carbon atoms produced by laser evaporation. It is impractical to describe all of these systems, and so some typical ones have been chosen.

- **Ion beam plating method**

Ion beam plating of hydrocarbons at an acceleration voltage has been used to prepare hydrogenated DLC films. Electrons, emitted from a hot tungsten cathode and accelerated passing through an anode grid up to 200eV, ionize

the vapor or gas molecules which are introduced into the deposition chamber and create a plasma [7]. Ions generated are accelerated to the substrate which is negatively biased. The ionization device is surrounded by a screen held at a floating potential. The hydrocarbon vapor used for film deposition are usually methane, ethane, butane, propane and benzene etc. [8].

- r.f. plasma deposition

r.f. plasma assisted chemical vapor deposition has the advantage of the ability to grow smooth transparent hydrogenated DLC films with a high deposition rate on a large area. One of these deposition systems was described by A.Bubenzer [9] to grow hydrogenated hard carbon thin films in an r.f. glow discharge sustained by a hydrocarbon gas. The system is first evacuated, then Ar discharge is started in order to sputter clean the substrate. A hydrocarbon gas is subsequently leaked into the system. In the r.f. discharge, hydrocarbons are partially ionized and cracked. Within the ion sheath region, the positively charged particles are accelerated toward the substrate and thereby form the carbon film. Benzene is usually chosen because of the comparatively low coating stress and high deposition rate that it can give.

- Magnetron sputtering

This method is widely used to generate non-hydrogenated carbon films. Though the deposition rate is low, it can produce smooth, transparent DLC films under extremely good operational control with respect to uniformity and homogeneity. Moreover, it can be used to grow multilayer films and has the ability to scale to the larger sources and substrate areas necessary for industrial application [10].

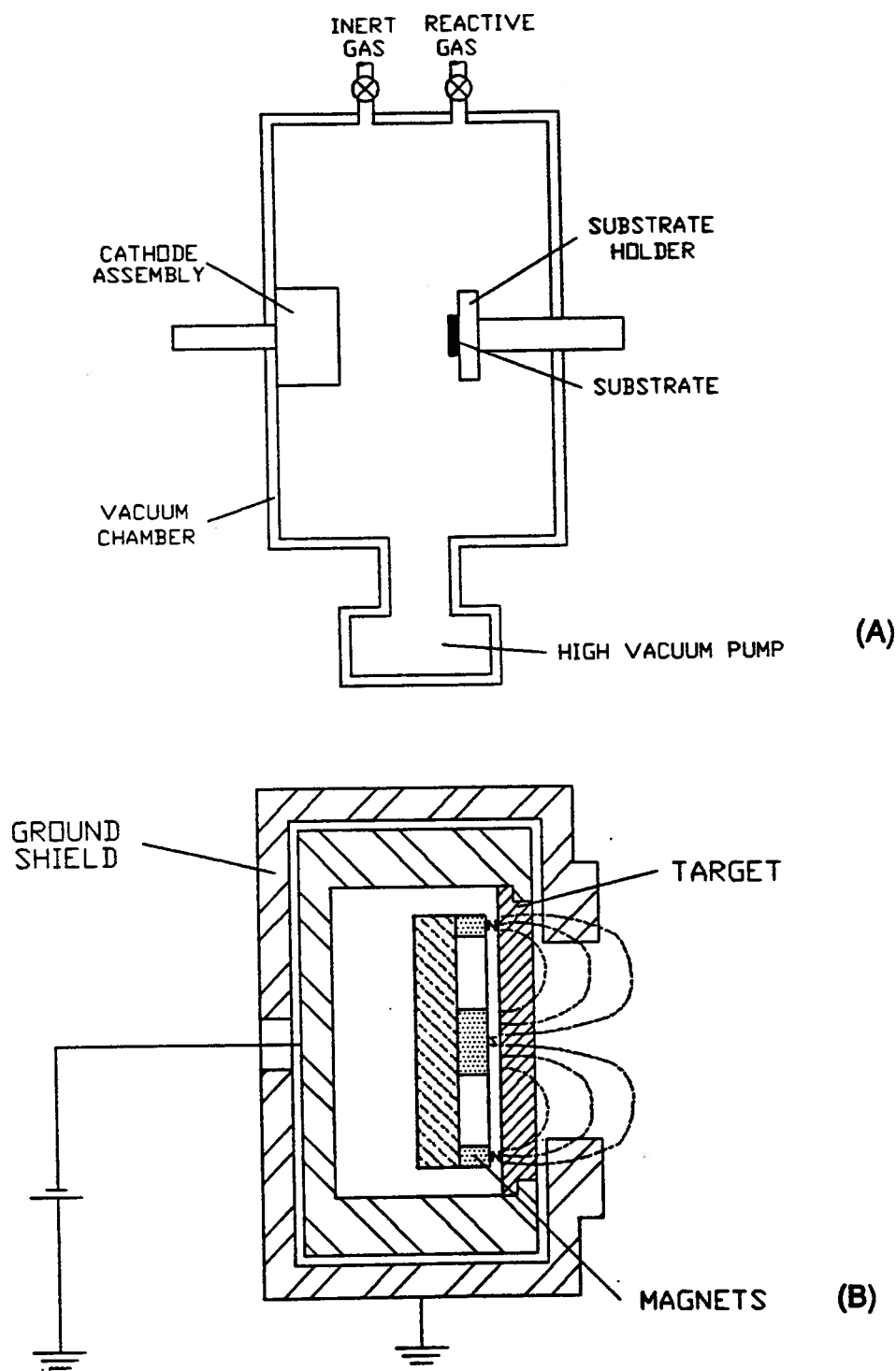


Fig. 1-1: (A) Schematic of a planar magnetron sputtering system. (B) Schematic of the cathode assembly of the planar magnetron sputtering system.

A d.c. planar magnetron sputtering system in Dr. Parson's lab was used for our samples and is shown in Fig. 1-1 [11]. The system was described in detail in Glenn Clarke's M.A.Sc thesis [11]. The pyrolytic graphite target is bombarded by energetic Ar ions and a portion of the ejected atoms then condense onto the substrate, which is positioned between 4 to 12 cm from the target surface, producing a thin film. The application of the magnetron can increase the deposition rate and overcome the film damage problem caused by the bombardment by highly energetic electrons [11].

### **1.1.3 Experimental Work on the Properties of DLC Films**

DLC films have attracted considerable attention because of their unusual properties and promising applications. A lot of work has been done to explore their structures, properties and it is clear that different deposition techniques and system configurations yield greatly variable film properties. Besides, a variety of characterization techniques are employed for investigation of the properties and the relationship between the properties and the preparation conditions. The following review is mainly extracted from reference [1].

#### **1.1.3.1 Mechanical Properties**

The hydrogenated DLC films typically have mass densities ranging from 1.4 to 2.0 g/cm<sup>3</sup>, with the least dense films found at the highest hydrogen content [4]. The densities of non-hydrogenated DLC films are usually higher than those of the hydrogenated ones. For the films prepared by the sputtering method, the film density is found to be dependent on the d.c. or r.f. sputtering power: with increasing sputtering power, the density of the films decreases [10] [12].



Hardness measurements of DLC films grown by d.c. magnetron sputtering indicate that pressure also affects film density [13].

Internal stresses and adhesion are important features since they determine the stability of the coating/substrate composite and thus the lifetime of the component. They may be affected by a number of processing parameters, such as deposition rate, angle of incidence, deposition temperature, and incorporation of impurities [4]. The hydrogenated DLC films are usually found in a high compressive stress state, the level of which increases with increasing hydrogen content, and the addition of fluorine increases compressive stress while nitrogen reduces compressive stress.

DLC films exhibit low values of friction coefficient [14]. Increasing humidity is found to result in a increase in friction coefficient and a decrease in wear factor [15].

### **1.1.3.2 Electrical Properties**

Since electrical resistivity is one of the crucial properties to characterize the electronic structure of carbon, it has been studied by many people.

In general, hydrogenated DLC films are characterized by high resistivity, and they have higher resistivities than non-hydrogenated films. The resistivity is increased greatly by hydrogen due to the stabilization of four-fold  $sp^3$  bonds by hydrogen [16]. It has been suggested that amorphous DLC films consist of a mixture of diamond and graphite bonds which act as the localized conduction states [19]. Thus, electrical resistivity may be a sensitive tool to measure the degree of amorphousness.

The resistivity of DLC films shows strong dependence on deposition conditions. The amorphous carbon films prepared by vacuum evaporation generally have a room temperature resistivity of between  $10^{-1}$  and  $1 \text{ } \Omega\text{cm}$  [17], while the film prepared by d.c. magnetron sputtering at low power can have  $10^4 \text{ } \Omega\text{cm}$  [10]. The electrical measurements taken by N.Savvides [10] showed consistence with Mott's model, which is, the conduction in amorphous carbon is caused by thermally activated hopping or tunneling of electrons between localized states which are associated with the  $\pi$  bonds of three-fold coordinated (graphitic) carbon atoms. For the d.c. magnetron sputtering method, It has also been found that conductivity varies with sputtering power, and the DLC film grown at low power possess insulating properties [10]. The spectra of the imaginary part of the complex dielectric function  $\epsilon_2$  is found to possess features typical of amorphous semiconductors [18]. It also showed in [13] that there is an increase in resistivity with increasing sputtering pressure, which cannot be explained simply in terms of film microstructure, and seem to imply changes in the bonding configuration of the carbon atoms. As for other deposition methods, the resistivity of films is found to rely on the deposition parameters such as r.f. power and substrate temperature in the glow discharge deposition of hydrocarbons and bias voltages in ion plating or rf decomposition of hydrocarbons [1].

#### **1.1.3.3 Optical Properties**

The potential application of DLC films as protective windows has led to a great deal of research on their optical properties. Furthermore, optical properties are closely related to the microstructures of the film, which determine the film properties.

Generally speaking, the optical properties of DLC films are closer to those of diamond, a large band gap semiconductor, than those of graphite, a semimetal. The optical constants  $n$  and  $k$  can be calculated from the reflectance and transmittance measurements. The extinction coefficient  $k$  shows a rapid decrease with increase of wavelength or decrease of photon energy in the visible region. In the infrared region, the absorptions are mainly associated with carbon, hydrogen, and oxygen vibrational modes. On the other hand, by increasing the hydrogen concentration, the band gap is increased to a maximum value, thus causing the films to become more transparent.

Optical properties in solids can be described in terms of the complex refractive index  $N=n+ik$  or the complex dielectric function  $\varepsilon=\varepsilon_1+i\varepsilon_2$ . The two representations are related by:

$$\begin{aligned}\varepsilon_1 &= n^2 - k^2 \\ \varepsilon_2 &= 2nk\end{aligned}$$

Absorption is characterized by the absorption coefficient  $\alpha(\nu) = 4\pi\nu k$  where  $\nu$  is the wavenumber. .

The visible absorption can be expressed by the Tauc formula:  $(\alpha E)^{1/2} = B(E - E_0)$ , where  $E$  is the photon energy. The optical band gap  $E_0$ , which is an important parameter to characterize amorphous solids, can be deduced from the intercept of the extrapolated linear fit to a plot of  $(\alpha E)^{1/2}$  versus  $E$  [20] [1]. The correlation of  $E_0$  with hydrogen content has been shown in [3] for rf-plasma-deposited films: with increasing bias voltage, the hydrogen content decreases and so does  $E_0$ .

The optical constants  $n$  and  $k$  vary with the preparation conditions. For sputter-deposited non-hydrogenated DLC films, the refractive index  $n$  appears to

increase with sputtering power, and shows minimum dispersion in infrared (IR) region for film deposited at less than 50W [10]. In most cases,  $n$  of hydrogenated amorphous carbon films remains roughly constant in the visible (VIS) region [21].

Details of the atomic arrangement and bonding structure can be derived from the analysis of the IR absorption bands. For hydrogenated DLC films, in the case of ion-plating-deposited layers [22], considerable absorption occurs only in the wavenumber range  $\nu \leq 1500 \text{ cm}^{-1}$ , which may be explained by the activation of phonons in the carbon network. Absorption lines due to C-H bonds were not observed. For microwave-deposited samples, strong absorption lines occur near  $2920 \text{ cm}^{-1}$  ( $sp^3$  C-H stretching vibrations),  $1450 \text{ cm}^{-1}$  (deformation vibrations of  $\text{CH}_2$  or  $\text{CH}_3$  groups), and around  $1300 \text{ cm}^{-1}$ ,  $1600 \text{ cm}^{-1}$ , corresponding to  $sp^2$ - or  $sp^2$ - and  $sp^3$ - hybridized carbon atoms. The bonding structure of the hydrogenated DLC films prepared by d.c. magnetron sputtering is given by S.Craig [20]. The optical studies done by O.Stenzel et al. on ion-plating-deposited samples showed that the strong absorption lines occur at the region  $750 \text{ cm}^{-1} < \nu < 1700 \text{ cm}^{-1}$ , and  $2800 \text{ cm}^{-1} < \nu < 3200 \text{ cm}^{-1}$ , and there is the expected window between  $1700\text{--}2800 \text{ cm}^{-1}$ . In addition, a dispersion model combining polymer-like features with absorption tendencies typical of amorphous solids was given, which was a superposition of Lorentz lines for vibrational resonances and an Urbach tail for the background absorption. J. Ullmann et al. studied the DLC films prepared by r.f. sputtering with target voltage as a parameter, and found that at low target voltage, the optical properties is similar to those of DLC films grown by d.c. plasma deposition and ion-plating deposition [24] .

Hydrogen incorporated in the amorphous DLC films may play a crucial role in the bonding configuration of the carbon atoms. It is believed that hydrogen can

help stabilize the tetrahedral coordination ( $sp^3$  bonding) of the carbon atoms which is the origin of the diamond like properties of the hydrogenated DLC films [10]. In order to understand the influence of hydrogen, the changes of C-H bonding as determined by IR spectroscopy have been studied with heating, for the films formed by ion beam processes [23]. It has been found that most of the carbon atoms in the film which are attached to hydrogens have a tetrahedral ( $sp^3$ ) structure, and some  $sp^2$  even  $sp^1$  bonding also exist depending on the deposition conditions. On heating the films for 1 hour in 500°C range, the  $sp^3$  carbon lose hydrogen forming  $sp^2$  bonds. On heating to 700 °C or more, the remaining hydrogen is lost and the films lose transparency which is proceeded by an increase in the refractive index. The study indicates that the presence of hydrogen is required to obtain carbon films that are transparent in the IR region and have good mechanical properties as well. In another work of IR spectroscopy [20], the role of hydrogen in optical properties was concluded as altering the opto-electronic properties of the hydrogenated DLC film by modifying the distribution of bonding and antibonding states of the basic singly bonded carbon network. This is indicated by the reduction in optical band gap resulting from 500°C bake-out of the hydrogen and an increase in C=C double bonding. However, after investigating the properties of the non-hydrogenated DLC film prepared by d.c. magnetron sputtering of graphite, N.Savvides and B.Window suggested that the presence of hydrogen is not strictly necessary for obtaining stable tetrahedral bonding in the amorphous carbon matrix, though the incorporation of hydrogen does improve the overall diamondlike properties by reducing the refractive index and increasing the IR optical transparency [10].

## **1.2 Characterization Methods for Optical Properties and Structure**

A great number of characterization methods are available to study amorphous DLC films. Among them, the most commonly used methods for optical properties are ellipsometry and IR spectroscopy. X-ray photoelectron spectroscopy and Auger electron spectroscopy are two of the most powerful surface composition analysis techniques. Some other techniques such as X-ray diffraction, transmission electron spectroscopy, laser Raman spectroscopy and electron-energy-loss spectroscopy are also important tools for studying thin film structures.

### **1.2.1 Ellipsometry**

In spectroscopic ellipsometry, a non-destructive optical probe, the change of polarization of elliptically polarized light due to reflection is measured and interpreted in terms of properties of the reflecting surface [1]. There are two characteristic parameters measured in ellipsometry: the change of relative amplitude and phase difference of two orthogonal components of light due to reflection. From these measured quantities, thickness and refractive index of a transparent film can be determined if the optical constants of the substrate are known. The optical constants of DLC films were measured by ellipsometry in the visible region [13] [25].

### **1.2.2 IR Spectroscopy**

Since ellipsometry is only efficient in the visible region, another method is necessary for the longer wavelengths. IR spectroscopy is always employed in this case because the optical constants of the films can be calculated from the

measured reflectance and transmittance spectra. Thus, the absorption behavior of the film can be obtained. The strong absorption lines in this region are mainly due to the excitations of vibrational modes, therefore, the information of atomic bondings in the films can be obtained through analysis of the characteristic vibrational frequencies of chemical bonds. Most works on the optical properties introduced in previous section were performed by this method.

### **1.2.3 Raman Spectroscopy**

Raman spectra of solids result from inelastic scattering of optical photons by vibration phonons and is a very useful technique for the characterization of material structures. Unlike IR spectroscopy, which is related to the change of electrical dipole moment, Raman spectroscopy is connected with a change in the polarizability of the molecule during vibrations. Raman spectra are sensitive to changes that disrupt the translational symmetry of the material and thus are useful for the study of disorder and crystallite formation in DLC films [1].

### **1.2.4 X-ray Photoelectron Spectroscopy (XPS) and Auger Electron Spectroscopy (AES)**

In XPS, x-rays are used to eject electrons by raising each electronic energy level from its original value by the amount of the photon energy. The outstanding strength of XPS is its ability to detect small chemical shifts in electron energy level. However, it lacks of spatial resolution.

The Auger process is easily understood by an analogy with X-ray emission, in which an incident electron ejects an atomic electron creating a core hole and

initiates a de-excitation process. AES is useful because of the rapidity of data collection owing to the high efficiency of the Auger process.

Both XPS and AES can provide information on bonding between atoms and on core level binding energy, and thus can be used to distinguish both the elements and its chemical states [1].

### 1.3 Purpose and Outline of the Thesis

The purpose of this thesis is to study the optical properties of amorphous DLC thin films deposited by the d.c. magnetron sputtering method, and obtain the information of atomic bondings in the films, by using a Fourier-transform infrared (FT-IR) spectrometer. This work was a cooperation between Dr. Parsons's thin film lab and Dr. Eldridge's FT-IR spectroscopy lab. The DLC films were all grown by Glenn Clarke in Dr. Parsons's lab and then tested by FT-IR spectrometer in Dr. Eldridge's lab. Glenn Clarke also developed programs to obtain the film thicknesses and  $n,k$  results in the MIR region. Furthermore, we investigated the correlation between the deposition parameters and the film properties so that it is possible to determine the optimum conditions for deposition of infrared transparent DLC films in Dr. Parsons's lab.

In the second chapter of this thesis, the principles and advantages of a Fourier-transform infrared spectrometer are described, together with the details of the Bruker 113V interferometer used for the experiments.

In the third chapter, the details of reflectance and transmittance measurements are given. There is also a brief description of the samples tested.



The fourth chapter is the theory of the reflectance and transmittance calculation, using the matrix method, as well as the optical absorption models applied to interband and longer wavelengths regions.

The fifth chapter contains the experiment results, which include the reflectance and transmittance spectra for 6 samples, the results of optical constants calculated from the reflectance and transmittance data, and the fittings of the absorption coefficients using a dispersion model described in Chapter 4. Therefore, information about the chemical bonds can be obtained. Finally, by comparing these samples, the effects of the deposition parameters on the film properties are discussed.

The final chapter is the conclusion, a summary of the work and the meaning of the research.

## **Chapter 2**

### **EXPERIMENTAL METHOD AND INSTRUMENTATION**

#### **2.1 Fourier Transform Spectroscopy**

Fourier-transform spectroscopy is one of the fundamental and important tools for studying condensed matter, since it is simple yet powerful. Resulting from its non-contact and non-destructive characteristics, it is most commonly used to study the optical properties of materials over a wide frequency range.

Mainly due to the two-beam interferometer and the computer facilities used, Fourier-transform (FT) spectrometer has the following advantages [26] over the traditional instruments such as diffraction grating monochromators:

- It receives information from the entire spectral range during each time element of a scan, while the grating instrument can just receive the information in a very narrow band. This is known as Fellgett or multiplex advantage, which will be described in detail later.
- It can operate with small  $f$  numbers (i.e. with large solid angles at the source and detector), thus, it can collect a large amount of energy at high resolution.
- It has a large resolving power as a result of the first two advantages.
- It has high wavenumber accuracy achieved by the precise change in the interference pattern, which is due to the laser interferogram used and the accuracy of the laser frequency.
- The stray or unwanted flux problem has been greatly reduced because of the interference phenomena involved in the interferometer. The unwanted light

signals do not get modulated by the moving mirror, nor do they appear in the interferogram.

- By the means of rapid-scan technology, the measurement can be performed extremely fast and electrical filtering can be used. This advantage will be discussed in detail later.

These advantages, as well as some other additional ones, make FT spectroscopy widely used in many fields, especially in Physics and Chemistry. For more information about the merits and applications, see the reference by Bell [26].

In order to understand this technology better, it is necessary to review the basic theories of the data collection and manipulation of the spectra. Therefore, the following sections will describe the Michelson interferometer, FT analysis, and other related data processing techniques.

### **2.1.1. Michelson Interferometer**

The main component of the spectrometer is the Michelson interferometer. Fig. 2-1A shows the basic Michelson interferometer with the sample in the recombined beams after the beamsplitter.

The beam from the source S is chopped and collimated, then directed to the beamsplitter, where half of it (beam1) is reflected and goes to mirror M1 while the other half is transmitted and goes to mirror M2. Both of the two beams will be reflected back to the beamsplitter. After the beamsplitter, the transmitted part of beam1 and the reflected part of beam2 will recombine with each other and interfere, since they are spatially coherent.

M2 is a fixed mirror. Suppose beam2 travels a distance  $L/2$  before hitting M2, then the total optical path of beam2 is  $L$  when it hits the beamsplitter again.

M1 is a movable mirror which can be controlled to move back and forth around  $L/2$  by a distance  $x/2$ . So the total optical path difference between the two beams at the point they recombine is  $x$ . The intensity of the recombined beam, which is measured by the detector, is a function of  $x$  and called the interference pattern or interferogram. For a monochromatic source with intensity  $I(\nu)$  at wavenumber  $\nu$  ( $\nu=1/\lambda$  in  $\text{cm}^{-1}$ ), the interferogram has the form:

$$I(x) = I_0(1 + \cos 2\pi\nu x) \quad (2.1)$$

and is shown in Fig. 2-1C. For a polychromatic source, the interferogram is the integral of the monochromatic interferogram over the frequency or wavenumber range :

$$\begin{aligned} I(x) &= \int_{\nu_{\min}}^{\nu_{\max}} I(\nu)(1 + \cos 2\pi\nu x) d\nu \\ &= \frac{1}{2}I(0) + \int_{\nu_{\min}}^{\nu_{\max}} I(\nu) \cos 2\pi\nu x d\nu \end{aligned} \quad (2.2)$$

where  $I(0)$  is the intensity at zero path difference,  $\nu_{\min}$   $\nu_{\max}$  are the minimum and maximum wavenumber generated by the polychromatic source. Fig. 2-1B shows the interferogram in this case. Though the detector usually detects the interferogram from the polychromatic source, the interference pattern generated by the monochromatic light, such as a He-Ne laser, is also very important, because it allows very precise tracking of the moveable mirror. Thus, it is used in all modern Fourier-transform infrared (FT-IR) spectrometers to control the movement of the moveable mirror and measure the change in the optical path difference.

Fig. 2-1C shows how the IR interferogram is digitized precisely at the zero crossings of the laser interferogram. Since the accuracy of the sample spacing between two zero crossings is determined by the precision of the known laser

wavelength, FT-IR spectrometers have a wavenumber calibration of high precision. This advantage is known as Connes advantage [27].

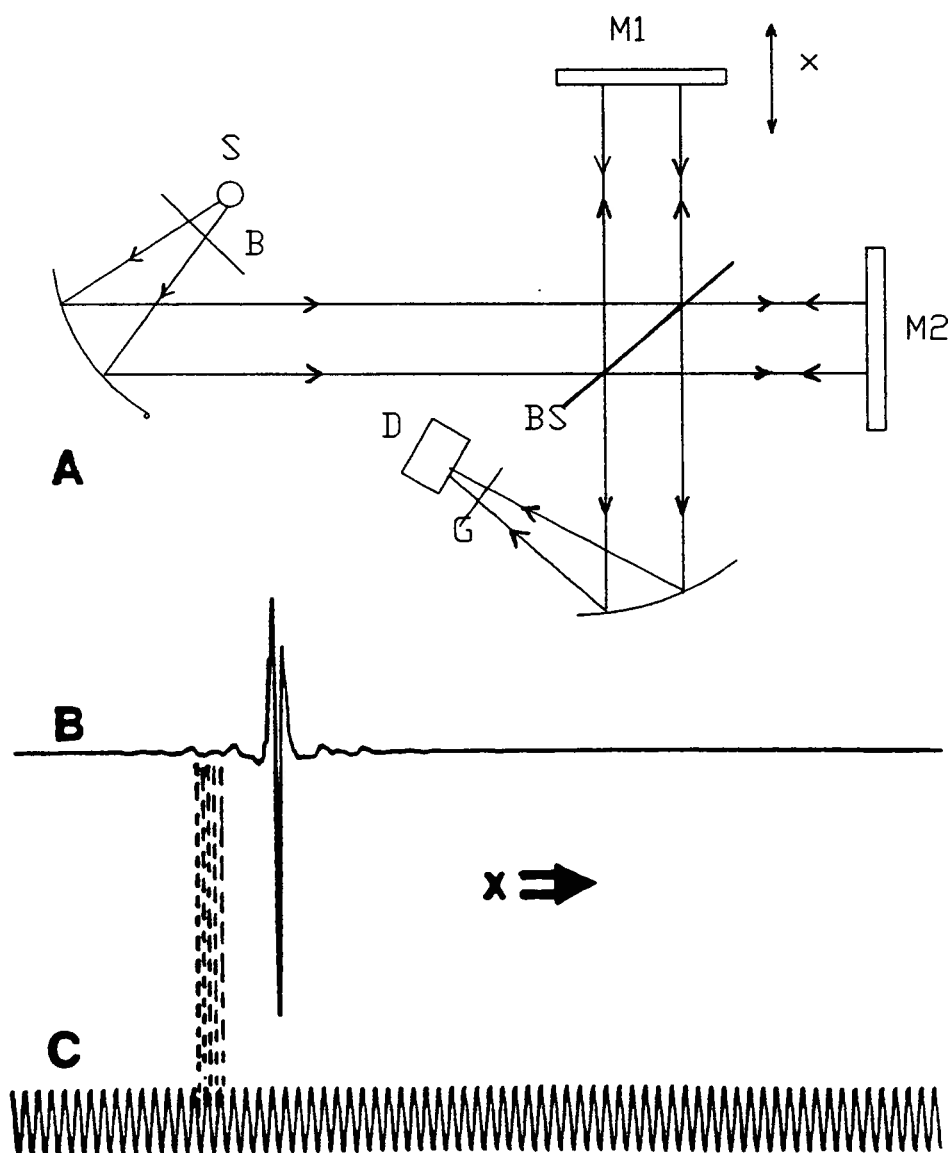


Fig.2-1: (A) Basic Michelson Interferometer. S: source. B: chopper. BS: beamsplitter. M1: movable mirror. M2: fixed mirror. G: sample. D: detector.  $x$ : mirror displacement. (B) Signal measured by detector D. This is interferogram of a polychromatic source. (C) Interference pattern of a laser source. Its zero crossings define the positions where the interferogram is sampled (dashed lines)

## 2.1.2 Fourier Analysis

### 2.1.2.1. Fourier Transformation

The interferogram is measured as a function of path difference  $x$ . In order to obtain the spectrum, which is a function of wavenumber (or frequency), the Fourier-transform integral theorem must be applied.

Mathematically, a function  $I(x)$  can be written as

$$I(x) = \int_{-\infty}^{+\infty} I(v) \exp(-i2\pi vx) dv \quad (2.3)$$

If we know  $I(x)$  and want  $I(v)$ , it is given by

$$I(v) = \int_{-\infty}^{+\infty} I(x) \exp(i2\pi vx) dx \quad (2.4)$$

where the second integral is called the continuous Fourier transform and the first one is called the inverse Fourier transform. However, experimentally, the waveform (the interferogram) is discretely sampled at evenly spaced intervals. Suppose we have  $N$  consecutive sampled values, the discrete Fourier transform (DFT) can be defined to approximate the original Fourier transform:

$$I(k\Delta v) = \sum_{n=0}^{N-1} I(n\Delta x) \exp(i2\pi nk / N) \quad (2.5)$$

where the continuous variables  $x$ ,  $v$  have been replaced by discrete values  $n\Delta x$  and  $k\Delta v$  respectively. Thus, the DFT is acceptable for the purpose of digital machine computation. The spacing  $\Delta v$  in the spectrum is related to  $\Delta x$  by

$$\Delta v = 1 / (N\Delta x) \quad (2.6)$$

The DFT expresses a given function as a sum of sine and cosine functions. The resulting new function  $I(k\Delta v)$  will form the spectrum. Alternatively, if the  $I(k\Delta v)$

is known, the formula for the inverse DFT, which recovers the interferogram  $I(n\Delta x)$ , is:

$$I(n\Delta x) = \frac{1}{N} \sum_{k=0}^{N-1} I(k\Delta \nu) \exp(-i2\pi nk / N) \quad (2.7)$$

Fig. 2-2 shows the spectrum with one or two monochromatic lines, a Lorentzian line, a polychromatic source, and their corresponding interferograms.

The general qualitative rule for an approximate description of the correspondence between  $I(n\Delta x)$  and  $I(k\Delta \nu)$  is that a finite spectral line width (as is always present for real samples) is due to damping in the interferogram: The broader the line, the stronger the damping. This is illustrated in Fig. 2-2C and 2-2D. Another related rule can be seen by comparing the widths at half height (WWH) of  $I(n\Delta x)$  and  $I(k\Delta \nu)$ : The WWH's of a "hump-like" function and its FT are inversely proportional. Using this rule, one can explain why the interferogram in Fig. 2-2D has a very sharp peak around the zero path difference position ( $x=0$ ), while the wings of the interferogram, which contains most of the useful spectral information, has a very low amplitude.

By examining Eq.(2.7), one can also see that when  $n=0$ , the intensity  $I(0)$  measured at the interferogram centerburst actually is a measure of the average spectral intensity.

Eq.(2.5) is seldom used in practice, since it appears to be an order of  $N^2$  process for  $N$  points. In fact, DTF can be computed in an order of  $\text{Mog}_2 N$  operation with an algorithm called the fast Fourier transformation (FFT) so that substantial computer time can be saved. There are a number of variations of the basic FFT algorithm and the most famous and commonly used one is the Cooley-Tukey algorithm, in which  $N$  must be chosen as a power of 2. In this case, the

spectra taken with a laser-controlled FT-IR spectrometer will show a sample spacing of  $\Delta\nu = m \cdot \text{laser wavenumber} / 2^N$ .

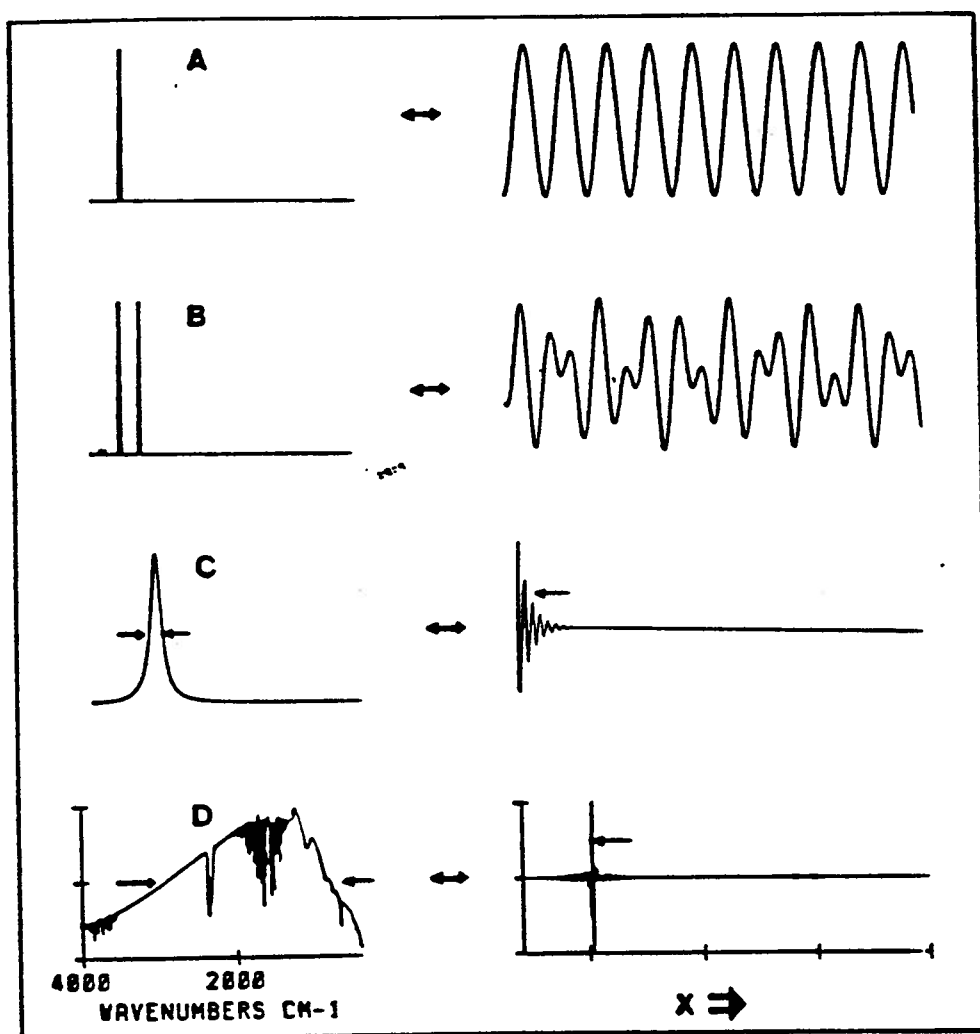


Fig. 2-2: Examples of spectra (left) and their corresponding interferograms (right). (A) One monochromatic line. (B) Two monochromatic lines. (C) Lorentzian line. (D) Broadband spectrum of polychromatic source.



### 2.1.2.2 Sampling Interval and Aliasing

In order to understand "aliasing" and other effects better, a very useful tool in modern scientific analysis should be introduced first: the convolution theorem. This theorem states that the Fourier transform (FT) of the product of two functions, e.g.,  $I(x)$  and  $\Delta(x)$ , is the convolution of their individual Fourier transforms  $I(v)$  and  $\Delta(v)$ , where the convolution is defined as:

$$I(v) \otimes \Delta(v) = \int_{-\infty}^{+\infty} \Delta(u) I(v-u) du \quad (2.8)$$

The convolution theorem is used in Fig. 2-3 to illustrate how to determine the Fourier transform of a sampled interferogram. In most practical situations, only samples of the continuous interferogram can be obtained. The sampled interferogram can be related to the continuous interferogram by the shah function  $\text{III}(x)$ :

$$I_s(x) \equiv \text{III}\left(\frac{x}{\Delta x}\right) I_c(x) \quad (2.9)$$

where  $I_s(x)$  is the sampled interferogram,  $I_c(x)$  is the continuous or the complete interferogram, and  $\Delta x$  is the sampling interval.  $\text{III}(x)$  is defined as:

$$\text{III}(x) = \sum_{n=-\infty}^{+\infty} \delta(x-n) \quad (2.10)$$

where  $\delta(x-n)$  is the Dirac delta function and  $n$  is an integer. From Eqs. (2.10) and (2.9), we can see that  $\text{III}(x/\Delta x)$  will just allow in  $I_s(x)$  those values of the interferogram for which  $x=0, \pm\Delta x, \pm 2\Delta x, \dots$ . After applying the convolution theorem and the properties of shah function [26], the FT of the sampled interferogram and the complete interferogram has the following relationship:

$$I_s(v) = \sum_{n=-\infty}^{+\infty} I_c(v - n\Delta v) \quad (2.11)$$

where 
$$\Delta\nu = \frac{1}{\Delta x}. \quad (2.12)$$

That is, we obtain the complete spectrum every time  $\nu$  equals to  $n\Delta\nu$  for all integers  $n$ . In other words, the spectrum is periodic starting at  $n\Delta\nu$ .

Fig. 2-3A shows the ordinary interferogram and Fig. 2-3B gives its complete spectrum, which include both positive and negative wavenumbers. The negative wavenumber part of the spectrum is actually just the mirror image of the positive wavenumber part of the spectrum, and is usually discarded. However, we cannot ignore it here. Fig. 2-4A shows the sampled interferogram and Fig. 2-4B is the computed spectra from the sampled interferogram. The spectrum is completely symmetric about  $\nu=0, \pm\nu, \pm2\nu, \dots$ . The solid lines are the contributions from the positive wavenumbers and the dashed lines are their mirror images. It is very clear that if  $\Delta\nu$  is big enough or  $\Delta x$  is small enough, the repeated spectra will not overlap with each other. But if  $\Delta\nu$  is too small, the original spectra of the positive and negative wavenumber will overlap and the total spectrum will be the sum of the dashed lines and the solid lines, as shown in Fig. 2-4C, and one cannot separate them. This phenomena is called aliasing. In this case, one could not determine the true spectrum from the spectrum which is computed from the sampled interferogram.

As illustrated in Fig. 2-4C, the sampled spectra is symmetric about  $\nu=0, \pm\nu, \pm2\nu, \dots$  and is periodic with period of  $\Delta\nu$ . Then the Nyquist wavenumber or folding wavenumber is defined as:

$$\nu_r = \frac{1}{2}\Delta\nu = \frac{1}{2\Delta x}. \quad (2.13)$$

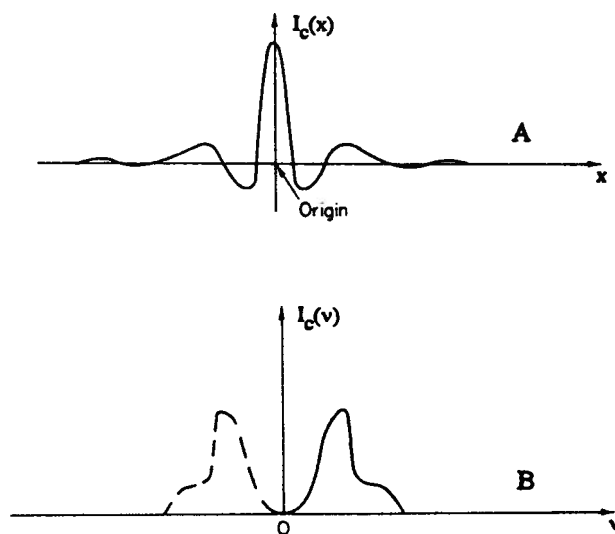


Fig. 2-3: (A) Interferogram. (B) Computed spectrum from a continuous, complete scan. It is a two-sided spectrum.

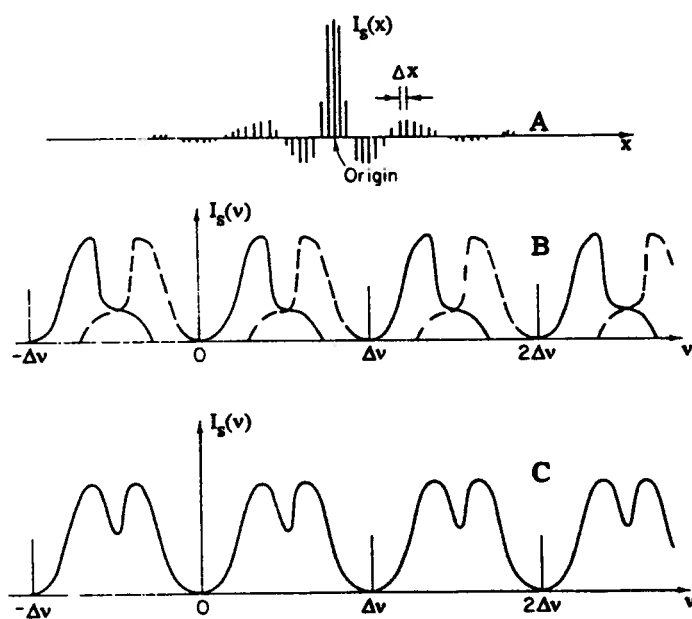


Fig. 2-4: (A) Sampled interferogram. (B) Computed spectral components from the sampled interferogram. The solid line represents the positive  $v$  spectra from Fig. 2-3B and the dashed line represents the negative  $v$  spectra from Fig. 2-3B. (C) The total spectrum which is the sum of the spectral components in (B).

In order to avoid aliasing,  $\Delta v$  must be big enough to avoid overlapping the repeated spectra. One method is to require that the spectrum is zero about a maximum wavenumber  $v_{\max}$  which is smaller than the Nyquist wavenumber  $v_f$ :

$$v_{\max} \leq v_f = \frac{1}{2\Delta x} \quad (2.14)$$

or

$$\Delta x \leq \frac{1}{2v_{\max}} = \frac{1}{2} \lambda_{\min}. \quad (2.15)$$

So the sampling interval must have an upper bound. In addition, Eq. (2.15) implies that one must sample twice in every cycle of the smallest wavelength variation in the interferogram. From the previous section, we know that the sampling positions are determined from the zero crossings of an He-Ne laser wave with a wavelength  $\lambda$  of 1/15800 cm. As a zero crossing occurs every  $\lambda/2$ , it samples twice in every cycle and the minimum possible sample spacing  $\Delta x_{\min}$  is 1/31600 cm, which corresponds to a Nyquist wavenumber of 15800 cm<sup>-1</sup>, i.e., the maximum bandwidth which can be measured without overlap has a width of 15800 cm<sup>-1</sup>. When the investigated bandwidth is much smaller than 15800 cm<sup>-1</sup>, as in the case of mid-infrared and far-infrared,  $\Delta x$  can be chosen to be an  $m$ -fold multiple of  $\Delta x_{\min}$ , which leads to an  $m$ -fold reduction of the interferogram size.

If the spectrum has a lower limit of  $v_{\min}$  instead of zero, that is, it is zero below a lower band limit  $v_{\min}$  and  $v_{\min}$  is not zero as assumed before, one has [26]:

$$\Delta x \leq \frac{1}{2(v_{\max} - v_{\min})} \quad (2.16)$$

if and only if

$$\nu_{\min} = \frac{n-1}{n} \nu_{\max} \quad (2.17)$$

Based on the condition of Eq. (2.17) and the fact that  $\nu_{\max}$  must be a natural fraction of the He-Ne laser wavenumber, one can fill the previous empty space from 0 to  $\nu_{\min}$  with  $n-1$  further copies of the original spectrum. Thus, it is possible to achieve greater reduction of the data size. This technology is called undersampling.

One advantage of an advanced FT-IR software package is that it can take care of the proper sampling and undersampling automatically so that only the upper and lower limits of the interested spectral range need to be specified. Thus the only thing one needs to do is to make sure that proper optical or electronic filters have been inserted so that the spectrum outside the range  $\nu_{\min}$  to  $\nu_{\max}$  is really zero.

### 2.1.2.3 Picket-fence Effect and Zero Filling

When the interferogram contains wavenumbers which are not coincident with the sampling wavenumber  $k\Delta\nu = k/(N\Delta x)$ , an erroneous signal reduction can occur [27]. This is called the "picket-fence" effect since one seems to be viewing the true spectrum through a picket fence, therefore clipping those spectral contributions lying between the sampling position  $k\Delta\nu$ . The picket-fence effect can be overcome by the method of zero filling, which is adding zeros to the end of the interferogram before applying DFT. As a result, the number of data points in the interferogram  $N$  increases, and  $\Delta\nu$ , which is  $1/(N\Delta x)$ , becomes smaller. This means that we will have more points to determine the spectral peaks. Thus, zero filling has the effect of interpolating the spectrum and reducing the error. As a basic rule, the zero filling factor (ZFF) should be at least 2, that is, one should

always at least double the original interferogram size. Zero filling is superior to polynomial interpolation techniques because it will not change the instrumental line shape and no errors are introduced.

#### 2.1.2.4. Leakage and Apodization

The leakage problem is caused by the truncation of the interferogram at finite optical path difference. The basic Fourier-transform integrals have the infinite optical path difference, however, in practice, the interferogram must be obtained over a limited range. In fact, the truncated interferogram  $I(x)$  can be obtained by multiplying the infinite interferogram  $F(x)$  with the infinite optical path difference by a rectangular function  $rect(x)$ , which is

$$\begin{aligned} rect(x) &= 1 & (|x| \leq x_M) \\ &= 0 & (|x| > x_M) \end{aligned} \quad (2.18)$$

where  $x_M$  is the maximum optical path difference. According to the convolution theorem mentioned before, the Fourier transform (FT) of a product of two functions is the convolution of their individual Fourier transform. Thus, the actual spectrum, which is the FT of the finite interferogram, is:

$$I(v) = F(v) \otimes ILS(v) \quad (2.19)$$

where  $F(v)$  is the FT of the infinite interferogram and  $ILS(x)$  is the FT of the rectangular function, which is usually called the Instrumental Line Shape function ( $ILS$ ) or spectral window. In the case of rectangular function, the  $ILS$  is the well known sinc function:

$$ILS(v) = \frac{x_M \sin(2\pi v x_M)}{2\pi v x_M} \quad (2.20)$$

which is plotted in Fig. 2-5A. We can see from the figure that ,apart from the maximum central line, there are a lot of side lobes which look like "feet" in the spectrum. These side lobes cause a "leakage" of the spectral intensity [27], i.e., the intensity is not strictly localized but contributes also to these side lobes. The side lobes or feet of the sinc function drop 22% maximum below zero which is large and unacceptable. Besides, the side lobes do not correspond to actually measured information but rather represent artifacts due to the sharp sides of the rectangular function. Therefore, it is necessary to use gentler functions instead of abruptly truncating functions in order to decrease the side lobes. This process is known as apodization, which means " removal of the feet" (hence the name "apodization" is from Greek "podos" for foot.)

There are many apodization functions for this purpose. The common ones are:

Triangular (TR):

$$\begin{aligned} TR(x) &= 1 - \frac{|x|}{x_M} & (|x| < x_M) \\ &= 0 & (|x| \geq x_M) \end{aligned} \quad (2.21)$$

Trapezoidal or Four-Point(FP):

$$\begin{aligned} FP(x) &= 1 & (|x| < BPC) \\ &= 1 - \frac{|x| - BPC}{BPD - BPC} & (BPC \leq |x| \leq BPD) \\ &= 0 & (|x| > BPD) \end{aligned} \quad (2.22)$$

This is a square window between 0 and breakpoint  $BPC$ , and then a triangular function between breakpoints  $BPC$  and  $BPD$ . In figure , we choose  $BPD = x_M$ .

Hamming or Happ-Genzel (HG):

$$\begin{aligned}
 HG(x) &= 0.54 + 0.46 \cos\left(\frac{\pi x}{x_M}\right) & (|x| \leq x_M) \\
 &= 0 & (|x| > x_M)
 \end{aligned} \tag{2.23}$$

Three- and four-term Blackmann-Harris (BH):

$$BH(x) = A_0 + A_1 \cos\left(\frac{\pi x}{x_M}\right) + A_2 \cos\left(\frac{2\pi x}{x_M}\right) + A_3 \cos\left(\frac{3\pi x}{x_M}\right) + A_4 \cos\left(\frac{4\pi x}{x_M}\right) \tag{2.24}$$

This set of windows is a generalization of the Happ-Genzel function. The coefficients have been chosen for optimum suppression of the side lobes [27]:

Table 2-1 coefficients for Blackmann-Harris function

|           | A0      | A1      | A2      | A4      |
|-----------|---------|---------|---------|---------|
| 3-term BH | 0.42323 | 0.49755 | 0.07922 | 0.0     |
| 4-term BH | 0.35875 | 0.48829 | 0.14128 | 0.01168 |

Fig. 2-5 shows several apodization functions, including the rectangular function, and their ILS's. It should be noticed that, in Fig. 2-5B to E, the negative lobes are absent, the sizes of the side lobes is smaller, and at the same time, the main lobes of all of the ILS's are broader than that of the sinc function in Fig. 2-5A. The price paid for the leakage reduction is lower resolution.

### 2.1.3. Resolution

The resolution of the instrumental line,  $\delta\nu$ , is originally defined as the full width at half height (FWHH) of the ILS function. For the sinc ILS function corresponding to the rectangular truncation or no apodization, we can have



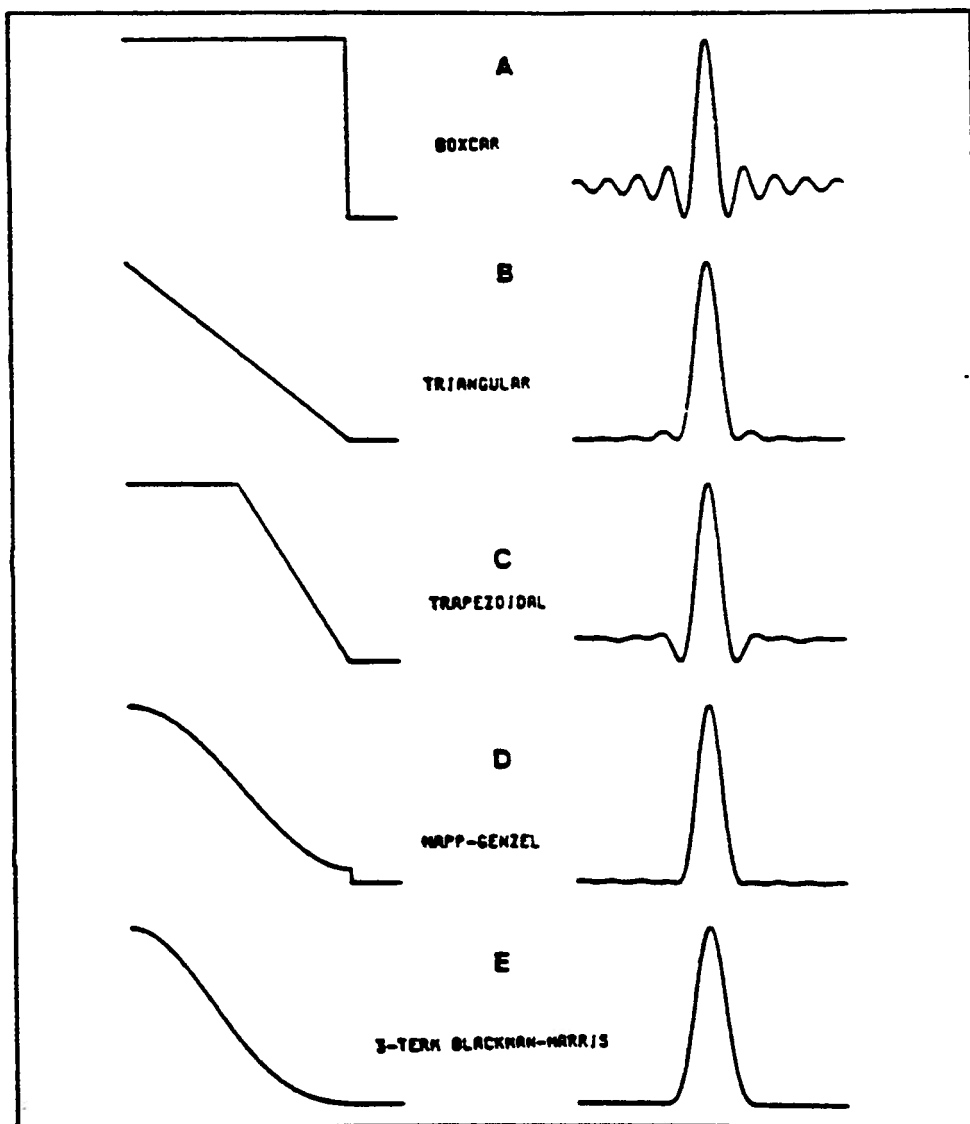


Figure 2-5: Several apodization functions (left) and the "Instrumental Lineshape" produced by them (right).

$$\delta\nu = \frac{1.21}{2x_M} \quad (2.25)$$

And for the triangular apodization, the ILS function has the form of  $x_M \sin c^2(\pi\nu x_M)$ , then

$$\delta\nu = \frac{0.90}{x_M} \quad (2.26)$$

On the other hand, in terms of the separation of two close lines, the resolution can be defined by the Rayleigh criterion. The Rayleigh criterion states that two resonance (2 lines with equal intensity) in a spectrum are resolved if they are separated such that the peak of one resonance falls at the first zero of the second one. Under this criterion, for the triangular apodized spectrum,  $\delta\nu$  is actually the distance between the peak frequency and the frequency at zero intensity:

$$\delta\nu = \frac{1}{x_M} \quad (2.27)$$

If the Rayleigh criterion is applied to two sinc ILS functions, which is the case of no apodization, we will have:

$$\delta\nu = \frac{1}{2x_M} \quad (2.28)$$

By comparing Eqs.(2.25) and (2.28), we can see that the full width at half height (FWHH) of the rectangular ILS function is  $1.21/2x_M$  and the Rayleigh criterion separates two equal rectangular ILS functions by  $1/2x_M$ . Thus, the frequency spreads  $\delta\nu$  in these two criteria are equal to each other to within about 20%. As for the triangular apodization, the two frequency spreads agree to within about 10%.

From the above discussion, we can conclude that the resolution for the unapodized spectrum is higher than that for the apodized spectrum, and it is inversely proportional to the maximum optical path difference used to obtain the interferogram. Therefore, the choice of particular apodization function depends on the resolution required. Despite the fact that the Black-Harris function has nearly the same resolution as the triangular- and Happ-Genzel functions, it is considered to be the top performer among these three windows, because the highest side lobe is the most suppressed and it is furthermore nearly zero at the interval ends (see Fig. 2-5).

Resolution does not depend only on the maximum path difference and apodization function. It may also be restricted by the aperture size. In the previous discussion, we only considered a plane wave incident normally on the mirror. With any finite-sized aperture, the radiation from the off center points will be incident on the mirror at some angle  $\theta$  and will cause a reduced optical path difference between the two arms of the interferometer. As a result, the effect of the entire aperture is to spread a monochromatic line at  $\nu_1$  into a range from  $\nu_1$  to  $\nu_1 - \nu_1 \cos \theta_{\max}$ , where  $\theta_{\max}$  is the maximum incident angle. Furthermore, considering the resolution of two lines in the spectrum, we can arrive at the result given by Jacquinot [26]:

$$R\Omega = 2\pi \quad (2.29)$$

where  $\Omega$  is the solid angle subtended by the aperture and  $R$  is resolving power defined by:

$$R = \frac{\nu}{\delta\nu} \quad (2.30).$$

Thus, the resolution is:

$$\delta v = \frac{v\Omega}{2\pi} \quad (2.31)$$

So, we can improve the resolution by reducing the aperture size, but the cost is the reduction of the optical throughput.

#### 2.1.4 Phase Correction

Phase correction is necessary because the FT of a measured interferogram generally generates a complex spectrum  $C(v)$  [27] from a double-sided interferogram rather than a real spectrum  $S(v)$ , in order to eliminate phase errors. Phase errors are introduced when the symmetry about the zero optical path difference point  $x=0$  is lost. The main sources for this asymmetry are [27]:

- (1) None of the sampling positions is coincident exactly with the position of the zero path difference. This is the main cause and leads to a phase shift linear in  $v$ .
- (2) Only a one-sided interferogram is measured, i.e., only one side is recorded to its full extent.
- (3) The interferogram may be asymmetric due to poor optical alignment, and/or the phase delay of either the optics, the detector/amplifier unit, or the electronic filters.

A complex spectrum  $C(v)$  can be expressed by the sum of the purely real part  $R(v)$  and the imaginary part  $I(v)$ :

$$C(v) = R(v) + iI(v) \quad (2.32)$$

or by the product of the true amplitude spectrum  $S(v)$  and the wavenumber dependent phase factor  $\exp(i\phi(v))$  containing the phase errors:

$$C(v) = S(v)\exp(i\phi(v)) \quad (2.33)$$

Since the power spectrum  $P(v) = C(v) \cdot C^*(v)$  is independent of phase errors, it is usually used to extract the amplitude spectrum  $S(v)$ :

$$S(\nu)=[C(\nu) \cdot C^*(\nu)]^{1/2}=[I^2(\nu)+R^2(\nu)]^{1/2} \quad (2.34)$$

The process of correcting phase errors and extracting  $S(\nu)$  is known as phase correction. It also can be done by multiplying  $C(\nu)$  by the inverse of the phase exponential and taking the real part of the result:

$$S(\nu)=\text{Re}[C(\nu)\exp(-i\phi(\nu))] \quad (2.35)$$

$\phi(\nu)$  can be calculated from  $C(\nu)$ :

$$\phi(\nu)=\arctan[I(\nu)/R(\nu)] \quad (2.36)$$

This procedure (Eq.(2.35)) is called 'multiplicative phase correction' or the 'Mertz-method'.

It should be noted that one-sided interferograms are extremely useful in order to shorten overall scan time. With the help of an on-line computer, the phase correction can be quickly computed and the entire spectrum can then be symmetrized.

### 2.1.5 Comparison Between Grating and FT-IR Spectrometer- Jacquinot and Fellgett Advantages

#### 2.1.5.1 Jacquinot Advantage

In a lossless optical system, the brightness of an object equals the brightness of the image and therefore the flux throughput and brightness can be considered at any point [26]. Throughput is defined as the product of the solid angle subtended by the source and the projected area of the collimator. If there is no loss between the elements in the system of interferometer, the throughput is found to be a constant for the instrument from the source to the detector. Using

the solid angle-resolving power product which is given by Eq. (2.29), we can obtain the throughput of a Michelson interferometer:

$$E_M = A_M \Omega_M = 2\pi A_M / R_M \quad (2.37)$$

where  $E_M$  stands for the throughput of Michelson interferometer,  $A_M$  is the area of the collimator mirror and  $R_M$  is the resolving power of the interferometer.

For the grating spectrometer, the entrance slit limits the power through the instrument. So the slit area defines the effective source area, and the slit subtends the solid angle from the collimating mirror. Assuming the same area and focal length for the collimators and the same resolving power, the ratio of the interferometer and grating throughput is given by [26]:

$$\frac{E_M}{E_G} \approx 2\pi \left( \frac{F}{f} \right) \quad (2.38)$$

where  $F$  is the focal length of the collimator and  $f$  is the slit length.

Even for the best grating spectrometers,  $F/f$  is never less than 30. That is to say, about 200 times more power can be put through the interferometer than through the best grating spectrometer. In addition, the optical system for the interferometer can be much smaller than that for the grating spectrometer. This throughput advantage is also known as the Jacquinot advantage.

#### 2.1.5.2 Fellgett Advantage

The Fellgett advantage, also called the multiplex advantage, is concerned with the signal to noise ratio  $S/N$ .

Suppose there is a broad spectrum band from the wavenumber  $\nu_1$  to  $\nu_2$ . With resolution  $\delta\nu$ , the number of spectrum elements in the band is:

$$M = \frac{\nu_1 - \nu_2}{\delta\nu} \equiv \frac{\Delta\nu}{\delta\nu} \quad (2.39)$$

Let  $T$  be the total time required for a scan from  $\nu_1$  to  $\nu_2$ , and assume the noise is random and independent of the signal level. In the grating instrument, each small band of width  $\delta\nu$  is observed individually for a time  $T/M$ . Thus, the integrated signal received in the band  $\delta\nu$  is proportional to  $T/M$  and the noise is proportional to  $(T/M)^{1/2}$ . The signal to noise ratio  $S/N$  for a grating instrument will be [26]:

$$(S/N)_G \propto (T/M)^{1/2} \quad (2.40)$$

But for the interferometer, since it receives the entire signal from the source continuously, the integrated signal in a small band  $\delta\nu$  is proportional to  $T$ , and the signal noise is proportional to  $T^{1/2}$ . Therefore, the signal to noise ratio  $S/N$  for a interferometer will be:

$$(S/N)_I \propto T^{1/2} \quad (2.41)$$

Comparing Eqs.(2.40) and (2.41), the multiplex or Fellgett advantage is:

$$\frac{(S/N)_I}{(S/N)_G} = M^{1/2} \quad (2.42)$$

Since  $M$  is of the order of the resolving power, typically about  $10^3$  order, Eq.(2.42) predicts that the interferogram has a much higher signal-to-noise ratio than the grating or prism instruments.

## 2.2 Instrumentation

The Bruker IFS 113V Fourier-transform infrared (FT-IR) spectrometer was used in all the reflectance and transmittance measurements reported here.

### 2.2.1 Bruker IFS 113V FT-IR Spectrometer

Bruker IFS 113V FT-IR spectrometer is a powerful and flexible vacuum bench research spectrometer which covers the entire wavenumber range from the

far infrared to the near infrared ( $\sim 10\text{cm}^{-1}$  -  $15800\text{ cm}^{-1}$ ). The maximum resolution is  $0.03\text{ cm}^{-1}$ . The optical system of the IFS 113V is divided into four modules as shown in Fig. 2-6: source, interferometer, sample, and detector. The radiation from the source is directed into the interferometer chamber, where it is transmitted and reflected by the beamsplitter, then the recombined light travels to one of the two sample chambers and finally reaches the selected detector. The optical conditions at the entrance and the exit of each module are identical and the sample compartments can be vacuum isolated from the other modules. Rotatable mirrors are used for beam switching.

There are some important features that make this a popular spectrometer. They are summarized as follows:

1. Focused Beam

The interferometer is of a modified Michelson type in which the infrared beam is focused at the beamsplitter so that the beamsplitter can be of a small size. As a result, the "drum head" effect, which refers to the diffusion of the IR beam and resulting spectral noise due to the slight vibration of a big beamsplitter, is decreased dramatically. Moreover, it is easier to produce small beamsplitters and consequently, the quality of the beamsplitter is improved. Since the beamsplitter is small, six of them can be mounted in a rotatable automatic changer.

2. Low Angle of Incidence on the Beamsplitter

The angle of incidence of the IR beam on the beamsplitter is 14 degrees. This low angle compared with other interferometers leads to a higher light throughput and minimum polarization effects.



### 3. Double-sided Moving Interferometer Mirror

The moving mirror is supported on a dual gas bearing which uses dry nitrogen and driven by a linear induction motor. Both sides of the moving mirror are used. Therefore, for a given optical path difference, the mechanical movement of the mirror is just half of that in a conventional Michelson interferometer. This results in greater spectrometer stability and the capability of performing high resolution work.

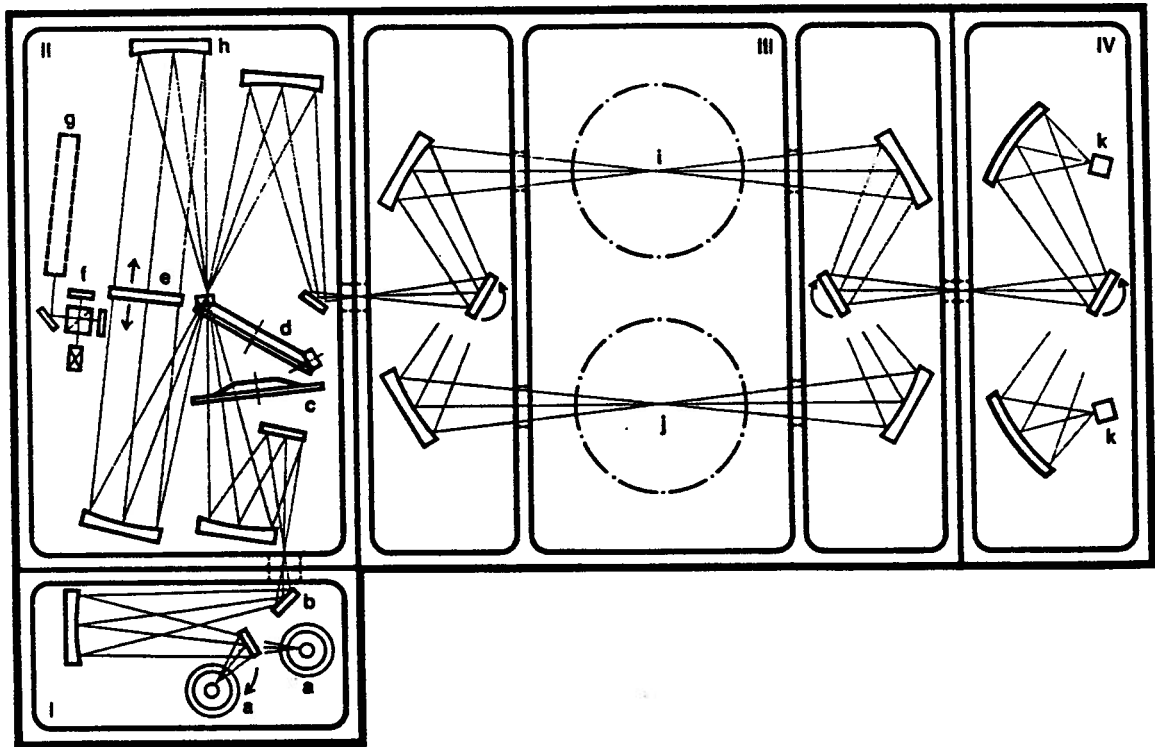


Fig. 2-6: Optical system of the Bruker IFS 113V. (I) Source chamber: a—near-, mid- or far-IR sources. b—automatic aperture. (II) Interferogram chamber: c—optical filter. d—beamsplitter. e—two-sided movable mirror. f—control interferometer. g—reference laser. h—remote control alignment mirror. (III) Sample chamber: i—sample focus. j—reference focus. (IV) Detector chamber: k—Near-, mid- or far-IR detectors.

#### 4. Vacuum Operation

Working under vacuum has several advantages: reducing atmospheric absorptions; higher throughput; less consumables; and maximum stability. The optical bench of the IFS 113V consists of several compartments. Thus the sample area can be vacuum isolated and purged, or a compartment can be replaced by a user-designed one for special experiments.

#### 5. Total Automation

The IFS 113V offers computer controlled switching of up to three sources, four apertures, four optical filters, six beamsplitters, two sample chambers, six detectors and numerous external experimental setups. The ability to change spectral range and experimental settings without opening the optical bench, i.e. without breaking the vacuum, preserves the stable environment required for reproduceable measurements.

#### 6. Rapid-Scan Technique

A rapid-scan technique is used for data collecting, with the steps of the moving mirror determined by the interference fringes of the He-Ne laser reference interferometer. White light is used in addition to determine the mirror position corresponding to zero path difference. The scan speed can be adjusted over a wide range to meet the requirements of different detectors. For a monochromatic source of wavenumber  $\nu$ , the moving mirror with a velocity of  $v$  will result in an alternating electronic signal with frequency  $f$  at the detector. The modulation frequency  $f$  imposed by the moving mirror is given by:

$$f = 4\nu v \quad (2.43).$$

Since this frequency is unique for each wavenumber, we can handle it electrically to filter out radiation outside our range of interest [28]. Thus, low-

pass and high-pass filters are used to determine the electronic cutoff settings for signal processing and we no longer need to rely on optical filters to avoid "false energies" or "aliasing". Other advantages of the rapid-scan technique include: the improved signal to noise ratio since averaging many short scans can achieve a better signal to noise ratio than taking one long scan; discarding "bad" runs which have their zero path difference peaks displaced more than a preset amount; and reduced  $1/f$  noise which is the largest noise source from the He cooled bolometer.

Measurements in different spectral regions require different choice of sources, filters, beamsplitters and detectors. A brief introduction on these important components will be given in the following sections.

### **2.2.2 Sources**

In general, wide-band sources of radiation in the infrared region are "hot body" radiation, whose intensity falls off rapidly in the far-infrared as the wavelength gets longer. The energy of distribution is given by Plank's equation [29].

In the Bruker IFS 113V spectrometer, three types of sources are provided for different spectral ranges. In the far-infrared region, the mercury lamp is used for the wavenumber from 10 to  $700\text{ cm}^{-1}$ . This lamp has the advantage [32], as compared with other hot body sources, that it radiates a greater proportion of its total energy at longer wavelength than shorter wavelength. For the mid-infrared region, a globar source is used between 100 and  $6,000\text{ cm}^{-1}$ . In the near-infrared region, a tungsten source is good for the spectral range of 1,850 to  $15,000\text{ cm}^{-1}$ . All these sources are water cooled.

### 2.2.3. Beamsplitters

The beamsplitter is a crucial part of the interferometer. It transmits and reflects the incident radiation with the ideal reflectance and transmittance of 50%. The beamsplitters can be made of self-supporting dielectric sheets or made of films on a substrate. Generally speaking, in the far-infrared region below  $400\text{ cm}^{-1}$  [26], self-supporting Mylar or polyethylene beamsplitters are usually used. From about  $400$  to  $3,800\text{ cm}^{-1}$ , a Ge film on various transparent substrates can be used. From about  $2,000$  to  $16,000\text{ cm}^{-1}$ , iron oxide ( $\text{Fe}_2\text{O}_3$ ) or Si on different substrates are good for beamsplitters.

If the incident radiation beam has an intensity of 1 and the overall reflectance (power reflected) and transmittance (power transmitted) of the beamsplitter are  $R_0$  and  $T_0$  respectively, the usable radiation has the intensity of  $2R_0T_0$  and the intensity returning to the source is  $R_0^2 + T_0^2$ . The relative intensity, which is defined as  $2R_0T_0$  over  $(2R_0T_0)_{\text{ideal}}$ , is usually used to describe the property of beamsplitter [26]. There are two main factors that will affect the relative efficiency: polarization and the multiple reflection within the beamsplitter. Since in the Bruker IFS 113V, the polarization effects have been minimized by the small incident angle on the beamsplitter, the relative efficiency will vary with wavenumber and depends on the film thickness for a given index of refraction.

In the Bruker IFS 113V spectrometer, beamsplitters are made of four types of materials. For the long wavelength region, self-supporting Mylar beamsplitters with different thickness,  $3\text{ }\mu\text{m}$ ,  $6\text{ }\mu\text{m}$ ,  $12\text{ }\mu\text{m}$ , etc. are available. As the wavelength becomes shorter, it is necessary to make the beamsplitters thinner, and thus, supporting transparent substrates are needed. For the mid-infrared region from

400 to 4000  $\text{cm}^{-1}$ , the useful beamsplitter is Ge film, whose index of refraction is about 4, on a KBr substrate with the index of refraction of about 1.6. The effective range for the Ge film on  $\text{CaF}_2$  beamsplitter is from 2500 to 10,000  $\text{cm}^{-1}$  [26], so it is used for near-infrared measurements with the wavenumber of interest between 2000 and 9000  $\text{cm}^{-1}$ . For wavenumber beyond 9000  $\text{cm}^{-1}$ , a quartz substrate with a Si film can be used. This type of beamsplitter is efficient from 5000 to 20,000  $\text{cm}^{-1}$ .

#### **2.2.4. Detectors**

The function of detectors is to convert the infrared radiation into an electronic signal. Basically, there are two types of detectors: thermal detectors and photo detectors. Thermal detectors measure a change in electronic properties caused by a change in temperature due to the absorbed radiation, while photo detectors measure the change in electronic properties caused by excess electron-hole pairs, which are produced by the absorbed radiation.

Noise always exists in the detectors. The main noise sources are [30]: Johnson noise, which is the limiting noise in all conductors;  $1/f$  noise, which is present in all detectors containing semiconductor elements; noise due to fluctuations in the generation and recombination of charge carriers, and due to the random arrival of photons from the background; temperature noise produced by fluctuations in the temperature of the surroundings and amplifier current and voltage noise.

There are four detectors installed in the Bruker IFS 113V spectrometer: DTGS, MCT, InSb and Si diode, and a He-cooled bolometer is available too. These detectors are now described below.

Deuterated-triglycerine-sulfate (DTGS) pyroelectrical detectors are wide-band thermal detectors. They are exceptionally sensitive, fast, dependable, and have practically indefinite life. The DTGS detectors in the Bruker IFS 113V operate at room temperature ( $\sim 300\text{K}$ ). If a KBr window is used, the useful range of the detector is  $400\text{--}7000\text{ cm}^{-1}$ , and the main application is in mid-infrared. If a poly-ethylene window is used, the useful range will be  $10\text{--}600\text{ cm}^{-1}$ , and the primary application will be in the far-infrared.

Mercury-cadmium-telluride (MCT,  $\text{Hg}_{1-x}\text{Cd}_x\text{Te}$ ) detectors are photo detectors and can operate in either photoconductive or photovoltaic mode. This detector has a fast response and the spectral ranges of response peaks depend on the alloy composition. In the Bruker 113V, this detector works in a photoconductive mode at an operating temperature of  $77\text{K}$ , and has the useful range of  $400\text{--}5000\text{ cm}^{-1}$  with the KRS-5 window. Thus, it is always used for mid-infrared measurements.

The InSb detector is a high-performance photo detector working on the photovoltaic mode [31]. The detector is actually a PN junction. The photovoltaic process involves measuring an external voltage produced by the infrared photons collecting at the PN junction. The operating temperature is  $77\text{K}$ , and the effective range of this detector with a Sapphire window is in the near-infrared, from  $1850$  to  $10,000\text{ cm}^{-1}$ .

The Si diode is a highly sensitive detector in the near-infrared region beyond  $9000\text{ cm}^{-1}$ , working on the photovoltaic mode. The operating temperature is room temperature ( $300\text{K}$ ).

In addition, a He-cooled bolometer may be substituted for the DTGS detector if high sensitivity is desired in the far-infrared region.

## ***Chaper 3***

### **MEASUREMENTS**

#### **3.1 Reflectance Measurement**

##### **3.1.1 Sample Chamber Arrangement**

The front sample compartment in the Bruker IFS 113V was used for the reflectance measurement, as shown in Fig. 3-1, which is viewed from the top [33]. Infrared radiation from the interferometer chamber is focused on an adjustable rectangular aperture F, which is used to restrict the size of the focused beam. The light through the aperture will focus again on the plane of the sample A and reference B with an incident angle of about 15 degrees. The sample holder can be moved from the outside in the horizontal direction M. Thus, we can put the reference or the sample into the beam alternatively. The vertical position of the image can be adjusted by the 1st toroidal mirror H1. The reflected radiation from the sample is collected by the 2nd toroidal mirror H2 and directed to the detector. The chopper I can be moved into the beam by the external rod J when the second toroidal mirror is to be aligned for maximum signal using a digital voltmeter.

##### **3.1.2 Measurement Procedure**

In all of these reflectance measurements, an aluminum mirror was used as the reference.

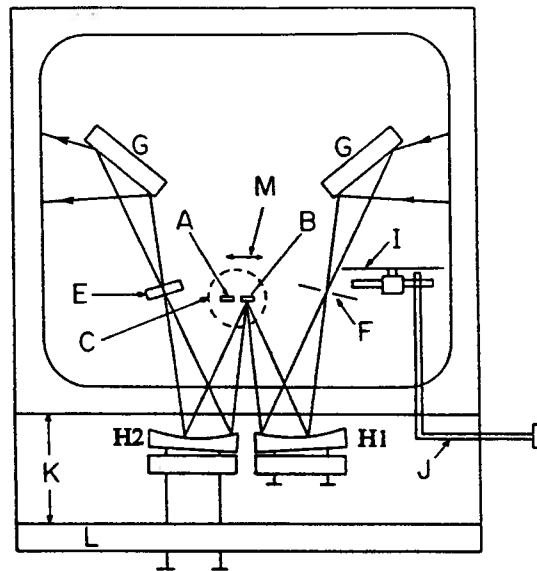


Fig. 3-1: Optical arrangement in the front sample chamber of the Bruker IFS 113V. A, B—mirror and sample. C—sample holder. E—rotateable polarizer. F—adjustable rectangular aperture. G—plane mirrors. H1, H2—toroidal mirrors. I—chopper with motor. J—external rod to move chopper into beam. K—extension to sample chamber. L—plexiglas lid. M—illustration of translational degree of freedom.

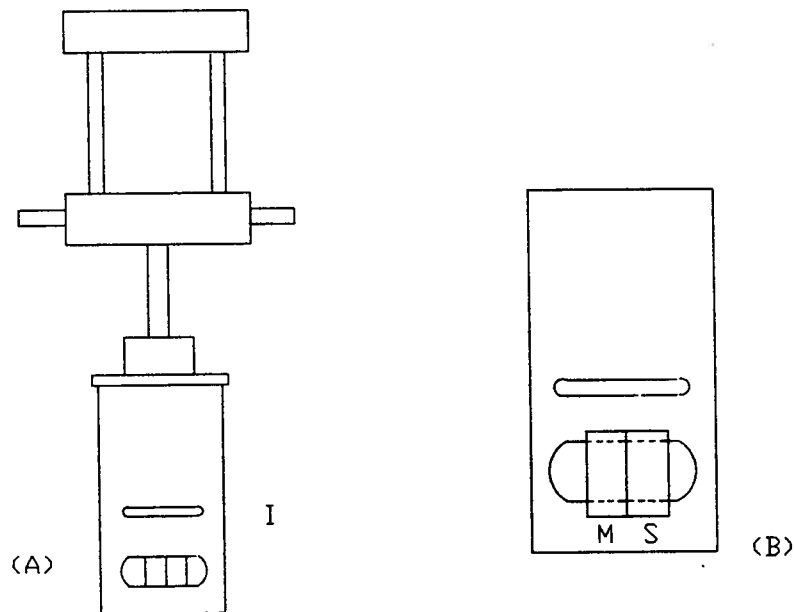


Fig. 3-2: Sample holder for reflectance measurements: (A) front view. (B) back of part I of the sample holder. M: reference mirror. S: sample.



Before starting the measurements, it is important to make sure that the mirror and the sample are clean, especially free of grease. This was achieved by cleaning the sample in an ultrasonic cleaner: the sample was first immersed in a beaker of acetone, then trichloroethylene, followed by methanol, finally, it was rinsed in de-ionized water and blown dry with N<sub>2</sub> gas.

The cleaned mirror and samples were mounted on a sample holder as shown in Fig. 3-2. Grease was used to stick the mirror and the samples on the holding surface instead of copper clips at the back of the mirror and samples in order to avoid any reflections from the clips. Moreover, a piece of black felt paper was put behind the mirror and samples to absorb the transmitted radiation and prevent the transmitted radiation from being reflected by other components in the sample chamber.

For measurements in different spectral regions, the optical settings should be chosen to get the optimum results. Table 3-1 shows the optical parameters used in different regions:

Table 3-1: Optical Parameters in the Bruker 113V

| Optic Parameters | NIR                        | MIR                       | FIR                       |
|------------------|----------------------------|---------------------------|---------------------------|
| Source           | Tungsten                   | Globar                    | Mercury Lamp              |
| Beamsplitter     | CaF <sub>2</sub>           | Ge/KBr                    | Mylar 3.5 $\mu$ m         |
| Optical Filter   | Open                       | Open                      | Blue                      |
| Aperture         | 1.25 mm                    | 5.0 mm                    | 10.0 mm                   |
| Detector         | InSb                       | MCT                       | DTGS                      |
| Spectral Range   | 2000-9000 cm <sup>-1</sup> | 500-5000 cm <sup>-1</sup> | 100-1000 cm <sup>-1</sup> |
| Scanner Velocity | 0.333 cm/s                 | 0.333 cm/s                | 0.099 cm/s                |

Before each measurement, the appropriate optics were first selected, then the tungsten source, which emits visible radiation, was used to see the spot on the rectangular aperture and thus adjust the position of the aperture so that a focused image could be formed at the plane of the sample. It was found that the position of the beam focus on the aperture depends on the beamsplitter used. Furthermore, the size of the aperture restricts the size of the focused beam, so it was also adjusted to suit the sample and to get optimum results. It has been found that the smaller the size of the focused beam, the closer the reflectance of GaAs to the literature value, due to the fact that all of the detectors have fairly small elements. However, the small size of the focused beam results in a low energy throughput and a large noise level in the spectrum. Thus one should be very careful to set the size of the aperture. In the near-infrared and mid-infrared measurements done here, the aperture size was set to about  $1 \times 1 \text{ mm}^2$ .

Evacuating the system is the next step after putting the mirror and samples into the sample chamber and setting the proper optics. Vacuum is indispensable to reduce atmospheric absorption and gain higher throughput as well as the maximum thermal stability. The waiting time of approximately 0.5 to 2 hours before starting the measurement was long enough to obtain stable signals. Since the reflectance chamber is designed such that the movement of the sample holder and the alignment of optics can be done externally while the spectrometer is under vacuum, the stability is not a big problem.

Before taking measurements and applying the Fourier-transformation, the alignment in the sample chamber was adjusted to obtain the maximum signal on the detector. This was done by rotating the sample holder about the vertical axis and adjusting the second toroid mirror H2. An easier method than to maximize the

interferogram peak is to maximize the a.c. output of the detector produced by the chopper which can be brought into the beam to produce an a.c. signal. Since the reference mirror and samples are held on the flat sample holder with grease, they may not be in the same vertical plane even though the holding surface is very smooth. Therefore, we maximized the signal from the mirror before applying the background measurement, and also maximized the sample signal before the sample measurement.

For each background and sample measurement, several hundreds of scans were performed and averaged to increase the signal to noise ratio. The scanner velocity listed before was chosen according to the response time of the detector. Typically, it takes about 4 minutes for a 256-scan measurement.

Due to the imperfect surface of the aluminum mirror, the reflectance measured was always a little bit higher than the ideal one, which could be seen from the GaAs measurement. To solve this problem, a piece of GaAs whose reflectance is known was measured along with the other samples, then the reflectance of the samples were calibrated by the GaAs.

## **3.2 Transmittance Measurements**

### **3.2.1 Sample Chamber Arrangement**

Transmittance measurements were performed in the back channel of the Bruker IFS 113V. The settings in the sample chamber are relatively simple as shown in Fig. 3-3. An adjustable iris aperture is positioned at about the focus of the beam from the interferometer chamber. The sample stands on a sample holder (Fig. 3-4) which is put behind the aperture without touching it. The sample

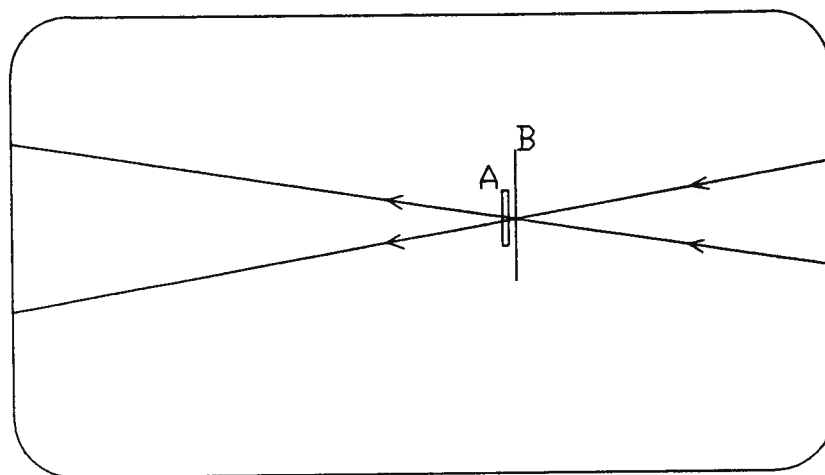


Fig. 3-3: Back channel optical arrangement. (A): Sample (B): Iris aperture

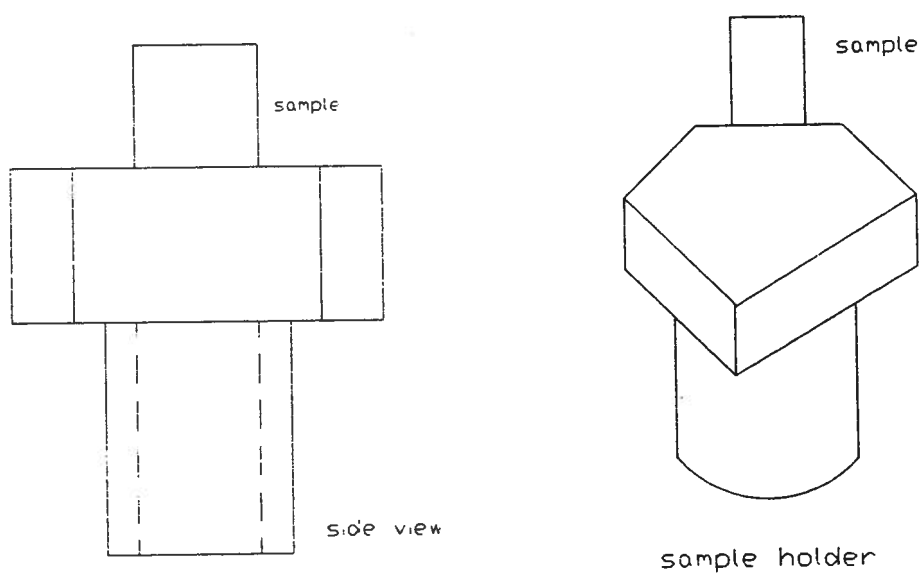


Fig. 3-4: Sample holder for transmittance measurements.

holder can also be used in the brass cryostat for low temperature measurements. The radiation which transmits through the sample will travel to the detector chamber.

### **3.2.2 Measurement Procedure**

Similar to the reflectance measurements, after setting the proper optics in the interferometer chamber, the tungsten source was first used to see the spot on the iris aperture. The aperture could be moved so that it was at the focus of the beam. The size of the aperture could be adjusted to restrict the focused beam on the sample since the sample was placed right behind it. One reason for placing the sample very close to the aperture is to obtain a well focused image, and the other reason is that if the sample is too far away from the aperture, the spread spot on the sample may exceed the dimensions of the sample and some radiation might leak around the edge of the sample to reach the detector. For the same reason introduced in the reflectance measurements, the size of the focused beam has been found to affect the transmittance in the same way as the reflectance. So, the aperture size should be carefully chosen. Because the GaAs sample used for calibration was very narrow, the aperture was set very small, with a diameter about of 1mm.

The reference spectrum was taken just before putting the sample into the chamber, i.e., only with the aperture in the sample chamber. Since a transmittance module which would allow the sample holder to be rotated externally has not yet been constructed, the chamber had to be vented to put in the sample. To avoid changing the background which has been taken before the sample measurement, the sample was put in carefully without touching the

aperture and as close to it as possible. After the sample measurement, the background was taken again to make sure that it had not changed.

After evacuating the system, it was necessary to wait for the system to become stable before taking the measurements. The waiting-period was at least 15 minutes.

Several hundred scans were taken for each measurement just as in the reflectance measurements. The settings of the parameters were the same as those in the reflectance measurement in a specific spectral region, except that the back channel was chosen.

### **3.3 Sample Preparation**

The diamond-like carbon thin film samples tested here were grown by magnetron sputtering method by Glenn Clarke in Dr. Parsons's lab, as part of his course for Ph.D degree. Magnetron sputtering, which is a sputtering technique under the application of a magnetic field parallel to the target surface [11], has the advantages of surface smoothness, the ability to control film uniformity and thickness, and the ability to deposit over a large area.

In Glenn Clarke's M.A.Sc thesis [11], this deposition process has been described: During the magnetron sputtering process, the material of interest for deposition, called the target, is bombarded by energetic particles (ions) to eject target atoms, a number of which will deposit onto the substrate. The system is working in a vacuum chamber which is initially pumped down to a pressure of  $\sim 10^{-6}$  Torr [11], then an inert argon gas is introduced to raise the pressure. Moreover, a reactive gas such as nitrogen or oxygen is sometimes also added to generate a dielectric film. After the desired gas pressure is reached, a negative

potential is applied to the target to create a plasma discharge, while the chamber and part of the target assembly are usually grounded. Thus, the main deposition parameters are: deposition pressure, which is the total gas pressure in the chamber including argon and other gases; partial pressure of a particular gas; target voltage; target current; and the substrate voltage. The structure and properties of the films are greatly dependent on these preparation parameters.

Seven samples were studied here. Their deposition parameters are listed in Table 3-2:

Table 3-2: Deposition parameters for the samples tested

| sample | deposition pressure (Pa) | H <sub>2</sub> partial pressure (Pa) | O <sub>2</sub> partial pressure (Pa) | target voltage (V) | target current (mA) | substrate voltage (V) |
|--------|--------------------------|--------------------------------------|--------------------------------------|--------------------|---------------------|-----------------------|
| acap18 | 8                        | 0                                    | 0                                    | ~530               | ~190                | ~7                    |
| acju11 | 8                        | 0                                    | 0                                    | 532                | 190                 | 7                     |
| acju13 | 4                        | 0                                    | 0                                    | 555                | 181                 | 17                    |
| acju17 | 1                        | 0                                    | 0                                    | 618                | 163                 | 25                    |
| acjl27 | 1                        | 0                                    | 0.1                                  | 623                | 161                 | 25                    |
| acau07 | 1                        | 0.1                                  | 0                                    | 557                | 181                 | 24                    |

## **Chapter 4**

# **REFLECTION, TRANSMISSION AND ABSORPTION IN AMORPHOUS THIN FILMS**

### **4.1 Matrix Method for Reflectance and Transmittance Calculation**

When an electromagnetic wave is incident on a solid media, it can be reflected, transmitted, and absorbed. The optical properties of this solid can be obtained by measuring the intensity of the reflected and transmitted light. To achieve this, one of the most commonly used methods is the matrix method.

#### **4.1.1 The Simple Boundary**

An incident plane electromagnetic wave can be expressed as:

$$\mathbf{E}_i(\mathbf{r}, t) = \mathbf{E}_i \exp[i(\mathbf{k}_i \cdot \mathbf{r} - \omega t)] \quad (4.1)$$

Assume that the media are isotropic and homogeneous, the optical properties of the media can be described by the complex index of refraction:

$$N = n + ik \quad (4.2)$$

where  $n$  is the real refractive index, or often simply refractive index, and  $k$  is known as the extinction coefficient.  $k$  is a measure of the absorption in the media.

It is related to the absorption coefficient  $\alpha$  by:

$$\alpha = 4\pi k / \lambda = 4\pi k \nu \quad (4.3)$$

where  $\nu$  ( $=1/\lambda$ ) is the wavenumber in  $\text{cm}^{-1}$ .

Considering the simplest case where an plane electromagnetic wave is incident on a single boundary between two media, denoted by suffix 0 for the incident medium and suffix 1 for the exit medium, for normal incidence, the



Fresnel amplitude reflection and transmission coefficients are given by  $\rho$  and  $\tau$  respectively [34]:

$$\rho = \frac{E_r}{E_i} = \frac{N_0 - N_1}{N_0 + N_1} \quad (4.4)$$

$$\tau = \frac{E_t}{E_i} = \frac{2N_0}{N_0 + N_1} \quad (4.5)$$

where  $E_i$ ,  $E_r$  and  $E_t$  are the electric field amplitudes of the incident, reflected and transmitted waves respectively, and  $N_0, N_1$  are the complex refractive indices for medium 0 and 1 respectively.

If  $I_i$ ,  $I_r$  and  $I_t$  are the intensities of the incident, reflected and transmitted light, then the reflectance  $R$  and transmittance  $T$  are as follows for a non-absorbing incident media [34]:

$$R = \frac{I_r}{I_i} = \rho\rho^* = \left(\frac{N_0 - N_1}{N_0 + N_1}\right)\left(\frac{N_0 - N_1}{N_0 + N_1}\right)^* \quad (4.6)$$

$$T = \frac{I_t}{I_i} = \frac{n_1}{n_0} \tau\tau^* = \frac{4n_0n_1}{(N_0 + N_1)(N_0 + N_1)^*} \quad (4.7)$$

where  $N_0$  is a real number.

#### 4.1.2 Assembly of Thin Films

The presence of two or more interfaces will produce successive reflections and transmissions. The summation of these beams will determine the properties of this assembly of thin films.

As shown in Fig. 4-1, a plane wave  $E_i$  with electric field amplitude  $E_i$  is incident normally on a pile of  $L$  parallel faced layers each of which is isotropic and homogeneous [35], then a reflected wave  $E_r$  and transmitted wave  $E_t$  exist.

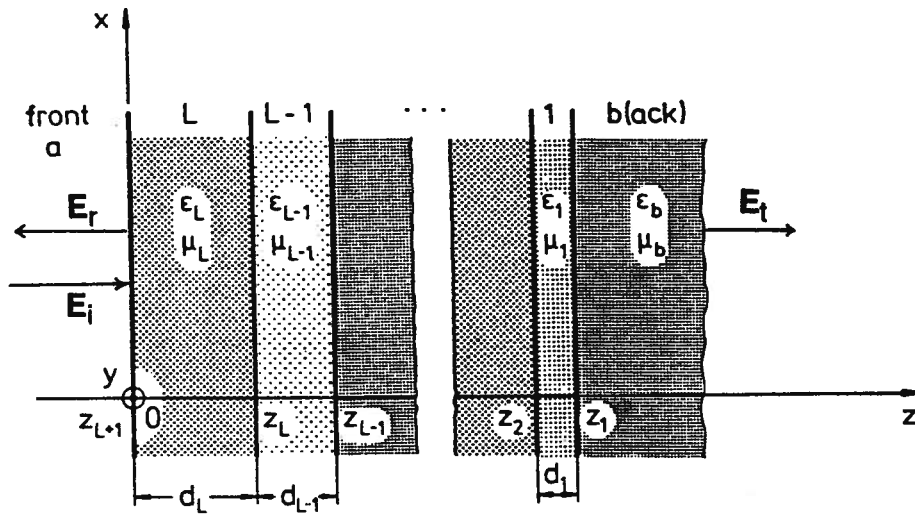


Fig. 4-1: The pile of layers and the coordinates used throughout the text

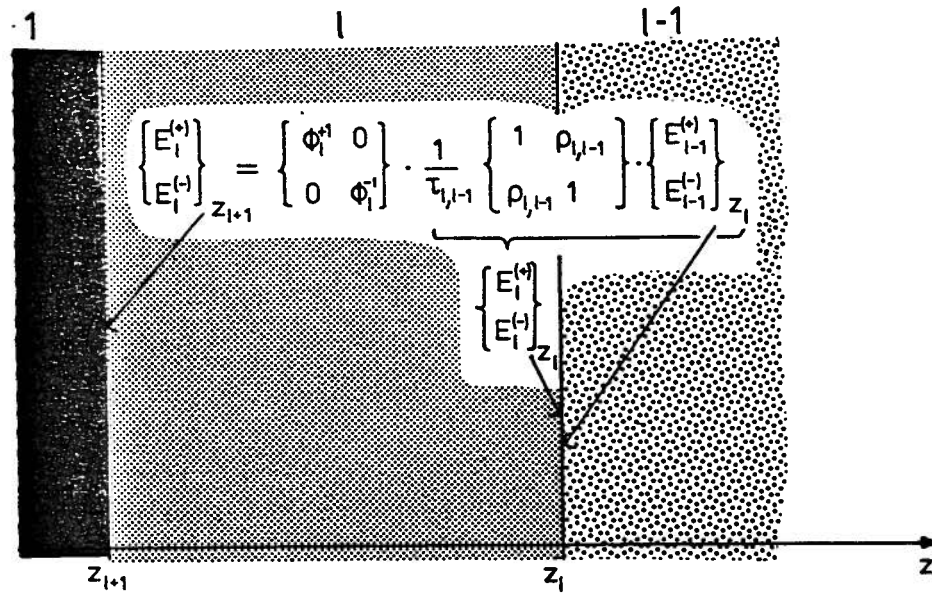


Fig. 4-2: The transformation of the waves ( $E^+$ ,  $E^-$ ) across the interface between layer  $l-1$  and  $l$  and through the inside of layer  $l$

Considering the tangential components of the fields, the field in a layer  $l$  can be described as the superposition of a positive-going wave and a negative-going wave. In the case of s-polarized wave [35],

$$\begin{aligned} E_l(x, z, t) &= [E_l^+(z) + E_l^-(z)] \cdot \exp[i(\frac{\omega}{c} x \sin \alpha - \omega t)] \\ &= [E_l^+ \exp(i \frac{\omega}{c} N_l z) + E_l^- \exp(-i \frac{\omega}{c} N_l z)] \cdot \exp[i(\frac{\omega}{c} x \sin \alpha - \omega t)] \end{aligned} \quad (4.8)$$

where  $+$  denotes the waves in the incident direction,  $-$  denotes the waves in the opposite direction and  $\alpha$  is the angle of incidence. The transformations of waves ( $E^+, E^-$ ) across layer  $l$  is illustrated in Fig. 4-2 :

1. the transformation of the fields  $E^+$  and  $E^-$  across the interface between two layers  $l$  and  $l-1$ :

$$\begin{pmatrix} E_l^+ \\ E_l^- \end{pmatrix}_{z_l} = \frac{1}{\tau_{l,l-1}} \cdot \begin{pmatrix} 1 & \rho_{l,l-1} \\ \rho_{l,l-1} & 1 \end{pmatrix} \cdot \begin{pmatrix} E_{l-1}^+ \\ E_{l-1}^- \end{pmatrix}_{z_{l-1}} \quad (4.9)$$

where  $\rho_{l,l-1}$  and  $\tau_{l,l-1}$  are the Fresnel's reflection and transmission coefficients:

$$\rho_{l,l-1} = \frac{N_l - N_{l-1}}{N_l + N_{l-1}}, \quad \tau_{l,l-1} = \frac{2N_l}{N_l + N_{l-1}} \quad (4.10)$$

and  $N$  is the complex refractive index:  $N = n + ik$

2. the transformation through the layer:

$$\begin{pmatrix} E_l^+ \\ E_l^- \end{pmatrix}_{z_{l+1}} = \begin{pmatrix} \phi_l^{-1} & 0 \\ 0 & \phi_l \end{pmatrix} \begin{pmatrix} E_l^+ \\ E_l^- \end{pmatrix}_{z_l} \quad (4.11)$$

where  $\phi_l = \exp(i \frac{\omega}{c} N_l d_l)$  and  $d_l$  is the thickness of layer  $l$ .

Thus,

$$\begin{pmatrix} E_i^+ \\ E_i^- \end{pmatrix}_{z_{i+1}} = \begin{pmatrix} \phi_i^{-1} & 0 \\ 0 & \phi_i \end{pmatrix} \cdot \frac{1}{\tau_{i,i-1}} \cdot \begin{pmatrix} 1 & \rho_{i,i-1} \\ \rho_{i,i-1} & 1 \end{pmatrix} \cdot \begin{pmatrix} E_{i-1}^+ \\ E_{i-1}^- \end{pmatrix}_{z_i} \quad (4.12)$$

For a pile of thin films (Fig. 4-1), the above two transfer operations have to be applied successively. Consequently, the complete transfer from medium b to medium a which is assumed vacuum here can be expressed as:

$$\begin{pmatrix} E_i \\ E_r \end{pmatrix}_{z=z_{L+1}=0} = \begin{pmatrix} T_{11} & T_{12} \\ T_{21} & T_{22} \end{pmatrix} \cdot \begin{pmatrix} E_i \\ 0 \end{pmatrix}_{z=z_1} \quad (4.13)$$

where the matrix **T** is the product of *L* matrices of type (4.12) followed by the transformation through the surface of this pile at  $z_{L+1}=0$ .

With the definition of the reflection and transmission coefficients :

$$r_{ab} = \frac{E_r(z=0)}{E_i(z=0)}, \quad t_{ab} = \frac{E_t(z=z_1)}{E_i(z=0)} \quad (4.14)$$

Eq. (4.13) can be rewritten as

$$\begin{pmatrix} 1 \\ r_{ab} \end{pmatrix} = \begin{pmatrix} T_{11} & T_{12} \\ T_{21} & T_{22} \end{pmatrix} \cdot \begin{pmatrix} t_{ab} \\ 0 \end{pmatrix}. \quad (4.15)$$

Then  $r_{ab}$  and  $t_{ab}$  can be obtained

$$r_{ab} = T_{21} / T_{11}, \quad t_{ab} = 1 / T_{11}. \quad (4.16)$$

If considering the case that the light is incident on the back b and emerges at the front a, we can have [35]:

$$\begin{pmatrix} 0 \\ t_{ba} \end{pmatrix} = \begin{pmatrix} T_{11} & T_{12} \\ T_{21} & T_{22} \end{pmatrix} \cdot \begin{pmatrix} r_{ba} \\ 1 \end{pmatrix} \quad (4.17)$$

$$r_{ba} = -T_{12} / T_{11}, \quad t_{ba} = (T_{11}T_{22} - T_{12}T_{21}) / T_{11} \quad (4.18)$$

### 4.1.3 Coherent Films and Incoherent Substrate

The definitions of the thin and thick films are based on the interference phenomena [34]: The film is considered thin when the interference effects can be detected in the reflectance and transmittance spectra, that is, when the optical path difference between the two beams is less than the coherence length of the light, and the film is thick when the path difference is greater than the coherence length. Usually, the films on the substrate can be treated as thin films and the substrate supporting the films can be treated as thick.

If there is a system consisting of piles of thin films and substrate, such as :medium a/pile 1/substrate/pile 2/medium b [35], we can apply the procedures in the above section and obtain the reflection and transmission coefficients from medium a (front) to medium b (back):

$$r_{ab} = r_{as} + \frac{t_{as}t_{sa}r_{sb}\phi_s^2}{1 - r_{sa}r_{sb}\phi_s^2} \quad t_{ab} = \frac{t_{as}\phi_s t_{ab}}{1 - r_{sa}r_{sb}\phi_s^2} \quad (4.19)$$

In the case of thick substrate, the waves reflected successively at the front and back surfaces of the substrate add incoherently instead of coherently. Thus, taking the absolute values of the complex coefficients  $t$ ,  $r$  and  $\phi$ , coherence can be turned off between the neighboring films. Therefore, for normal incidence and when medium a is the same as medium b, the reflectance and transmittance of this system with an incoherent substrate can be given by:

$$R_{incoh} = |r_{as}|^2 + \frac{|t_{as}t_{sa}r_{sb}|^2 \exp(-4\frac{\omega}{c}k_s d_s)}{1 - |r_{sa}r_{sb}|^2 \exp(-4\frac{\omega}{c}k_s d_s)} \quad (4.20)$$

$$T_{incoh} = \frac{|t_{as}t_{sb}|^2 \exp(-2\frac{\omega}{c}k_s d_s)}{1 - |r_{sa}r_{sb}|^2 \exp(-4\frac{\omega}{c}k_s d_s)} \quad (4.21)$$

In the case of our samples, which is a carbon thin film layer on a GaAs substrate, there are three boundary surfaces as shown in Fig. 4-3. Since the substrate is incoherent and non-absorbing, i.e.,  $k_s \approx 0$ , at normal incidence, Eqs. (4.20) and (4.21) can be simplified as:

$$R = |r_{as}|^2 + \frac{|t_{as}t_{sa}r_{sb}|^2}{1 - |r_{sa}r_{sb}|^2} \quad (4.22)$$

$$T = \frac{|t_{as}t_{sb}|^2}{1 - |r_{sa}r_{sb}|^2} \quad (4.23)$$

where  $r_{as}$ ,  $t_{as}$ ,  $r_{sa}$  and  $t_{sa}$  are derived from Eqs. (4.12) to (4.18) and can be easily calculated by computer program. Since there is just one boundary between substrate and medium b,  $r_{sb}$  and  $t_{sb}$  are just Fresnel's reflection and transmission coefficients through this boundary.

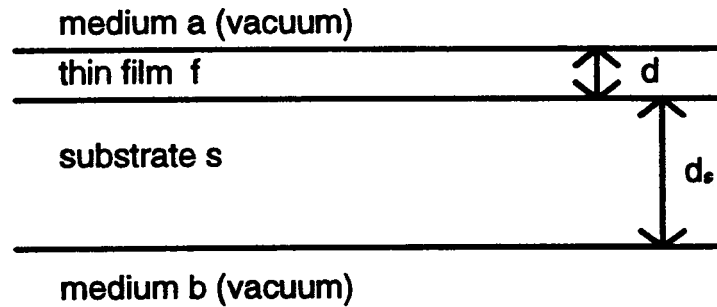


Fig. 4-3: Layers in our samples

Eqs. (4.22) and (4.23) were used for our samples.

## **4.2 Optical Model for Amorphous Solids in the Interband Region**

From the last section, we can see that when an electromagnetic wave interacts with a solid medium, the reflectance and transmittance are determined by the complex index of refraction  $N=n+ik$ , where  $n$  (refractive index) and  $k$  (extinction coefficient) are termed as optical constants. However,  $n$  and  $k$  are not constant over the optical region. They depend on the photon energy  $E = \hbar\omega$ , and exhibit structure in the interband region where bound electron transitions are dominant. Thus, the optical constants are presented as  $n(E)$ ,  $k(E)$ . A.R.Forouhi and I.Bloomer gave a model for  $n(E)$  and  $k(E)$  in reference [36], which will be described below.

### **4.2.1 Derivation of $k(E)$**

Based on the quantum mechanical theory of absorption, an expression for the extinction coefficient  $k$  can be deduced. In the fundamental optical region, interband transition of bound electrons are mainly responsible for optical properties. Using time-dependent perturbation theory, the rate, denoted as  $\Phi(\omega)$ , at which photon energy is absorbed from the incident beam can be derived from the probability that an electron transfers to an excited state. Furthermore, the absorption coefficient  $\alpha$  is proportional to  $\Phi(\omega)$ , and thus, the extinction coefficient can be obtained. This method can be applied to amorphous semiconductors and dielectrics, crystalline semiconductors and dielectrics, as well as metals.

From first order time-dependent perturbation theory, the rate of energy absorbed,  $\Phi(\omega)$ , in the frequency range  $\omega$  to  $\omega+d\omega$ , associated with an electron transition between two arbitrary states  $|a\rangle$  and  $|b\rangle$  where  $E_a > E_b$ , is given by

$$\Phi(\omega) = \frac{4\pi\hbar}{3c} e^2 \omega_0 |\langle b|\mathbf{x}|a\rangle|^2 \left[ \frac{\gamma}{(E_b - E_a - \hbar\omega)^2 + \hbar^2 \gamma^2 / 4} \right] \quad (4.24)$$

where  $e$  stands for electron charge,  $\mathbf{x}$  is the electron position vector,  $\langle b|\mathbf{x}|a\rangle$  is the dipole matrix element between initial and final states,  $I_0$  is the incident photon energy, and  $\gamma$  is the reciprocal of the finite lifetime of the excited state.  $\Phi(\omega)$  reaches the maximum when  $\hbar\omega = E_b - E_a$ .

Under the assumption that there is only one peak in the optical constants of amorphous semiconductors and dielectrics, taking  $|a\rangle$  and  $|b\rangle$  to be bonding state  $|\sigma\rangle$  and antibonding state  $|\sigma^*\rangle$  with associated energies  $E_\sigma$  and  $E_{\sigma^*}$ ,  $\Phi(\omega)$  for amorphous solids is

$$\Phi(\omega) = \frac{4\pi\hbar}{3c} e^2 \omega_0 |\langle \sigma^*|\mathbf{x}|\sigma\rangle|^2 \left[ \frac{\gamma}{(E_{\sigma^*} - E_\sigma - \hbar\omega)^2 + \hbar^2 \gamma^2 / 4} \right] \quad (4.25)$$

Derived from Eq.(4.3), the extinction coefficient  $k$  is directly related to the absorption coefficient  $\alpha(\omega)$ :

$$k(\omega) = \frac{c}{2\omega} \alpha(\omega) \quad (4.26)$$

$\alpha(\omega)$  is proportional to  $\Phi(\omega)$  and can be expressed as

$$\alpha(\omega) = \Theta \Phi(\omega) / I_0 \quad (4.27)$$

where  $\Theta$  represents the total number of ways that a photon of energy  $\hbar\omega$  can be removed from the incident radiation, per unit volume in an infinitesimal layer of thickness.  $\Theta$  is proportional to the product of the number of occupied electron states in the valence band in the energy range  $dE_v$  and the number of unoccupied electron states in the conduction band. Let  $\eta_v(E_v)$ ,  $\eta_c(E_c)$  stand for



the density of states in the valence band  $E_v$  and the conduction band  $E_c$  respectively, and  $f(E)$  represents Fermi function, thus,

$$\Theta \propto \int \eta_v(E_v) f_v(E_v) \eta_c(E_v + \hbar\omega) [1 - f_c(E_v + \hbar\omega)] dE_v \quad (4.28)$$

In the case of amorphous solids, take the optical band gap as:

$$E_g = E_c^{bottom} - E_v^{top} \quad (4.29)$$

Then  $\Theta$  can be written as

$$\Theta = const(\hbar\omega - E_g)^2 \quad (4.30)$$

where *const* stands for a constant. From Eq.(4.26), (4.27), (4.25), and (4.30),  $k(\omega)$  can be derived for amorphous semiconductors and dielectrics:

$$k(\omega) = const \cdot |\langle \sigma^* | x | \sigma \rangle|^2 \cdot \left[ \frac{\gamma}{(E_{\sigma^*} - E_{\sigma} - \hbar\omega)^2 + \hbar^2 \omega^2 / 4} \right] \cdot (\hbar\omega - E_g)^2 \quad (4.31)$$

More compactly, it can be written as

$$k(E) = \frac{A(E - E_g)^2}{E^2 - BE + C} \quad (4.32)$$

with parameters:  $A = const |\langle \sigma^* | x | \sigma \rangle|^2 \gamma$ ,  $B = 2(E_{\sigma^*} - E_{\sigma})$ ,  $C = (E_{\sigma^*} - E_{\sigma})^2 + \hbar^2 \gamma^2 / 4$ .

#### 4.2.2 Derivation of $n(E)$

The refractive index  $n(E)$  is related to the extinction coefficient  $k(E)$  by the Kramers-Kronig dispersion relations:

$$n(E) - n(\infty) = \frac{1}{\pi} P \int_{-\infty}^{+\infty} \frac{k(E') - k(\infty)}{E' - E} dE' \quad (4.33)$$

where  $n(\infty)$  and  $k(\infty)$  are the infinite limits of  $n(E)$  and  $k(E)$ , and  $P$  is the Cauchy's principle value integral.

By evaluating Eq.(4.33),  $n(E)$  for amorphous semiconductors and dielectrics can be obtained:

$$n(E) = n(\infty) + \frac{B_a E + C_a}{E^2 - B_a E + C_a} \quad (4.34)$$

where

$$B_a = \frac{A}{Q} \left( -\frac{B^2}{2} + E_g B - E_g^2 + C \right) \quad (4.35)$$

$$C_a = \frac{A}{Q} \left[ (E_g^2 + C) \frac{B}{2} - 2E_g C \right] \quad (4.36)$$

$$Q = \frac{1}{2} (4C - B^2)^{1/2} \quad (4.37)$$

$k(E)$ ,  $n(E)$  can be fully and simultaneously determined by the parameters  $A$ ,  $B$ ,  $C$ ,  $E_g$  and  $n(\infty)$ .  $E_g$  is simply the measured energy of which  $k(E)$  has its absolute minimum value.  $n(\infty)$  is approximately equal to but always greater than one. The value of  $B/2$  is approximate equal to the energy at which  $k(E)$  is a maximum. The parameter  $C$  depends on the energy difference between distinguishable states and the transition lifetime. The parameter  $A$  is associated with the square of the dipole matrix element and essentially gives the strength of the peak in  $k(E)$ .

$k(E)$  and  $n(E)$  model is quite useful for determining the film thickness. In the case of our films, the near-infrared reflectance and transmittance features are due to the interband transition, thus this model and matrix method can be used to fit the experimental data so that the film thickness can be obtained as a fitting parameter.

### 4.3 Optical Model for Amorphous Solids in Long Wavelength Region

In the interband optical region, the optical properties mainly depend on the interband transitions of bound electrons. However, as the wavelength of the

incident radiation becomes longer, i.e., the photon energy is away from the band gap, the dominant optical processes in the medium are vibrational excitations. In the semiempirical dispersion model [7] used here for amorphous solids, the strong absorptions in the long wavelength region are mainly due to excited vibrational resonances, and the influence from the interband transition is considered to be an Urbach absorption tail. Therefore, the total absorption in this region will be the superposition of these two effects.

The complex index of refraction is related to the complex dielectric function  $\epsilon(\nu)$  by

$$N = n(\nu) + ik(\nu) = [\epsilon(\nu)]^{1/2} \quad (4.38)$$

and the absorption coefficient can be given by  $\epsilon(\nu)$ :

$$\alpha(\nu) = 4\pi k(\nu) = 4\pi\nu \text{Im}\{[\epsilon(\nu)]^{1/2}\} \quad (4.39)$$

Even though amorphous solids do not have long-range order, their vibrational behavior is very similar to that of the corresponding crystalline forms, except that the selection rules for transitions are relaxed (no  $k$  conservation) and sharp features in the density of vibrational modes are broadened. Thus, similar to the Lorentz oscillator model used for crystalline materials, the dielectric function due to the vibrational resonances in the amorphous solids can be expressed as the superposition of  $N$  Lorentz lines :

$$\epsilon_i(\nu) = A_0 + A_1\nu^2 + \frac{1}{\pi} \sum_{j=1}^N \frac{J_j}{\nu_{0j} - \nu - i\Gamma_j} \quad (4.40)$$

where  $A_0$ ,  $A_1$ ,  $J_j$ ,  $\nu_{0j}$  and  $\Gamma_j$  are constants.  $\nu_0$  is the resonance frequency,  $J$  is the intensity factor and  $2\Gamma$  is the line width. The term  $A_0 + A_1\nu^2$  describes a weak background Sellmeier dispersion [37].

The Urbach tail is presented in the form:

$$\alpha_u(\nu) = \alpha_{u0} \exp(\nu / \nu_{u0}) \quad (4.41)$$

where  $\alpha_{u0}$  and  $\nu_{u0}$  are constants.

Considering Urbach background absorption in the dielectric function,

$$\epsilon(\nu) = \{[\epsilon_r(\nu)]^{1/2} + \frac{j\alpha_u(\nu)}{4\pi\nu}\}^2. \quad (4.42)$$

Finally, from Eqs. (4.39), (4.38), we can have

$$N(\nu) = [\epsilon(\nu)]^{1/2} = [\epsilon_r(\nu)]^{1/2} + j\frac{\alpha_u(\nu)}{4\pi\nu} \quad (4.43)$$

$$n(\nu) = \text{Re}\{[\epsilon_r(\nu)]^{1/2}\} \quad (4.44)$$

$$\alpha(\nu) = 4\pi\nu \text{Im}\{[\epsilon_r(\nu)]^{1/2}\} + \alpha_u(\nu) \quad (4.45)$$

Eq.(4.45) was used to fit the experimentally established absorption coefficient data. More details will be given in the next chapter.

## **Chapter 5**

### **EXPERIMENT RESULTS AND DISCUSSION**

#### **5.1 Experiment Results**

The samples are amorphous diamond-like carbon (DLC) thin films about 1  $\mu\text{m}$  thick on semi-insulating GaAs (SI-GaAs) substrate, named in chronological order: acap18, acju11, acju13, acju17, acjl27, acau07, and acau24. The deposition parameters for these samples have already been described in Chapter 3. Reflectance and transmittance measurements were performed at nearly normal incidence, using the Bruker 113V spectrometer.

##### **5.1.1 Far-infrared Results**

Figure 5-1 shows the far-infrared reflectance spectra of an amorphous carbon thin film on SI-GaAs substrate, from  $100\text{ cm}^{-1}$  to  $700\text{ cm}^{-1}$ , as well as the reflectance of the substrate. The sample was acap18 grown under a deposition pressure of 8 Pa. Figure 5-2 is the transmittance spectra of sample acap18 and SI-GaAs substrate. By comparing the spectra of sample acap18 with those of SI-GaAs, one can see that the spectra of the sample actually show the features of SI-GaAs substrate. This is due to the small absorption of the carbon thin film in this region. Thus, this region is not the one in which we are interested and was not investigated further.

### 5.1.2 Mid-infrared Results

In the mid-infrared (MIR) region, from  $800\text{ cm}^{-1}$  to  $4000\text{ cm}^{-1}$ , the extinction coefficient  $k$  of Si-GaAs is zero except at  $1042\text{ cm}^{-1}$  [38], which is primarily intrinsic due to multiphonon absorption. This means there is little absorption in this region from Si-GaAs. As a result, Si-GaAs is a good substrate for studying the amorphous DLC thin films in this region. The MIR reflectance spectrum of GaAs is shown in Fig. 5-3. However, the multiphonon absorption did not appear in Fig. 5-3 for it might be too weak to see.

The reflectance and transmittance spectra of the investigated samples are shown in Fig. 5-4 (A) to Fig 5-8 (A). The main features of these spectra are the wide interference oscillations characteristic of thin films, with dips indicating absorption from vibrational modes. Fig. 5-4 (B) to Fig. 5-8 (B) are the absorptance spectra, which are calculated from  $A=1-R-T$ , where  $A$ ,  $R$ ,  $T$  are the absorptance, reflectance, and transmittance respectively. The absorption behavior of the film is much clearer in the absorption spectra: Sample acju11, acju13 and acau07 act similarly, showing the optical "window" between  $1900$  to  $2700\text{ cm}^{-1}$ , and strong absorption bands around  $1300\text{ cm}^{-1}$ ,  $1600\text{ cm}^{-1}$ ,  $1700\text{ cm}^{-1}$  and  $2900\text{ cm}^{-1}$ . Sample acju11 and acju13 also have absorption bands at around  $3300$  and  $3500\text{ cm}^{-1}$ . Sample acju17 and acjl27 are quite different from the others. They have very strong absorption increasing with wavenumber after  $1900\text{ cm}^{-1}$ , which may due to the interband absorption. Neither the flat transparent "window" nor the C-H absorption bands from about  $3000$  to  $3500\text{ cm}^{-1}$  have been observed in these two films.

### 5.1.3 Near-infrared Results

Reflectance measurements in the near-infrared (NIR) were performed in order to determine the thickness of the thin film. An optical method to determine the film thickness is better than a mechanical method since it is non-destructive and more accurate. In the NIR region from 4000 to 9000  $\text{cm}^{-1}$ , the absorption mechanism of the amorphous DLC film is the interband transition and no vibrational modes have been observed. Thus, by fitting the experimental value of the reflectance using the optical constants model in the interband region, which has been introduced in Chapter 4, the film thickness can be obtained. In order to reduce the error, a reflectance measurement was also performed for the same film on a glass substrate. As shown in Fig. 5-9, the model fits the experimental data quite well. All of the data fitting in the NIR was performed by Glenn Clarke using his program, and thus he obtained the thicknesses of the films as one of the fitting parameters.

### 5.1.4 Absorption Coefficients and Bonding Configurations

In the MIR region, the absorption is mainly caused by the excitation of vibrational resonances. Therefore, the optical constants model used in the NIR region is not suitable anymore. However, based on the homogeneous film model presented in Fig. 4-3,  $n(\nu)$  and  $k(\nu)$  can be found from experimental values of the transmittance  $T$  and reflectance  $R$  by means of the iteration method. As introduced in Chapter 4,  $R$  and  $T$  can be calculated by the matrix method, i.e., Eqs. (4.22), (4.23), and then  $n(\nu)$  and  $k(\nu)$  may be solved from the equations:

$$\begin{cases} T_{\text{expt}}(\nu) - T_{\text{calc}}(\nu, n, k) = 0 \\ R_{\text{expt}}(\nu) - R_{\text{calc}}(\nu, n, k) = 0 \end{cases}$$

In order to get the solutions of the nonlinear array of equations, the two dimensional Newton-Raphson iteration method was used [39]. Upon knowing  $k$ , the absorption coefficient as a function of wavenumber could be calculated. The results are shown in Fig. 5-10 to 5-14 with dotted lines. This work was also done by Glenn Clarke, using programs written by him.

The optical properties of the film rely on the atomic bonding configuration in the film. In order to get this information, a dispersion model, described in Chapter 4 (Eqs. (4.40) to (4.45)), was used to fit the absorption coefficient data obtained from the experimental reflectance and transmittance values. For sample acju11, acju13, and acau07, an Urbach absorption tail was used as the background absorption, and  $\alpha_0$ ,  $\nu_0$  in Eq. (4.41) were obtained through fitting the MIR absorption coefficient data. Lorentz phonon lines were then successively added. The strong absorption after 2700  $\text{cm}^{-1}$  in sample acju17 and acjl27 seemed to be interband transitions and to follow the Tauc law given by:

$$(\alpha E)^{1/2} = B(E - E_0),$$

where  $E$  is the photon energy, and  $B$  and  $E_0$  are constants. Tauc law therefore was used first and then followed by an Urbach tail to fit the data of these two samples. Lorentz lines below 1900  $\text{cm}^{-1}$  were also added to fit the vibrational modes in that region.

The fitting results are the solid lines in Fig. 5-10 to Fig. 5-14. The fitting parameters used are listed in table 5-1, where  $\nu_0$ ,  $\Gamma$ , and  $J$  in Eq.(4.40) stand for resonance frequency, intensity factor and half line width, respectively.



## 5.2 Discussion

### 5.2.1 Optical Properties and Bonding Configuration

As illustrated in the absorption coefficient spectra, Fig. 5-10 to Fig. 5-14, samples grown under high deposition pressure (acju11 and acju13) and samples grown under low deposition pressure but with considerable hydrogen content (acau07), have similar MIR spectra, while samples prepared under low pressure with or without oxygen incorporation (acjl27 and acjl17) are quite different.

As for sample acju11, acju13 and acau07, the MIR region can be conveniently divided into 3 parts to describe the typical optical properties. The first part is the C-C network and  $\text{CH}_x$  deformation region at  $\nu < 1700 \text{ cm}^{-1}$ . In this region, all of the 3 samples show strong absorption lines at about  $1300 \text{ cm}^{-1}$ ,  $1438 \text{ cm}^{-1}$ ,  $1600 \text{ cm}^{-1}$ , and  $1700 \text{ cm}^{-1}$ . The band at about  $1700 \text{ cm}^{-1}$  is known as C=O stretch in C=O and HC=O while the one at about  $1600 \text{ cm}^{-1}$  is assigned to C=C stretch [20]. The band at around  $1438 \text{ cm}^{-1}$  is possibly due to C-H rock or  $\text{CH}_2$  deformation [20], and the peak at  $1300 \text{ cm}^{-1}$  may be caused by  $\text{sp}^2$ - and  $\text{sp}^3$ -hybridized carbons [22]. Though the  $-\text{CH}_3$  symmetric bending at about  $1375 \text{ cm}^{-1}$  [23] appear in the spectra of acju11 and acju13, it does not show up in that of acau07.

The second region is the low absorption "window" between  $1900$  and  $2700 \text{ cm}^{-1}$ , which is of great interest for potential optical applications. Sample acju11 and acau07 exhibit better qualities than acju13 which shows gradually increasing absorption with wavenumber. The little peak at around  $2100 \text{ cm}^{-1}$  may be associated with nitrogen impurities (C-N bonds).

The third region is the  $\text{CH}_x$  stretching vibration area after  $2700\text{ cm}^{-1}$ . The strong peak at about  $2900\text{ cm}^{-1}$  in all of these 3 samples is the  $\text{sp}^3\text{C-H}$  stretching vibration [22]. Sample acau07 also shows a very weak absorption at about  $3000\text{ cm}^{-1}$ , which might due to C-H stretch in  $=\text{CH}$  [20]. In stead of showing the peak at  $3000\text{ cm}^{-1}$ , acju11 and acju13 show strong absorptions at approximate  $3300\text{ cm}^{-1}$  and  $3500\text{ cm}^{-1}$ . The former peak may be assigned to hydrogen bonded  $\text{sp}^1$  hybridized carbon [23], and the latter is probably caused by O-H stretching modes.

Sample acju17 and acjl27 are much more absorbing. The absorption which increases rapidly with wavenumber after  $1900\text{ cm}^{-1}$  appears due to interband transitions, indicating a small optical band gap in these films. The broad band from  $1000$  to  $1700\text{ cm}^{-1}$  may be caused by overlapping vibrational resonances. From the data fitting, at least the resonances from C=C stretch at about  $1600\text{ cm}^{-1}$ ,  $\text{CH}_2$  deformation at  $1438\text{ cm}^{-1}$  and  $\text{sp}^2$ ,  $\text{sp}^3$ - hybridized carbon at around  $1300\text{ cm}^{-1}$  were found.

### 5.2.2 Effects of Hydrogen and Oxygen Incorporation

The role of hydrogen in DLC film properties was examined by incorporating hydrogen into the film instead of heating hydrogen out. Sample acju17 and acau07 were grown under the same deposition pressure (1 Pa), but acau07 had a hydrogen partial pressure of 0.1 Pa. It is obvious that hydrogen changes the film properties. Acau07 is more transparent and shows a low absorption window between  $1900$  and  $2800\text{ cm}^{-1}$ . Thus, it indicates that hydrogen raises the optical band gap of the film.

Intentional incorporation of oxygen (sample acjl27) leads to an increase in absorption. But there isn't a C=O absorption band at about  $1700\text{ cm}^{-1}$  observed in this film. This may be due to that the C=O bond is weak and easily stripped off by bombardment from Ar neutrals and some other particles in the chamber. Besides, at this low pressure, hydrogen impurity is sputtered off thus little HC=O bond can be formed. And it is also possible that the C=O absorption is widened and buried by the strong interband absorption tail.

### 5.2.3. Effects of Deposition Pressure

The main deposition variable here is the deposition pressure. From a previous study [13], the deposition pressure had a great effect on the properties of DLC films prepared by magnetron sputtering, such as hardness, resistivity and optical constants in the visible region. It has been found that the higher the pressure, the softer the film, and the higher the optical constants in the visible region. So it is of interest to know the effect of deposition pressure on the infrared properties.

By comparing the spectra of sample acju11, acju13 and auju17, which were grown under the pressure of 8 Pa, 4Pa and 1 Pa respectively, one can see that the higher the pressure, the more transparent the film appears to be. In the d.c. magnetron sputtering method used for these samples, the energetic working gas ions, in this case Ar ions, bombard the target surface generating neutral target atoms, neutralized sputtering Ar ions and secondary electrons. Under the applied electric and magnetic fields, the electrons are trapped by the Lorentz force and have little effect on the film growth. In addition to the sputtered target neutrals, the bombardment from the Ar neutrals and Ar ions are the main factors in the film

growth. Ar neutrals have the energies up to the target voltage in eVs and it has been shown that Ar ions actually have little effect on the optical constants [13], thus, Ar neutrals seem to have the greatest effect on the film deposition. The mean free path of a particle is inversely proportional to the pressure. Therefore, at high pressure, the Ar neutrals have a relatively shorter mean free path, which means they will endure more scattering and have lower energy when they bombard the growing film. In this case, some other impurities, such as hydrogen and oxygen, will then be easily incorporated into the film. And the hydrogen incorporated into the film can decrease the optical band gap and make the film more transparent. On the other hand, low pressure will result in long mean free path and high bombardment energy, thus, hydrogen and oxygen impurities may be sputtered off as a result of energetic impacts, while carbon atoms can still accumulate on substrate since C-C bond strength ( 607 KJ/mol) is greater than that of C-H bond (338 KJ/mol) and O=C bond (532 KJ/mol in O=CO) [40]. However, C-N bond strength (754 KJ/mol) is even greater than C-C bond and this is probably why the small C-N absorption peak always exists. With little C-H bonding in the low pressure film acju17, it appears to be very absorbing.

Even though no hydrogen was deliberately introduced, there are still considerable amounts of hydrogen in the films grown under high pressure (acju11 and acju13) as seen in the strong absorption band near  $2900\text{ cm}^{-1}$  due to the C-H stretching mode, and it seems that the hydrogen makes the films more transparent and like the hydrogenated film acau07. So this indicates that the deposition pressure may affect the film properties through incorporating hydrogen and other impurities into the film. This hydrogen can arise from a background impurity in the chamber or even from the carbon source since graphite strongly

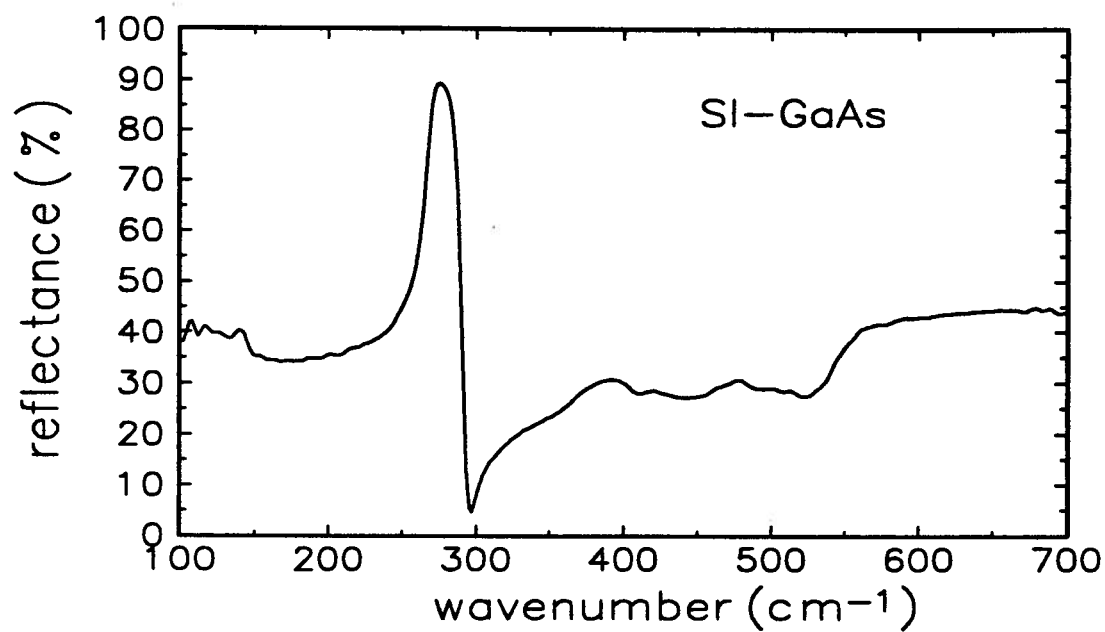
absorb  $\text{H}_2\text{O}$ . Furthermore, we should not assume that the films grown by d.c. magnetron sputtering are all hydrogen free since no hydrogen is intentionally incorporated. These samples were grown under the lowest impurity levels that the system could reach, but we still can see that the C-H bonding at about  $2900\text{ cm}^{-1}$  exists in the high pressure films. Unfortunately, the system cannot do better than this, which means the hydrogen impurity cannot be totally removed from the system.

Considering the C-H stretching absorption band at around  $2900\text{ cm}^{-1}$ , which has been used for quantitative analysis for chemically bound hydrogen [41] and used to evaluate hydrocarbon content in DLC films [42], it does not exist in sample acju17 and it is stronger and wider in acju11 than in acju13, indicating more hydrogen is bonded to carbon atoms in acju11 and there might be a larger amount of hydrocarbon. But it is hard to judge the total hydrogen content since hydrogen can present in a bound and unbound form.

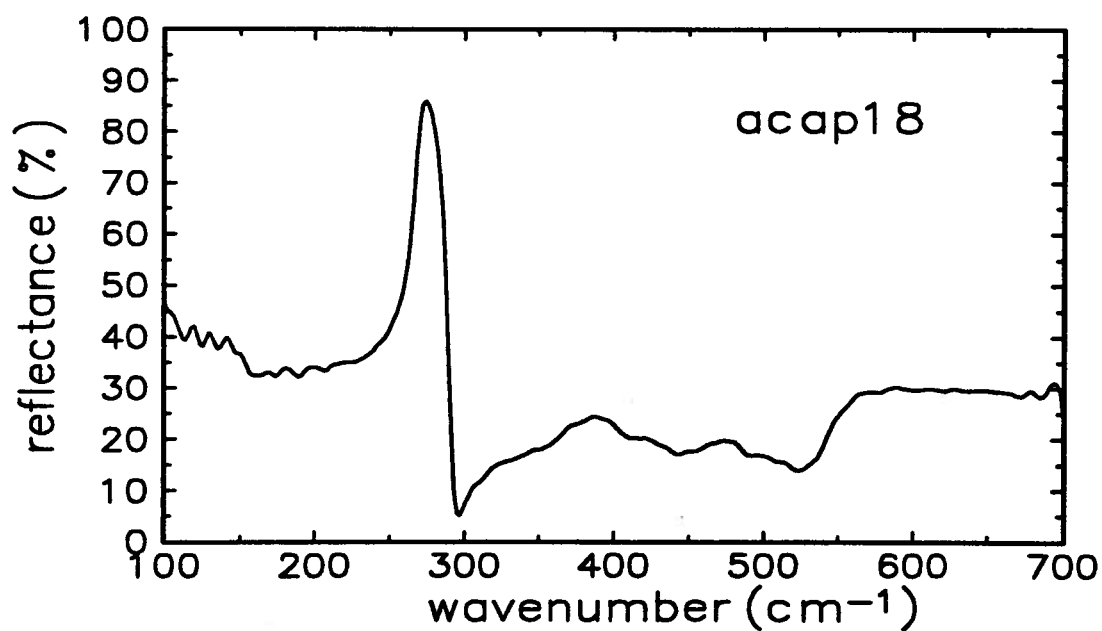
From S.Craig and G.L.Harding's report [20], the reduction in the optical band gap is associated with a decrease in hydrogen content and an increase in C=C bonding. As for our samples, the absorption coefficient spectra (Fig. 5-10, Fig. 5-11 and Fig. 5-12) suggest that the higher the pressure, the larger the optical band gap. This is consistent with S. Craig's results because the higher the pressure, the more hydrogen atoms are bonded to carbon atoms. The background absorption is mainly due to the Urbach tail from interband transitions, which is expressed as an exponential function and indicates that the flatter the spectrum curve, the larger the optical band gap. Then from the background shape, it can be deduced that acju11 has the maximum optical band gap and acju17 has the minimum. The statement by S.Craig about C=C bond seems to be true for acju11

and acju13 because C=C bonding increased in acju13. But it is hard to say for acju17 since the absorption band below  $1700\text{ cm}^{-1}$  is so wide that it can consist of many overlapping resonances and it is difficult to extract accurate parameters for this bond.

As mentioned before, the study in the visible region found that the higher the pressure, the lower the extinction coefficient  $k$ . This conclusion is supported by our near-infrared (NIR) results. In the NIR region, reflectance measurements of the DLC film on both Si-GaAs and glass substrates were performed in order to reduce the error in  $k$ . As illustrated in Fig. 5-15,  $k$  increases with decreasing pressure.



(A)



(B)

Fig. 5-1: (A):Far-infrared reflectance spectrum of Si-GaAs. (B) Far-infrared reflectance spectrum of sample acap18

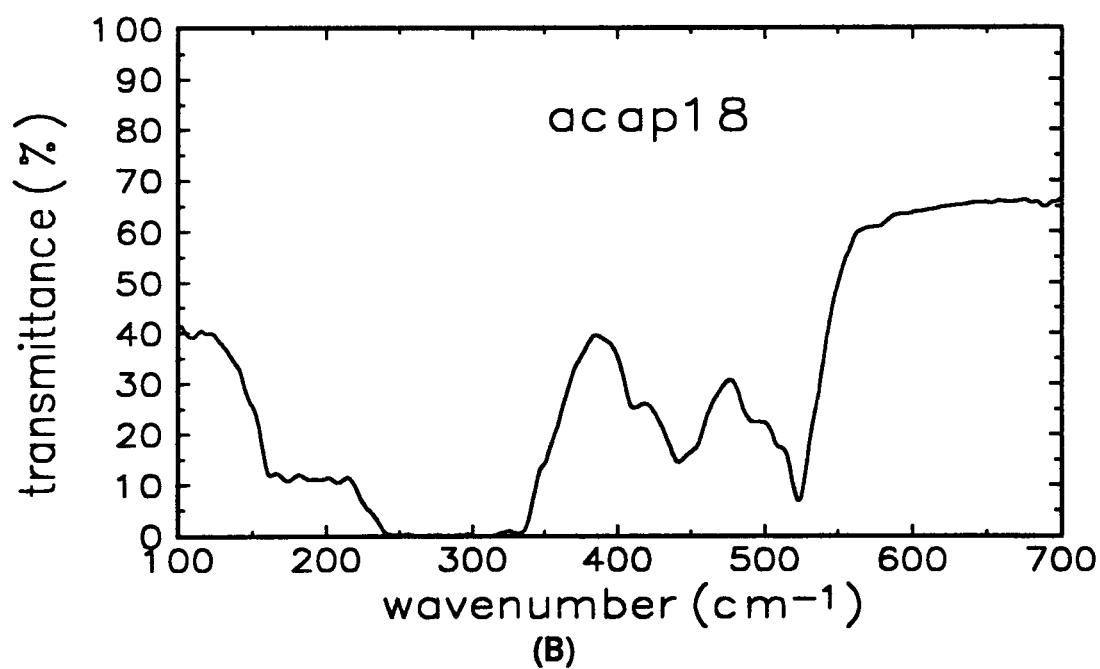
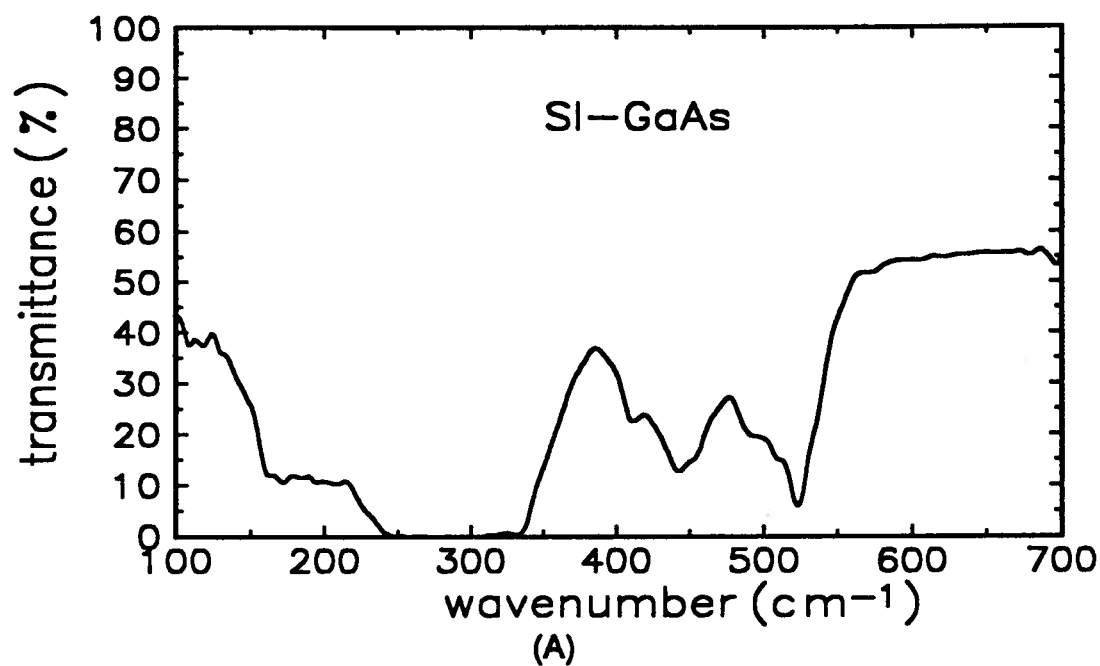


Fig. 5-2: (A): Far-infrared transmittance spectrum of SI-GaAs. (B): Far-infrared transmittance spectrum of sample acap18.



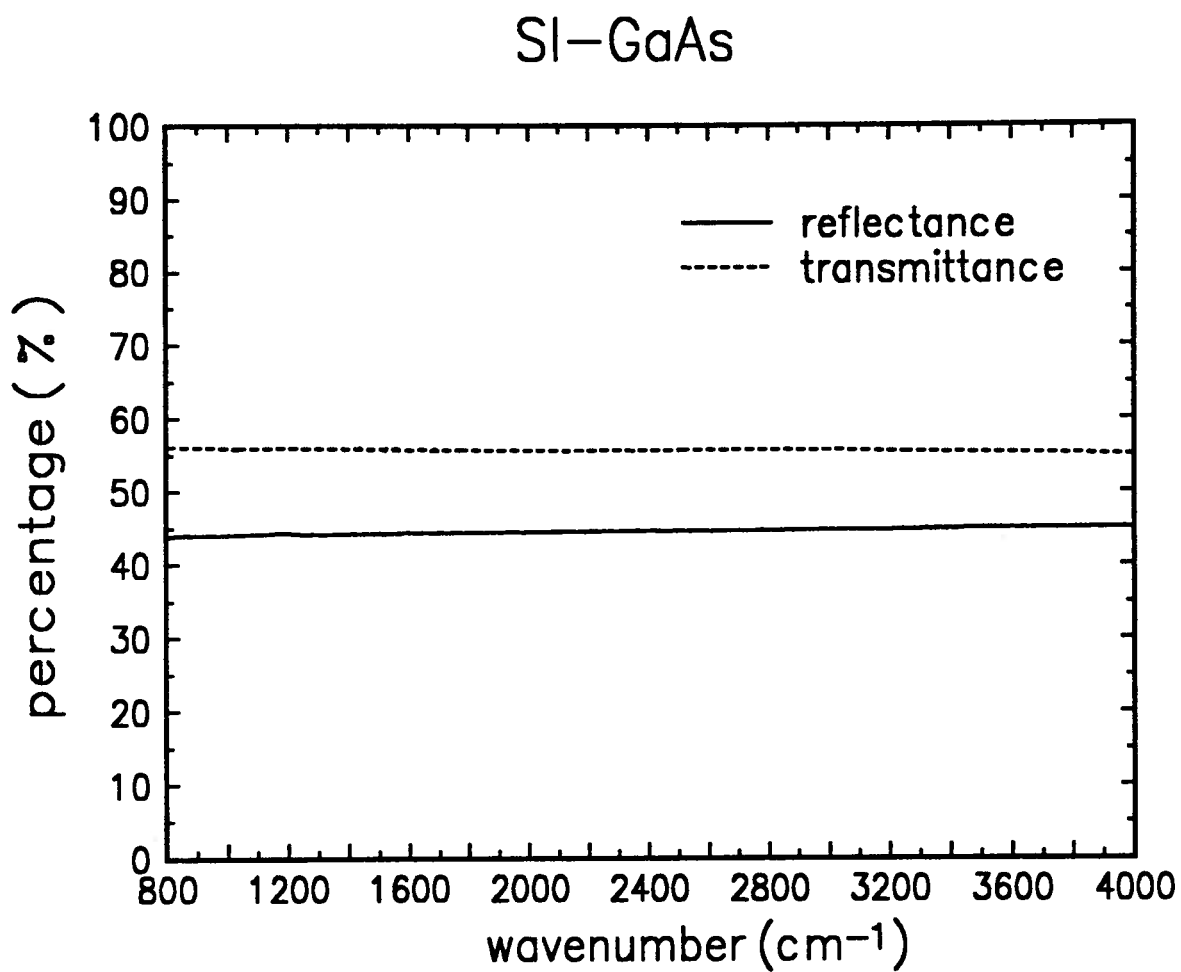


Fig. 5-3: Reflectance and transmittance spectra of semi-insulating GaAs (SI-GaAs)

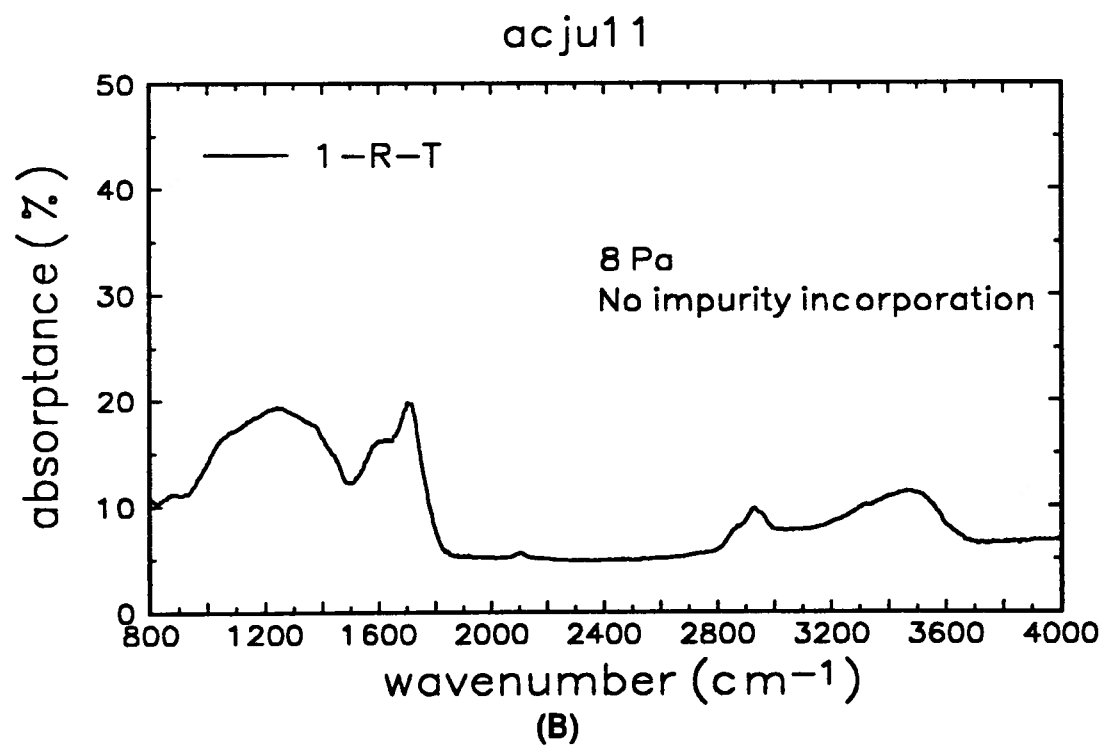
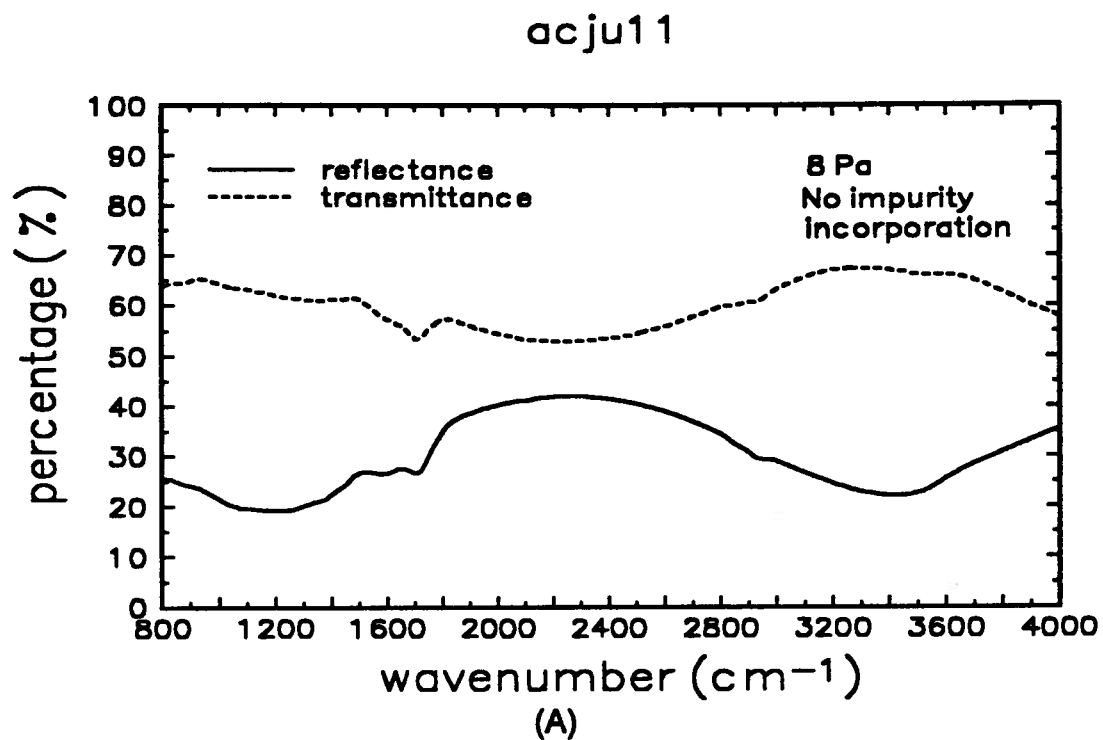


Fig. 5-4: (A): Mid-infrared reflectance and transmittance spectra of acju11. (B): Mid-infrared absorbance spectrum of acju11.

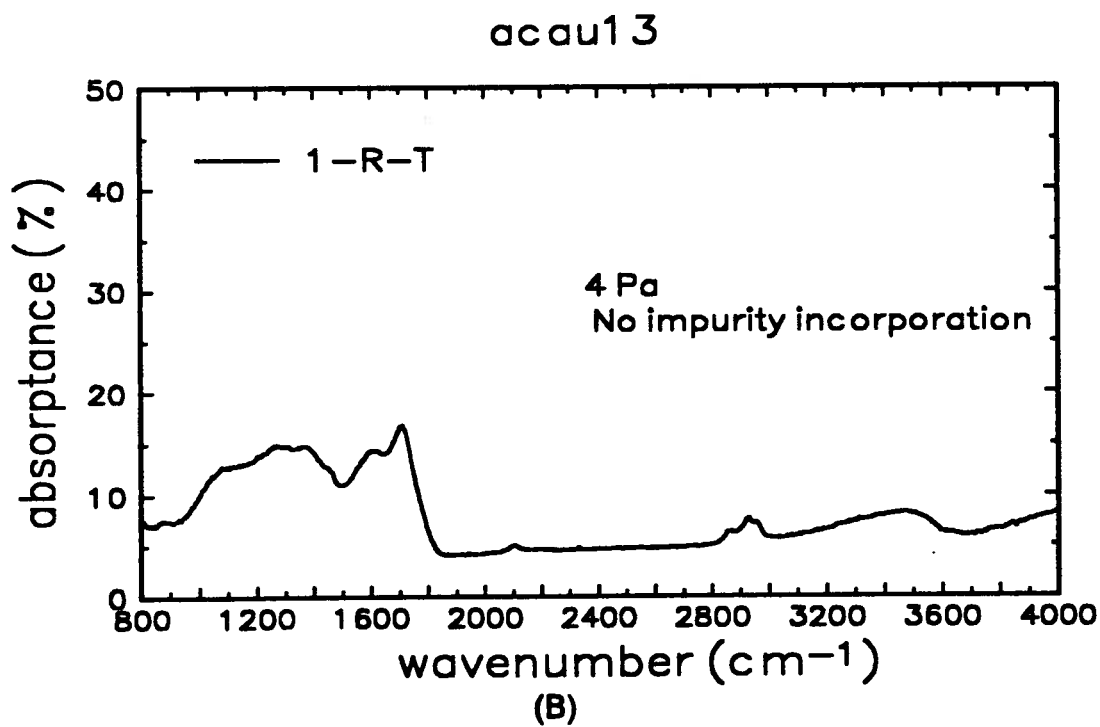
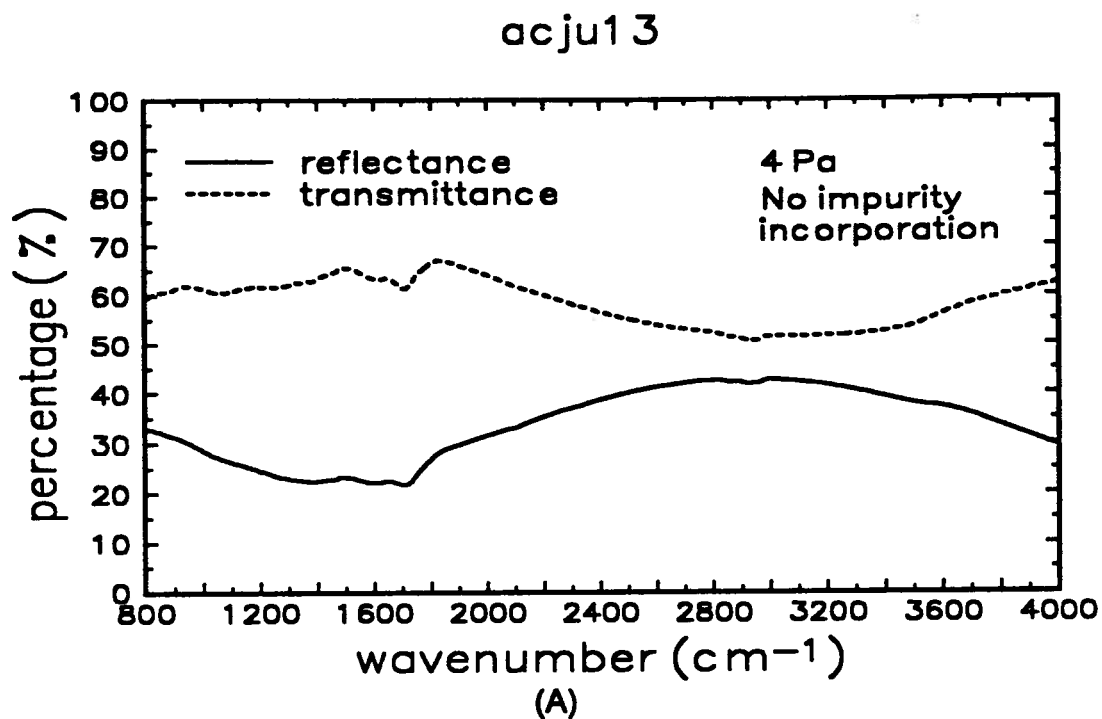


Fig. 5-5: (A): MIR reflectance and transmittance spectra of acju13. (B): MIR absorbance spectrum of acju13.

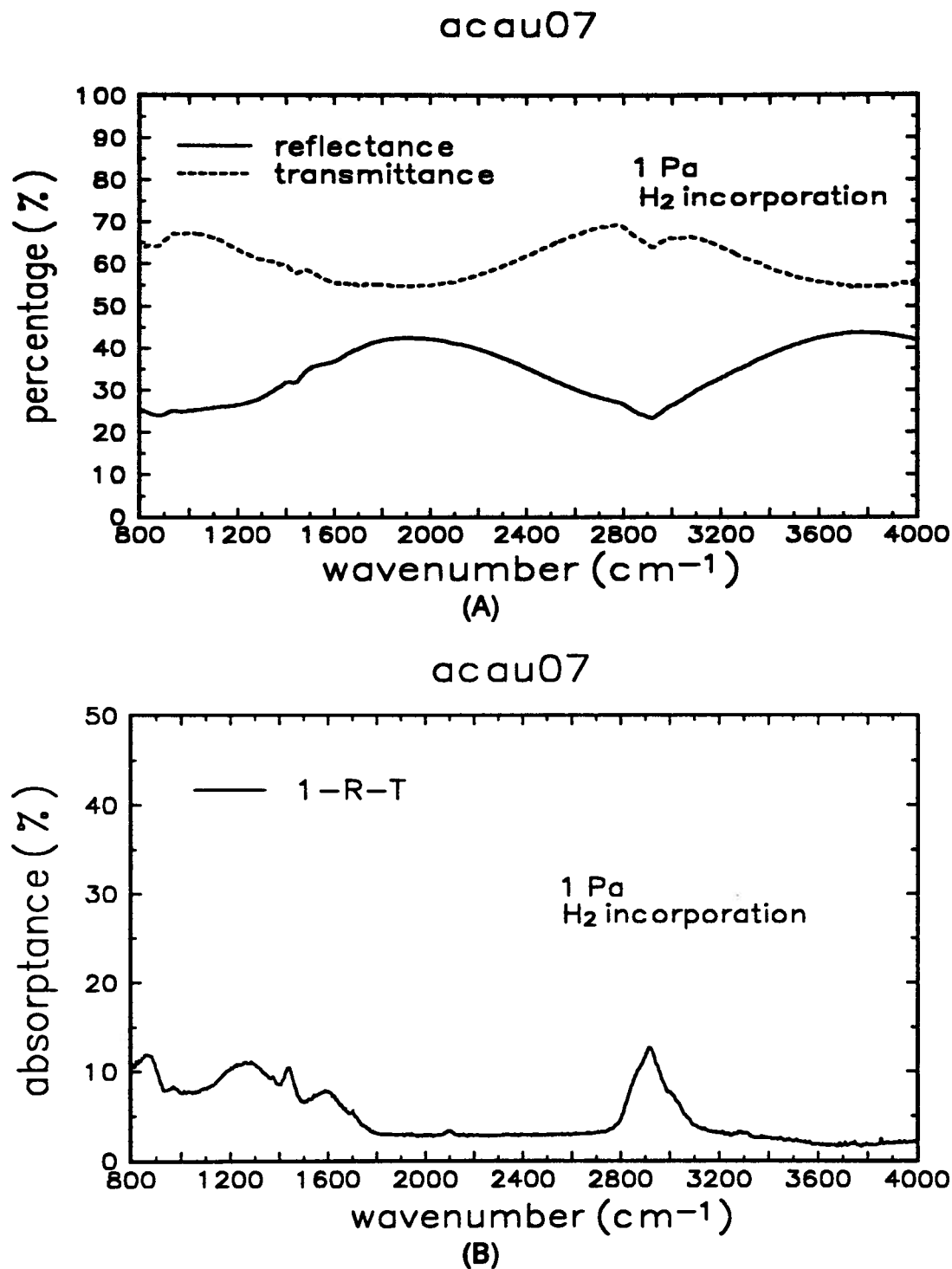


Fig.5-6: (A) MIR reflectance and transmittance spectra of acau07. (B): MIR absorbance spectrum of acau07

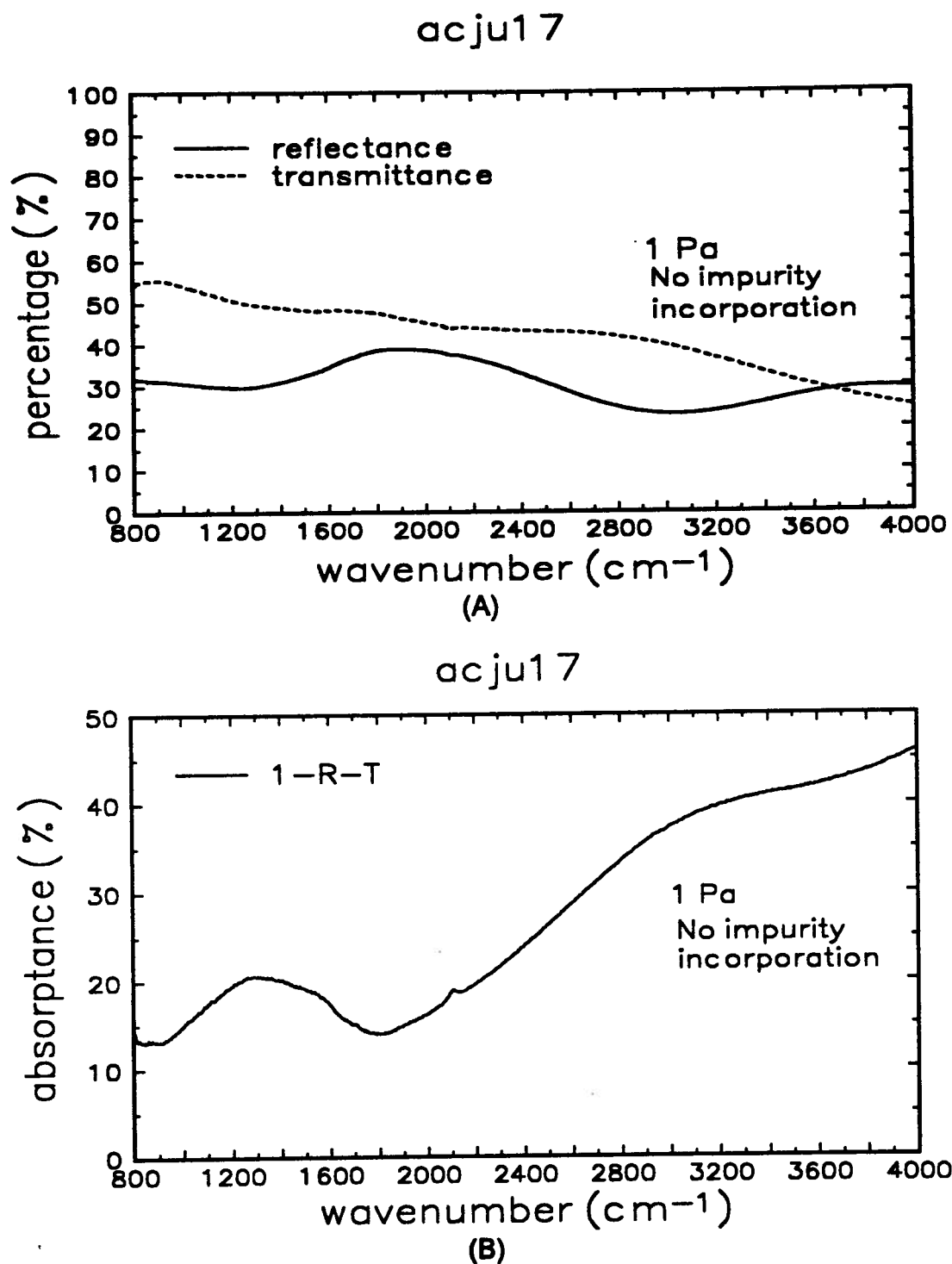


Fig.5-7: (A) MIR reflectance and transmittance spectra of acju17. (B): MIR absorbance spectrum of acju17

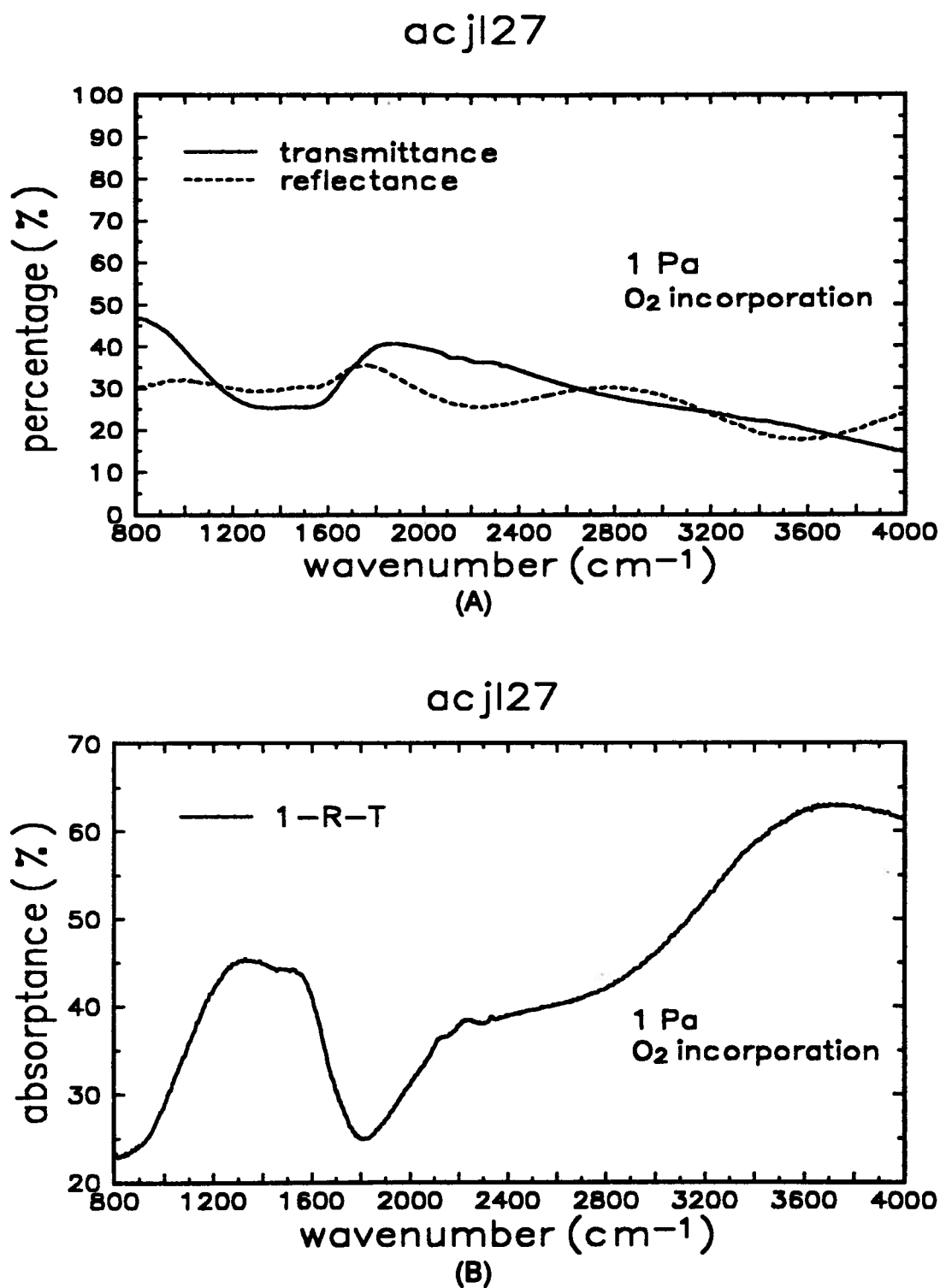


Fig.5-8: (A) MIR reflectance and transmittance spectra of acjl27. (B): MIR absorbance spectrum of acjl27

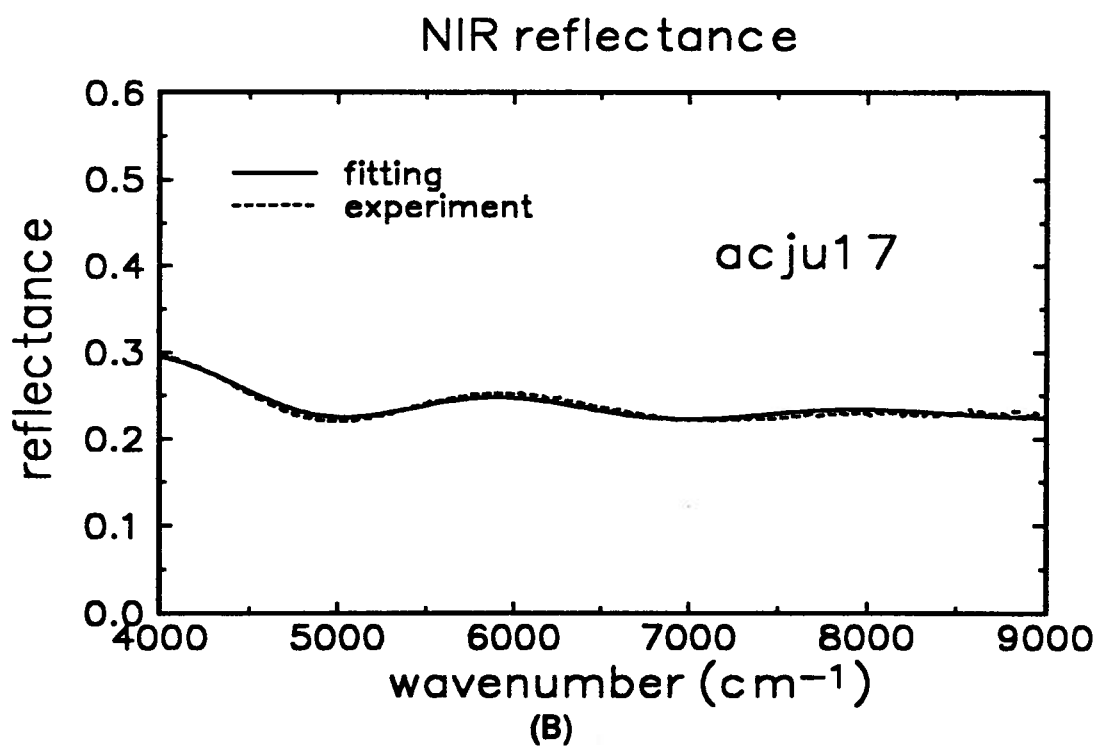
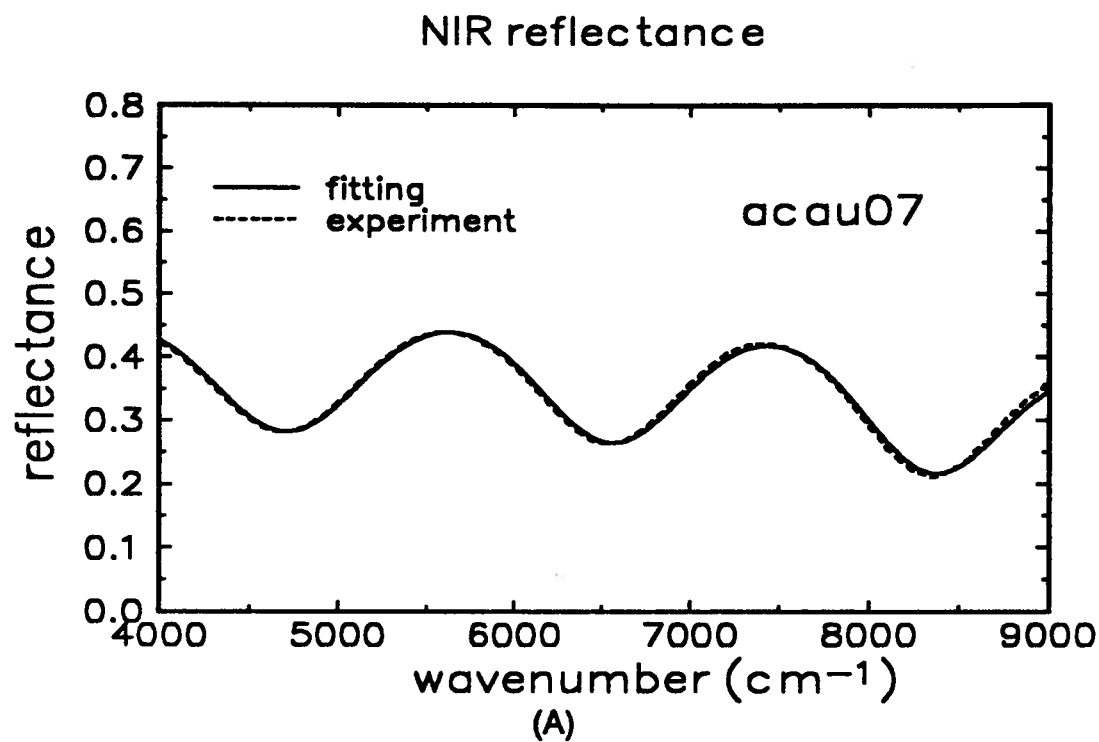


Fig.5-9: Near-infrared reflectances of sample acau07 and acju17. The dashed line is experiment result and the solid line is data fitting

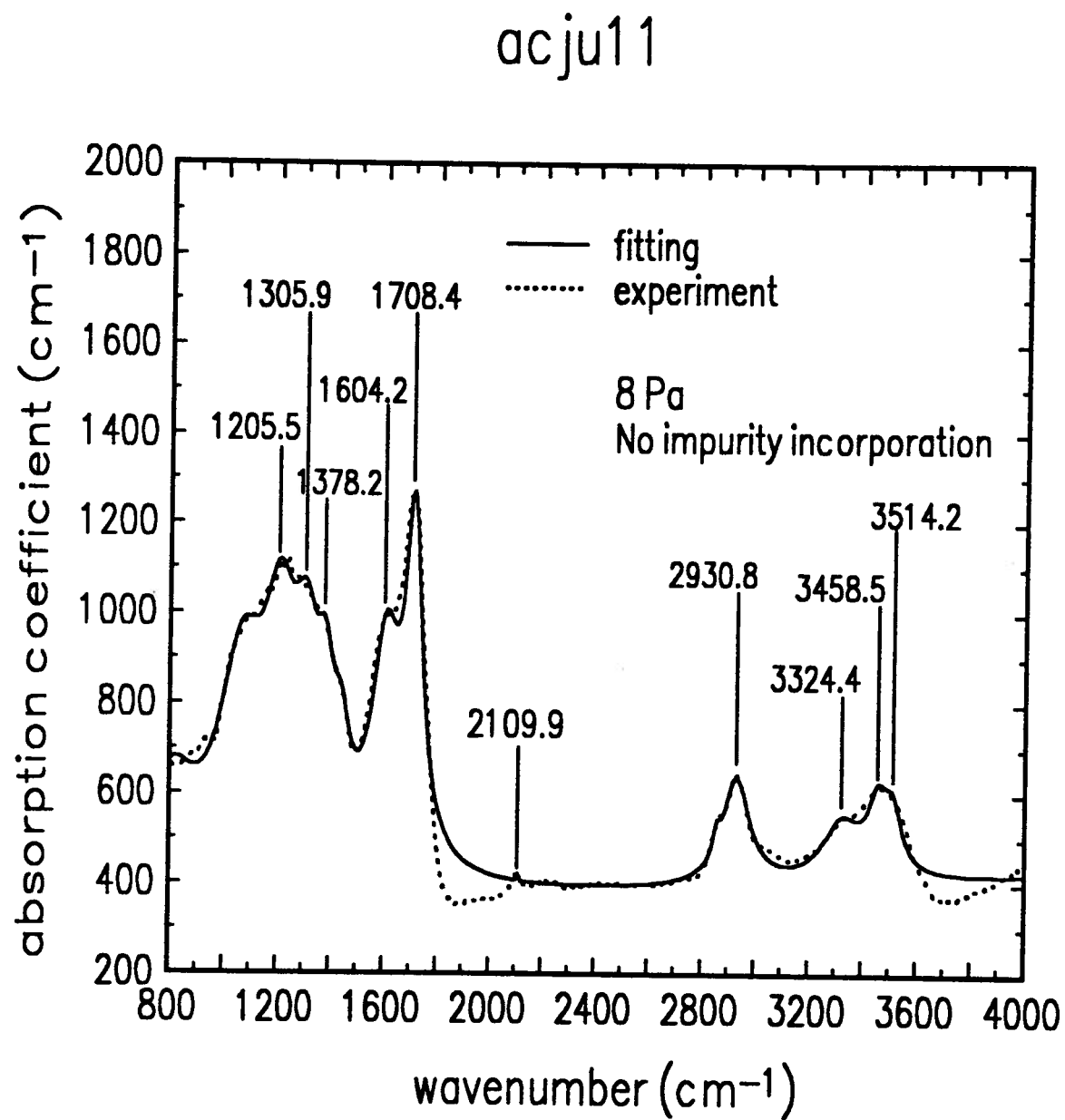


Fig. 5-10: Absorption coefficient of acju11. The dotted line is from experiments and the solid line is from data fitting



acju13

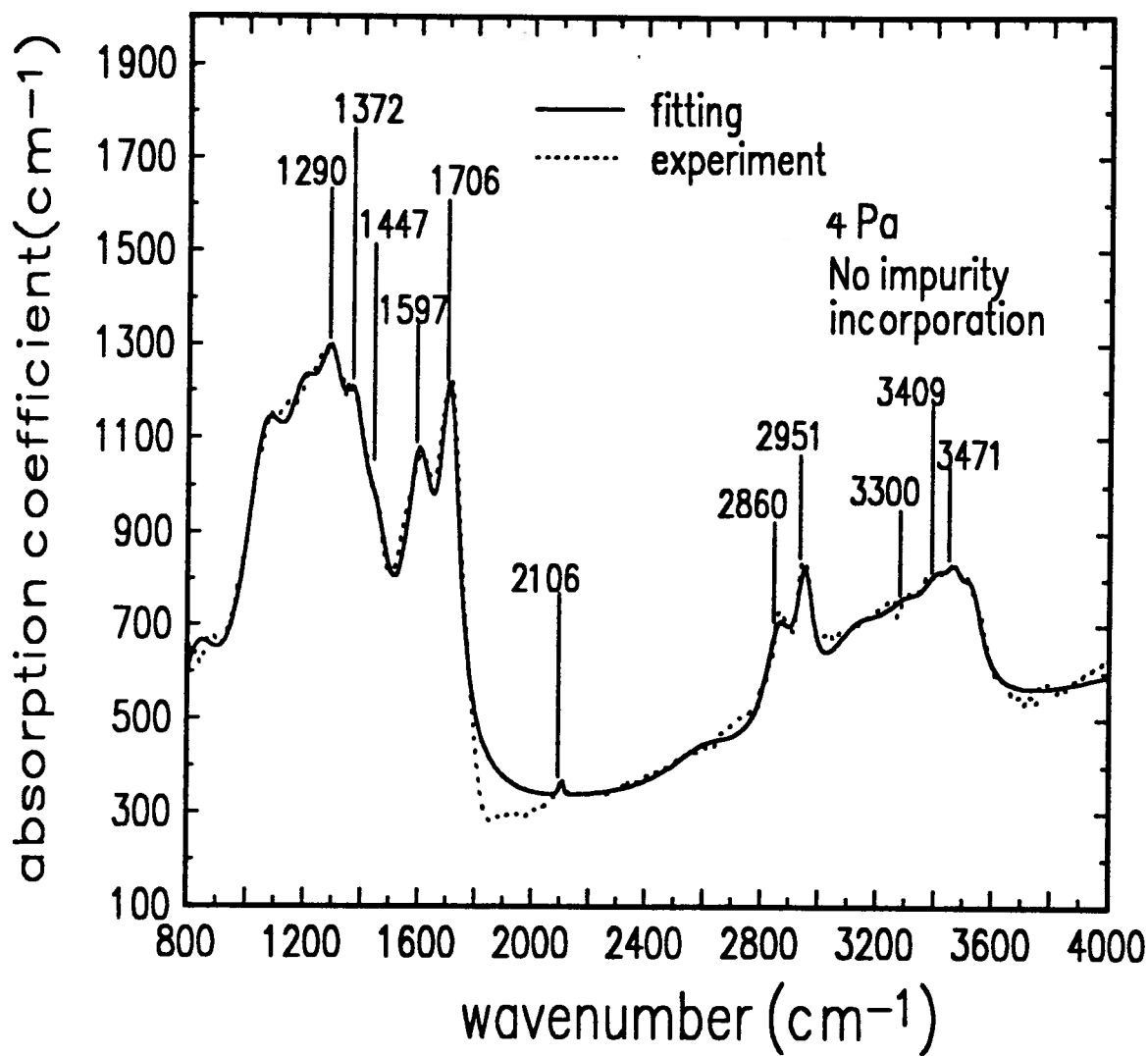


Fig. 5-11: Absorption coefficient of acju13. The dotted line is from experiments, the solid line is from data fitting

acju17

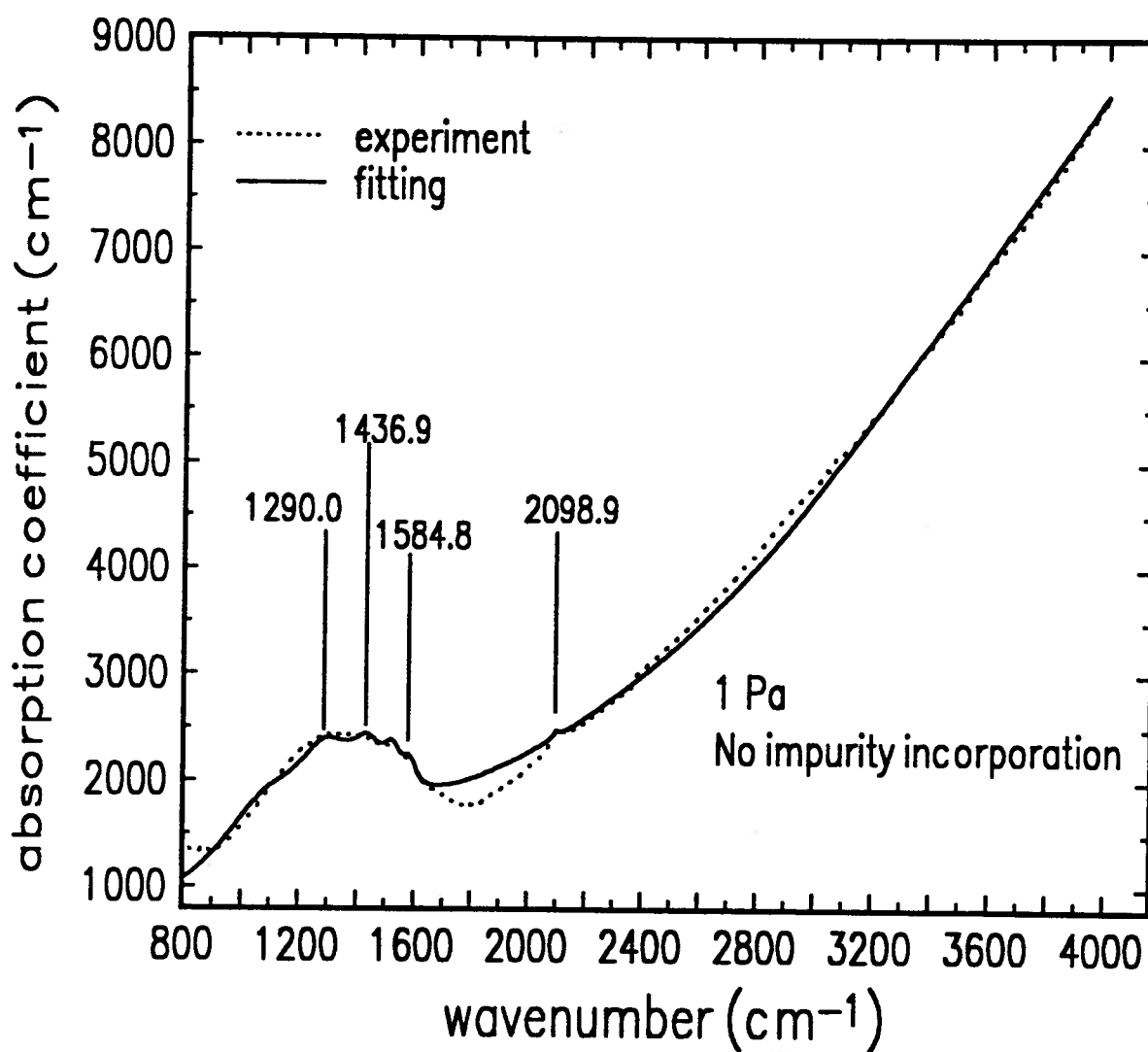


Fig. 5-12: Absorption coefficient of sample acju17. The dotted line is from experiments and the solid line is from data fitting

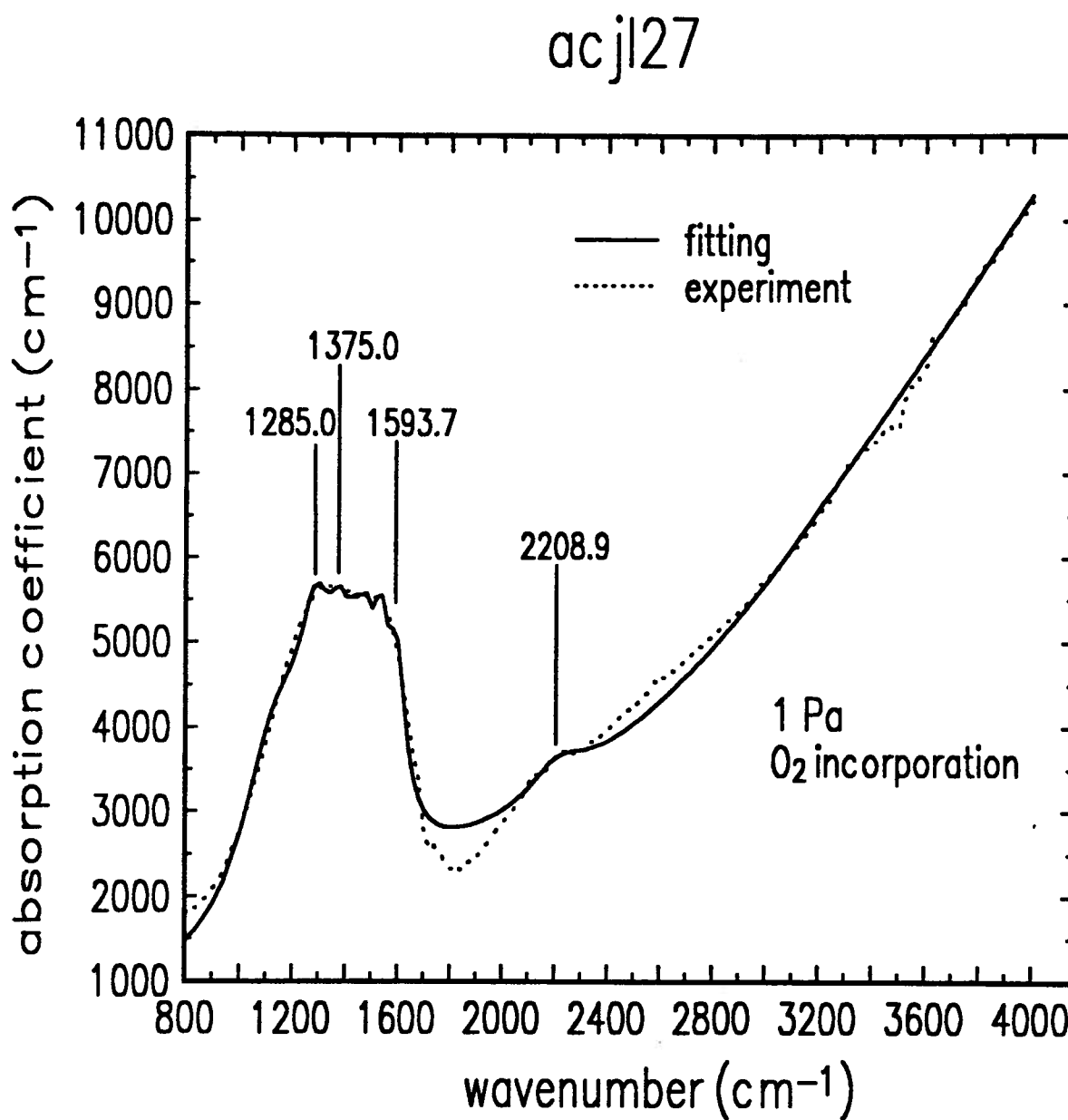


Fig. 5-13: Absorption coefficient of sample acjl27. The dotted line is from experiments and the solid line is from data fitting

acau07

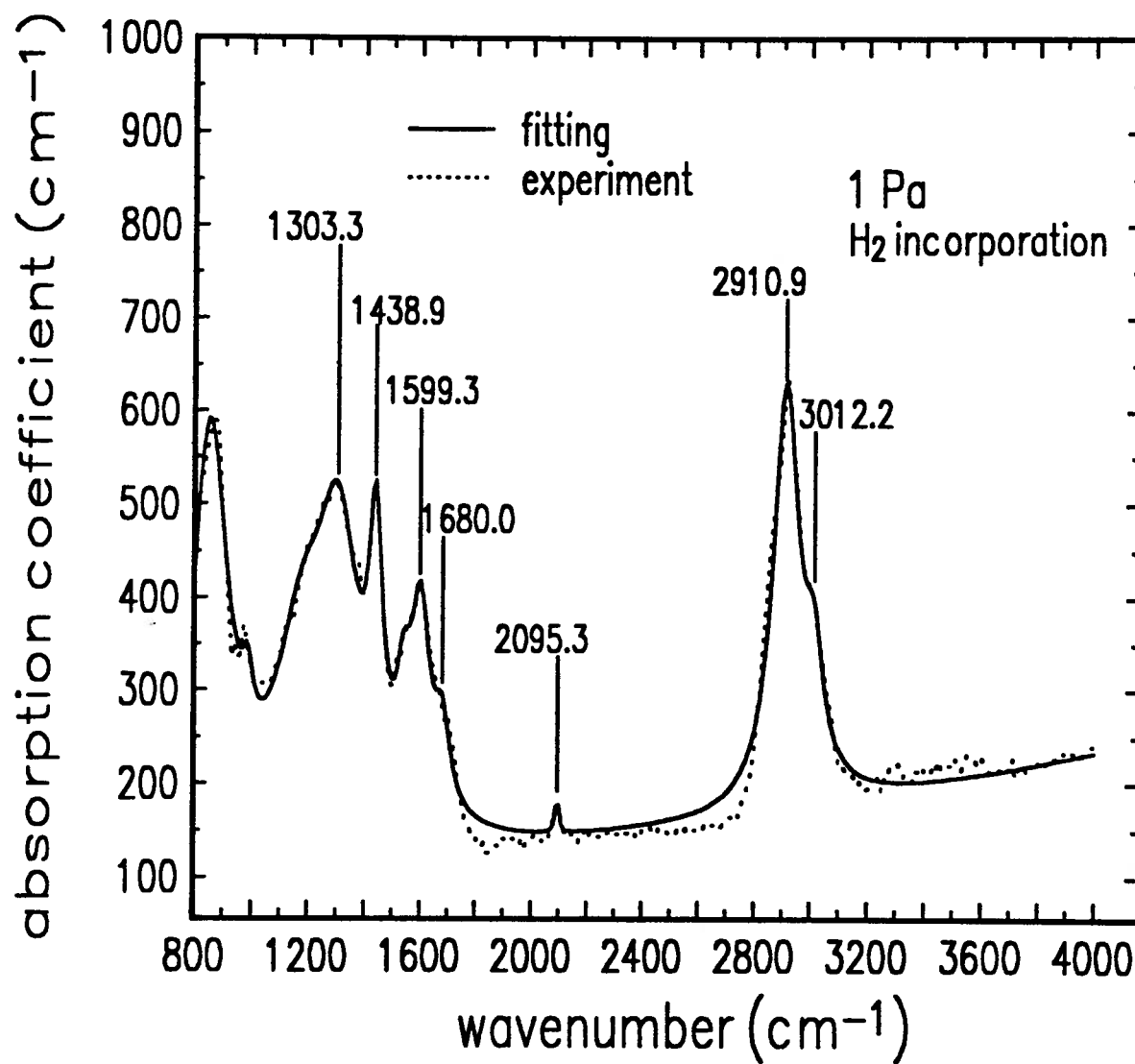


Fig. 5-14: Absorption coefficient of sample acau07. The dotted line is from experiments and the solid line is from data fitting

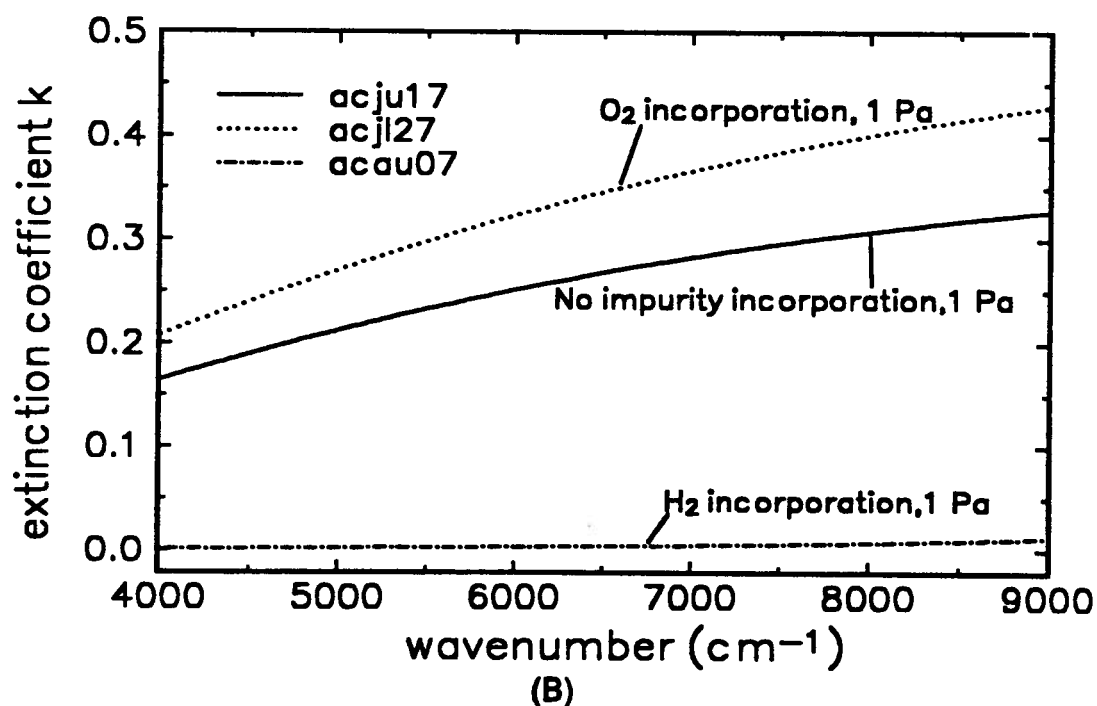
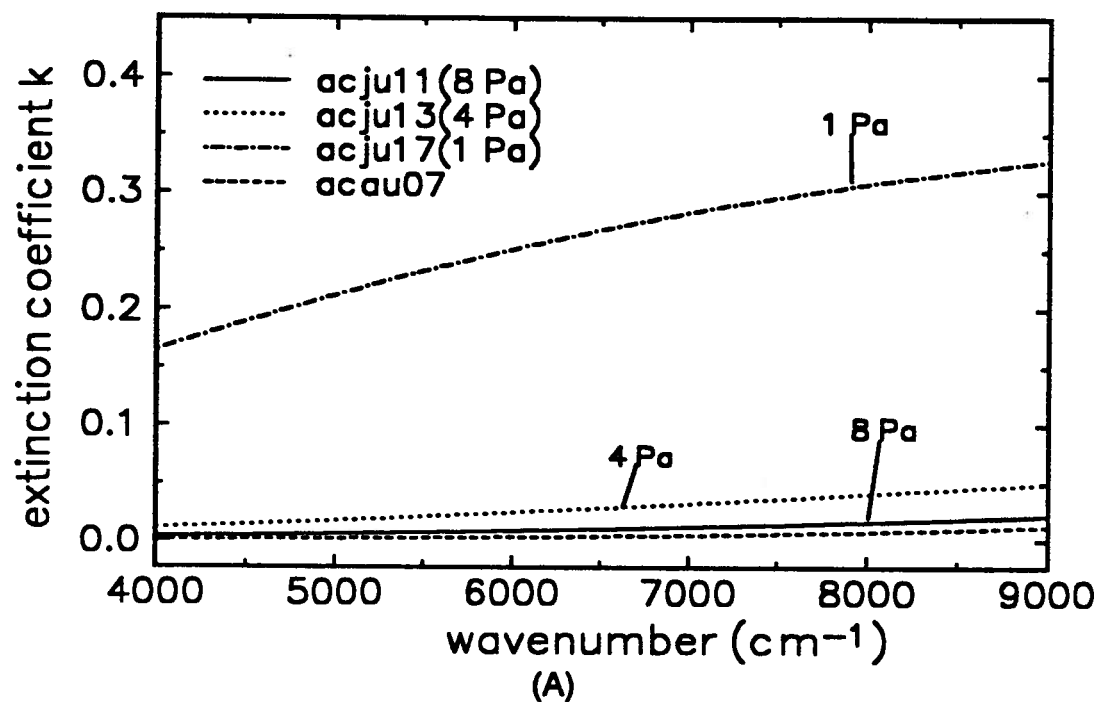


Fig. 5-15: (A): Extinction coefficient  $k$  for films of different deposition pressure. (B): Extinction coefficient  $k$  for films of 1 Pa, with hydrogen and oxygen incorporation ( $acau07$  and  $acjl27$ ) and without any impurity incorporation ( $acju17$ )

Table 5-1: Fitting Parameters and Possible Bonding

| Possible Bonding | acju11  |       |          | acju13  |       |          | acju17  |      |          | acjl27  |       |          | acau07  |       |          |
|------------------|---------|-------|----------|---------|-------|----------|---------|------|----------|---------|-------|----------|---------|-------|----------|
|                  | $\nu_0$ | $J$   | $\Gamma$ | $\nu_0$ | $J$   | $\Gamma$ | $\nu_0$ | $J$  | $\Gamma$ | $\nu_0$ | $J$   | $\Gamma$ | $\nu_0$ | $J$   | $\Gamma$ |
| (1)              | 3514.2  | 1.38  | 38.0     | 3530.1  | 2.19  | 42.6     |         |      |          |         |       |          |         |       |          |
| (1)              | 3458.5  | 2.16  | 46.5     | 3470.9  | 1.50  | 39.2     |         |      |          |         |       |          |         |       |          |
|                  |         |       |          | 3409.4  | 3.60  | 67.8     |         |      |          |         |       |          |         |       |          |
| (2)              | 3324.4  | 3.72  | 87.2     | 3299.7  | 5.90  | 112.1    |         |      |          |         |       |          | 3012.2  | 1.69  | 39.2     |
|                  |         |       |          | 3128.6  | 11.6  | 156.1    |         |      |          |         |       |          | 2910.9  | 9.65  | 56.4     |
| (3)              | 2930.8  | 5.45  | 60.5     | 2950.7  | 3.27  | 33.3     |         |      |          |         |       |          |         |       |          |
| (4)              | 2858.0  | 0.29  | 15.2     | 2860.1  | 4.82  | 56.4     |         |      |          |         |       |          |         |       |          |
|                  |         |       |          |         |       |          |         |      |          |         |       |          |         |       |          |
| (5)              | 2109.9  | 0.005 | 0.6      | 2105.8  | 0.13  | 4.79     | 2098.9  | 0.4  | 12.5     | 2208.9  | 22.1  | 123.4    | 2095.3  | 0.16  | 6.78     |
| (6)              | 1708.4  | 17.8  | 38.9     | 1706.5  | 20.0  | 43.1     |         |      |          |         |       |          | 1680.0  | 1.84  | 32.6     |
| (7)              | 1604.2  | 22.1  | 66.9     | 1597.1  | 26.6  | 64.9     | 1584.8  | 3.91 | 25.7     | 1593.7  | 46.47 | 41.1     | 1599.3  | 6.22  | 41.9     |
|                  |         |       |          |         |       |          | 1524.7  | 8.66 | 38.0     | 1531.7  | 41.8  | 36.31    | 1541.0  | 1.69  | 27.4     |
| (8)              | 1438.5  | 4.85  | 37.9     | 1447.1  | 14.3  | 61.9     | 1436.9  | 22.9 | 68.9     | 1439.1  | 55.68 | 53.0     | 1438.9  | 5.61  | 28.9     |
| (9)              | 1378.2  | 7.56  | 39.1     | 1372.2  | 16.35 | 49.9     |         |      |          | 1375.0  | 43.85 | 49.3     |         |       |          |
| (10)             | 1305.9  | 17.6  | 60.3     | 1290.0  | 28.22 | 63.5     | 1290.0  | 76.6 | 127.4    | 1285.0  | 88.6  | 174.1    | 1303.3  | 21.46 | 89.9     |
|                  | 1205.5  | 32.15 | 77.7     | 1195.0  | 42.25 | 86.2     |         |      |          |         |       |          | 1174.7  | 24.14 | 118.7    |
|                  | 1059.1  | 53.3  | 108.2    | 1056.5  | 75.75 | 102.8    | 1067.1  | 41.7 | 202.4    | 1124.8  | 402.9 | 166.4    | 985.3   | 1.42  | 21.2     |
|                  | 792.7   | 47.84 | 122.0    | 822.6   | 53.8  | 103.9    |         |      |          |         |       |          | 847.3   | 49.48 | 78.0     |

(1): H-O stretching (2): hydrogen bonded to  $sp^1$  hybridized carbon (3):  $sp^3$ C-H stretching (4): symmetric  $CH_2$  or  $CH_3$  stretching (5): C-N (6): C=O stretch (7): C=C stretch (8): C-H rock or  $CH_2$  deformation (9):  $CH_3$  symmetric bending (10):  $sp^2$ - and  $sp^3$ - hybridized carbon.

## **Chapter 6**

### **CONCLUSION**

Infrared reflectance and transmittance measurements were performed on amorphous DLC films to study the optical properties of these films. The films were grown on semi-insulating GaAs substrates and were deposited by a d.c. magnetron sputtering technique. Through analyzing the near-infrared (NIR) reflectance data, the film thicknesses were obtained. It has been found that the interband transition model of optical constants fits the experimental data in the near-infrared region fairly well. In the mid-infrared (MIR) region, a matrix method was used to calculate the reflectance and transmittance as a function of photon wavenumber. The real and imaginary parts of the complex refractive index were solved by a two dimensional Newton-Raphson iteration method. Furthermore, the absorption coefficient spectra were fitted by a dispersion model taking account of the Urbach background absorption and the excitation of vibrational resonances. Thus, information of chemical bonding was acquired. Even though this model can also fit the experimental results very well, it should be noted that small adjustments to the parameters used in the model or adding more lines would allow a better fit. However, general bonding configuration of the films were still obtained.

The properties of DLC films were found to be strongly dependent on the film deposition parameters. Films prepared under different deposition pressures displayed different optical properties. The NIR results showed that the higher the pressure, the lower the extinction coefficient  $k$  and absorption. This is consistent with the findings in the visible region. Films grown under high pressure also

showed a high optical band gap and a flat low absorption window between 1900 and 2700  $\text{cm}^{-1}$ . Considering the bonding configuration, it is different from film to film. At low pressures, neither C-H stretching bond at about 2900  $\text{cm}^{-1}$  nor the C=O bond at around 1700  $\text{cm}^{-1}$  were visible. At high pressure, more vibrational resonances were seen. One possible explanation is the short mean free path and low bombardment energy of Ar neutrals under high pressure and the resulting incorporation of impurities. Thus it suggests that the deposition pressure has an effect on film properties mainly through incorporating impurities into the film. The large optical band gap and low absorption feature in the film grown under high pressure may be due to the incorporated hydrogen in the film. The role of hydrogen was studied by incorporating hydrogen into the film grown under low pressure (1 Pa). We can see that, under the same deposition pressure, the film without hydrogen incorporation and the one with hydrogen incorporation are quite different. The hydrogenated film appeared to be more transparent in both NIR and MIR region. This is consistent with other people's reports [20]. The effect of oxygen incorporation was also investigated and it was found that oxygen increased the absorption.

One objective of this study was to see whether it is possible to use d.c. magnetron sputtering to grow diamond-like hydrogen free carbon films, which do not possess the C-H stretching absorption at about 2900  $\text{cm}^{-1}$  and thus have a resulting much wider low absorption "window". Unfortunately, it seems impossible for the system used for our films. At low pressure, there is not this C-H resonance but the optical band gap is too low and the film is too absorbing in the whole region. At high pressure, the film is much more transparent and displays the flat low absorption "window", but there exists the C-H stretching absorption band even



if no hydrogen has been incorporated. Therefore, one should not assume that the film is hydrogen free just because no hydrogen is incorporated intentionally. The impurities should not be ignored. This study suggests that the optimum deposition conditions for a DLC film with good IR transparency may be a low deposition pressure with hydrogen incorporation, which may result in a more IR-transparent film, with lower non-hydrogen impurity absorption, compared with a high pressure and no hydrogen incorporation.

It was also shown in this study that Fourier-transform infrared spectroscopy is a very important and effective tool for the characterization of thin films. It has the advantage of being non-contact, non-destructive and covering a wide spectral range.

## **Bibliography**

- [1] Hsiao-chu Tsai and D. B. Bogy, *J. Vac. Sci. Technol.* **A5** (6), 3287 (1987)
- [2] S. Aisenberg and R. Chabot, *J. Appl. Phys.* **42**, 2953 (1971)
- [3] B. Dischler, A. Bubenzer and P. Koidl, *Appl. Phys. Lett.* **42** (8), 636 (1983)
- [4] J. C. Angus and Y. Wang, *Diamond and Diamond-like Films and Coatings*, edited by R. E. Clausing, L. L. Horton, J. C. Angus and P. Koidl ( Plenum Press, New York, 1991 ), p.173
- [5] N. Sawides, *J. Appl. Phys.* **58** (1), 518 (1985)
- [6] A. H. Lettington, *Diamond and Diamond-like Films and Coatings*, edited by R. E. Clausing, L. L. Horton, J. C. Angus and P. Koidl ( Plenum Press, New York, 1991 ), p.481
- [7] O. Stenzel, G. Schaarschmidt, F. Wolf, M. Vogel and T. Wallendorf, *Thin Solid Films* **203**, 11 (1991)
- [8] Yves Catherine, *Diamond and Diamond-like Films and Coatings*, edited by R. E. Clausing, L. L. Horton, J. C. Angus and P. Koidl ( Plenum Press, New York, 1991 ), p.193
- [9] A. Bubenzer, B. Dischler, G. Brandt and P. Koidl, *J. Appl. Phys.* **54** (8), 4590 (1983)
- [10] N. Sawides and B. Windows, *J. Vac. Sci. Technol.* **A3** (6), 2386 (1985)
- [11] Glenn A. Clarke, Thesis of Master of Applied Science in University of British Columbia, (1990)

- [12] Z. Marinkovic and R. Roy, Carbon **14**, 329 (1976)
- [13] G. A. Clarke and R. R. Parsons, Thin solid Films **236**, 67 (1993)
- [14] C. Weissmantel, K. Bewilogua, K. Breuer, D. Dietrich, U. Ebersbach, H.-J. Erier, B. Rau and G. Reisse, Thin Solid Films **96**, 31 (1982)
- [15] R. S. Bhattacharya, R. L. C. Wu and C. S. Yust, Nuclear Instruments and Methods in Physics Research, **B59-B60**, 1383 (1991)
- [16] D. R. McKenzie, R. C. McPhedran, L. C. Botten, N. Savvides and R. P. Netterfield, Appl. Opt. **21**, 3615 (1982)
- [17] E. M. Hamilton, J. A. Cross and C. J. Adkins, *Amorphous and Liquid Semiconductor*, edited by J. Stuke and W. Brenig (Taylor and Francis, London, 1973 ), p.1225
- [18] N. Savvides, J. Appl. Phys. **58**(1), 518 (1985)
- [19] J. J Hauser, J. Non-Cryst. Solids **23**, 21 (1977)
- [20] S. Craig and G. L. Harding, Thin Solid Films **97**, 345 (1982)
- [21] F. W. Smith, J. Appl. Phys. **55**, 764 (1984)
- [22] O. Stenzel, S. Roth and W. Scharff, Thin Solid Films **190**, 9 (1990)
- [23] M. P. Nadler, T. M. Donovan and A. K. Green, Thin Solid Films **116**, 241 (1984)
- [24] J. Ullmann, G. Schmidt and W. Scharff, Thin Solid Films **214**, 35 (1992)
- [25] A. A. Khan, D. Mathine, J. A. Woollam and Y. Chung, Phys. Rev. **B28**, 7229 (1983)

- [26] R. J. Bell, *Introductory Fourier Transform Spectroscopy*, Academic Press, New York (1972)
- [27] W. Herres and J. Gronholz, *Comp. Appl. Lab.* **2**, 216 (1984)  
J. Gronholz and W. Herres, *Instruments and Computers* **3**, 10 (1985)
- [28] J. E. Eldridge, private communications
- [29] R. A. Smith, F. E. Jones and R. P. Chasmar, *The Detection and Measurement of Infra-red Radiation*, Clarendon Press, Oxford (1958)
- [30] H. Levinstein, *Semiconductors and Semimetals* vol.5, chapter 1, edited by R. K. Willardson and A. C. Beer (Academic Press, New York, 1970)
- [31] P. W. Kruse, *Semiconductors and Semimetals* vol.5, chapter 2, edited by R. K. Willardson and A. C. Beer (Academic Press, New York, 1970)
- [32] A. E. Martin, *Vibrational Spectra and Structure* Vol.8, edited by J. R. Durig (Elsevier Scientific, New York 1980), p.104
- [33] J. E. Eldridge and C. Homes, *Infrared Physics* **29**, 143 (1989)
- [34] H. A. Macleod, *Thin Film Optical Filters* 2nd edition, Adam Hilger Ltd., Bristol (1986)
- [35] B. Harbecke, *Appl. Phys.* **B39**, 165 (1986)
- [36] A. R. Forouhi and I. Bloomer, *Handbook of Optical Constants of Solids II*, edited by E. D. Palik (Academic Press, New York, 1991), p.151
- [37] M. Born and E. Wolf, *Principle of Optics*, Pergamon, Oxford (1964)
- [38] E. D. Palik, *Handbook of Optical Constants of Solids*, edited by E. D. Palik (Academic Press, New York, 1985), p.429

[39] W. H. Press, S. A. Teukolsky, W. T. Vetterling and B. P. Flannery, *Numerical Recipes in C*, 2nd edition, Cambridge University Press (1992), chapter 9

[40] *CRC Handbook of Chemistry and Physics*, 74th edition, editor-in-chief: D. R. Lide, CRC Press, Boca Raton (1993-1994), 9-123

[41] J. C. Angus, J. E. Stultz, P. J. Shiller, J. R. MacDonald, M. J. Mirtith and S. Domitz, *Thin Solid Films* **118**, 311 (1984)

[42] K. Pirker, R. Schallauer, W. Fallmann, F. Olcaytug, G. Urban, A. Jachimowicz, F. Kohl, and O. Prohaska, *Thin Solid Films* **138**, 121 (1986)